UCRL-LR-121751

Nonequilibrium Flows with Smooth Particle Applied Mechanics

Oyeon Kum
(Ph.D. Thesis)

July 1995

Lawrence
Livermore
National
Laboratory

MASTER

DISTRIBUTION OF THIS DOCUMENT IS UNLIMITED 35

Available to DOE and DOE contractors from the
Office of Scientific and Technical Information
P.O. Box 62, Oak Ridge, TN 37831
Prices available from (615) 576-8401, FTS 626-8401

Available to the public from the
National Technical Information Service
U.S. Department of Commerce
5285 Port Royal Rd.,
Springfield, VA 22161

Work performed under the auspices of the U.S. Department of Energy by Lawrence Livermore National Laboratory under Contract W-7405-ENG-48.

UCRL-LR-121751
Distribution Category UC-705

Nonequilibrium Flows with Smooth Particle Applied Mechanics

Oyeon Kum
(Ph.D.Thesis)

Manuscript date: July 1995

LAWRENCE LIVERMORE NATIONAL LABORATORY
University of California • Livermore, California • 94551

NONEQUILIBRIUM FLOWS WITH SMOOTH PARTICLE APPLIED MECHANICS

BY
OYEON KUM
B.S. KYUNGPOOK NATIONAL UNIVERSITY (MATHEMATICS 1980)
M.S. SEOUL NATIONAL UNIVERSITY (PHYSICS 1982)

DISSERTATION

Submitted in partial satisfaction of the requirements for the degree of
DOCTOR OF PHILOSOPHY
in
ENGINEERING – APPLIED SCIENCE
in the
GRADUATE DIVISION
of the
UNIVERSITY OF CALIFORNIA
DAVIS

APPROVED: W G Hoover

Garry Rodrigue

DA McQuarrie

D S Miller

COMMITTEE IN CHARGE

1995

Blank page

This thesis is dedicated to my parents:

Seok-Kyu Kum and **Romi Song Kum.**

Blank page

ACKNOWLEDGEMENTS

I express my sincere gratitude and appreciation to Professor William G. Hoover for his interest, guidance, assistance, and wonderful teaching technique (his directions and expectations were almost always true) throughout my studies at the University of California, Davis. His incessant eagerness to seek the truth and assiduous and sincere life style will be a milestone for my future. I wish to express thanks to Professor William G. Hoover and his wife, Dr. Carol G. Hoover for inviting my family to the trip to Henry W. Coe Park and to the concert at the Lick Observatory. The overnight at the peak of Red Skunk became a big memory for my family.

I thank Dr. Alan J. Spero (Lawrence Livermore National Laboratory) for his idea of this project, his useful and constructive comments of this work, and his help in obtaining financial support. I thank Dr. Eugene W. Burke (Lawrence Livermore National Laboratory, A division) for supportive administration of my guest student status.

I thank my thesis committee, Professor Donald A. McQuarrie (Chemistry Department), Professor Garry H. Rodrigue (Department of Applied Science), and Dr. Doug S. Miller (Lawrence Livermore National Laboratory, A-division) for their careful reading and many valuable comments. I wish specially again to thank Professor Garry H. Rodrigue for providing the valuable Supercomputer account and DB Annex account.

I thank Professor Harald A. Posch (University of Vienna, Austria), Dr. Brad Holian (Los Alamos National Laboratory), Dr. Bill Ashurst (Sandia Laboratory), and Carol G. Hoover (Lawrence Livermore National Laboratory) for useful and constructive comments on many aspects of this work and Jeff W. Swegle (Sandia Laboratory) for kindly providing a copy of his unpublished Sandia Corporation report.

I have enjoyed the years I have spent studying with the following Professors in the Department of Applied Science and Physics Department: William G. Hoover (Nonequilibrium statistical mechanics and Chaos), Garry H. Rodrigue (Numerical methods and seminars), Richard Christensen (Continuum mechanics), William McCurdy (Statistical mechanics), Frederick Wooten (Ph.D seminar), Nelson Max (Computer graphics seminars), Ling-Lie Chau (Mathematical Physics), Glen W. Erickson (Quantum mechanics), and Roderick V. Reid (Electricity and Magnetism).

I thank Professors Ann Orel (Quantum mechanics) and David Q. Hwang (Electricity and Magnetism) for employing me as the reader for their classes.

I thank Professor John S. De Groot, Professor Frederick Wooten (Department of Applied Science), Professor Rajiv R. P. Singh (Physics Department), Professor Joel E. Keizer (Chemistry Department), and Professor Harry A. Dwyer (Mechanical and

Aeronautical Engineering Department) for serving as Committee members of my Oral Examination.

Many others, especially secretaries of my Department, Ms. Barbara Smith, Ms. Hellen Franklin, Ms. Archietta Johnson, Ms. Estelle Miller, and Ms. Donna Clifford, were very helpful during the course of my graduate work and I thank them. I thank Mr. Stephen Moon (and his family) for their numerious help with academic and life affairs at the Rhonewood Apartments in Livermore.

On the Korean side, I thank Mr. Hak-Ok Kim, former President of Agency for Defense Development, Korea, for his permission to pursue my Ph.D. study. I would like to thank Dr. Ki-Bok Hahn for his recommendation and continued administration.

I wish to acknowledge the financial support over the last three academic years (from 1992 to 1995) from the Agency for Defense Development, Korea, and a two academic-year grant (from 1993 to 1995) from Lawrence Livermore National Laboratory through an Interuniversity Transfer Agreement.

I thank many members of KAA (Korean-American Association at the Lawrence Livermore National Laboratory), Dr. Francis Ree, Dr. Sang-Wook Kang, Dr. Sang K. Sheem, Dr. Choong-shik Yoo, Dr. Dae Hyun Chung, Dr. Sangbong Lee, Dr. Heung-Rae Lee, Dr. Jinwon Kim for their helpful guidance and inviting my family to their houses.

My mother, Romi Song Kum, my wife, Woon Hyun, and my two sons, Hyun Woong and Hyun Seong have always been a great source of strength during the course of this work and I thank them.

Oyeon Kum.
Livermore, California.
July 1995.

Table of Contents

page

List of Figures

page

List of Tables

Blank page

Oyeon Kum
September 1995
Applied Science

Nonequilibrium Flows with Smooth Particle Applied Mechanics

ABSTRACT

Smooth particle methods are relatively new methods for simulating solid and fluid flows though they have a 20-year history of solving complex hydrodynamic problems in astrophysics, such as colliding planets and stars, for which correct answers are unknown. The results presented in this thesis evaluate the adaptability or fitness of the method for typical hydrocode production problems.

For finite hydrodynamic systems, boundary conditions are important. A reflective boundary condition with image particles is a good way to prevent a density anomaly at the boundary and to keep the fluxes continuous there. Boundary values of temperature and velocity can be separately controlled. The gradient algorithm, based on differentiating the smooth particle expressions for $(u\rho)$ and $(T\rho)$, does not show numerical instabilities for the stress tensor and heat flux vector quantities which require *second* derivatives in space when Fourier's heat-flow law and Newton's viscous force law are used.

Smooth particle methods show an interesting parallel linking them to molecular dynamics. For the inviscid Euler equation, with an isentropic ideal gas equation of state, the smooth particle algorithm generates trajectories isomorphic to those generated by molecular dynamics. The shear moduli were evaluated based on molecular dynamics calculations for the three weighting functions, B spline, Lucy, and Cusp functions.

The accuracy and applicability of the methods were estimated by comparing a set of smooth particle Rayleigh-Bénard problems, all in the laminar regime, to corresponding highly-accurate grid-based numerical solutions of continuum equations. Both transient

and stationary smooth particle solutions reproduce the grid-based data with velocity errors on the order of 5%. The smooth particle method still provides robust solutions at high Rayleigh number where grid-based methods fails. Considerably fewer smooth particles are required than atoms in a corresponding molecular dynamics simulations of Rayleigh-Bénard convection. Nevertheless, the smooth particle trajectories are essentially Newtonian trajectories, for particles with mass m, subject to an effective potential function $2Pn^{-2}w(r)$. Accordingly, high-pressure subsonic problems, with $v^2 << c^2$, cannot be reliably solved using this method. A further limitation of the method is its inability to treat free surfaces accurately.

Not just subsonic flows can be treated. Shock waves propagate very well in smooth particle systems. For the Richtmyer-Meshkov instability problem with a small amplitude interface perturbation, compared to the wavelength, the interface amplitude grows linearly and the growth rate agrees with the analytic value within 3%.

The smooth particle method promises to be of special interest whenever it is desirable to include fluctuations. Smooth particles also provide an interesting eddy viscosity for use in turbulence studies.

CHAPTER 1

INTRODUCTION

Blank page

Computer simulations describing physical many-body processes originated with Enrico Fermi at Los Alamos during the Second World War. With J. R. Pasta and S. M. Ulam he simulated the motion of a linear array, or "string", of atoms linked by nonlinear "spring" forces [1, 2]. In these experiments, Fermi emphasized the potential usefulness of computer simulation to the understanding of N-body systems. Statistical mechanics makes general statements about the diffusion of energy and equipartition among modes, and Poincáre's Theorem suggested that all accessible points in phase space will be approached arbitrarily closely. Nobody before Fermi could state, without calculating it, what such a string, started out with a pure sinusoidal displacement, would look like after a few thousand oscillations at its fundamental frequency.

Theoretical Physics – Classical Mechanics, Thermodynamics, Statistical Mechanics, Electricity & Magnetism – provides a basis for the macroscopic description of matter. However, the complexity of real problems (for example, the splendor of real waterfalls, the violence of burning high explosives and hyper velocity impacts, the complexity of supersonic flow around projectiles, and the changing of the weather) makes them all hard to predict. Practical descriptions of these problems are difficult. Computer simulation is essential to understanding physics and engineering problems with many nonlinearly interacting degrees of freedom.

Due to the fast development of electronic technologies, computer hardware has developed rapidly during last four decades. Now inexpensive workstations capable of dealing with millions of degrees of freedom are readily available and massively–parallel computer simulations with billions of degrees of freedom are becoming routine. Computer simulation is now a widespread research and development tool impacting both theory and experiment. Simulated computer experiments, both real or imagined, can be a substitute for, or an enrichment of, true laboratory experiments. Computer simulation describes physical processes involving real materials with a simplified conceptual model capturing the essentials of the material behavior and revealing interesting features of the flow.

Simulations can be carried out purely at the microscopic level, treating the motion of individual atoms, or purely at the macroscopic level, treating the motion of a continuum. Atomic level computer simulation, called Molecular Dynamics (MD) solves the ordinary differential equations for the time development of particles making up the system. The articles in the Reference[3], "Nonequilibrium Molecular Dynamics at Livermore and Los Alamos", and "Nonequilibrium Molecular Dynamics: the first 25 years" [4], monograph, "Molecular Dynamics" [5], and a book, "Computational Statistical Mechanics" [6], all written by Professor William G. Hoover, include summaries of the history and state of the art of Molecular Dynamics simulations.

Independently of microscopic simulation techniques, computers have been used to simulate macroscopic phenomena using the Finite–Difference, Finite–Element, and Finite-Volume methods. Description at the macroscopic level requires the solution of partial differential equations for both the space and time dependence of the " field variables " (density, velocity, energy density) and their fluxes. The additional complexity of partial differential equations for a continuum has spawned a variety of computational methods. These methods, microscopic or macroscopic, for solving differential equations depending upon time and space variables, are of two kinds, Eulerian (space-fixed) techniques or Lagrangian (comoving) techniques.

Macroscopic finite–difference methods involve three kinds of errors, numerical diffusion, numerical dispersion and finite resolution. Resolution errors can be minimized by improved computer speed and capacity but diffusion and dispersion errors are intrinsic to this method. In Eulerian simulations information moves through a fixed–in–space Eulerian grid. This approach contains information diffusion errors, poor representation of convective terms in the equations of motion for large deformation, and the lack of accurate tracking of interfaces separating moving materials.

On the other hand, Lagrangian methods do not have these disadvantages, but cannot be universally applied because the material deformations are sometimes so large that the Lagrangian grid becomes severely distorted and the calculation breaks down. In order to treat chaotic (turbulent) mixing phenomena in nonlinear equations of continuum mechanics, exact interface tracking and freedom from mesh tangling are needed. One grid-free method for treating turbulent fluid flow is the Free-Lagrangian method [7]. The main concept of underlying the Free-Lagrangian method is that it has no actual mesh. The grid points nominally move with the fluid velocity.

Smooth Particle Applied Mechanics (SPAM), the focus of this thesis, [8, 9] is a grid-free Lagrangian technique which is appealing as a possible alternative to the grid-based numerical techniques currently used to analyze high deformation impulsive loading events. SPAM is a method designed to simulate problems in continuum mechanics with techniques resembling molecular dynamics.

The first use of particles to solve a flow problem originated in Harlow's particle-in-cell method. The method was developed to compensate for some deficiencies of the Eulerian method. He could follow the moving interfaces easily with this method since each material could be represented by an independent set of particles. This method uses the two different grids, a moving Lagrangian particle grid and a fixed Eulerian grid to calculate spatial derivatives using a finite difference method. Because of the inconvenience of dealing with two different kinds of grid, this method has a disadvantage in real computer simulations. Smooth Particle Applied Mechanics, originally called Smooth Particle Hydrodynamics, but applicable to solids and also to fluids other than water, developed from two equivalent sources: J. J. Monaghan [10] developed an improved particle-in-cell method with a truly grid-free Lagrangian method, and Lucy [11] approximated integral (Monte-Carlo integration) representations of spatial differential equations in order to solve the problem of rotating star bifurcation.

The basic idea of smooth particle applied mechanics is to replace the described material by a set of distributed ("Smoothed") particles, associating a mass, density, pressure-tensor, heat flux vector, and energy with each particle. The right hand side spactial derivatives in the conservation equations are converted to analytic forms using a smoothing function so as to follow the motion of mass, momentum, and energy by solving ordinary differential equations, equivalent to, but simpler than, the partial differential equations of conventional Lagrangian continuum mechanics.

SPAM has already been applied successfully to a number of astrophysical problems, and has been compared to adaptive grid techniques so that some of its strengths and weakness are known. However, much remains to be done. It is still hard to assess the adaptibility or fitness of this method for usual solids and fluids using complex astrophysical results with no comparison to exact solutions.

Here, the fitness of the smooth particle method for solid and fluid problems is evaluated for two known problems, Rayleigh-Bénard convection and Richtmyer-Meshkov instability. By comparing a set of smooth particle Rayleigh-Bénard problems, all in the laminar regime, to corresponding highly-accurate grid-based numerical solutions of the continuum equations, we find velocities within a few percent. By simulating shock waves propagating in a perturbed two phase system, we reproduce the known linear interface growth rate within a few percent. The role of boundary conditions is emphasized throughout.

This thesis consists of nine chapters. In Chapter II, we introduce the basic formulae of continuum mechanics and SPAM and compare these with the other numerical methods from the mathematical point of view. Chapter III describes numerical methods, including the use of image particles to model a reflecting boundary condition. In Chapter IV, we discuss fluctuations, time reversibility, and consider different types of hydrodynamic instabilities. We also discuss the isomorphism of microscopic molecular dynamics and macroscopic smooth particle trajectories. Chapter V is devoted to describing the simulation results of the Rayleigh-Bénard instability problem. In Chapter VI, we discuss the generation of the shock waves using the Smooth Particle method as well as the propagation properties of shock waves. In Chapter VII, we discuss the Richtmyer-

Meshkov instability, the Rayleigh-Taylor instability induced by shock impulsive forces. Chapter VIII treats Turbulence in homogeneous shear flows *via* Microscopic and Macroscopic Smooth Particle Applied Mechanics. Finally, in Chapter IX, we conclude with a summary and several recommendations.

References

[1] S. Chandrasekhar, "Stochastic problems in physics and astronomy", Review of Modern Physics **15** (1943) 1.

[2] J. L. Tuck and M. T. Menzel, "The superperiod of the nonlinear weighted string (FPU) problem", Advances in Mathematics **9** (1972) 399.

[3] M. Mareschal and B. L. Holian, editors, **Microscopic simulations of complex hydrodynamic phenomena**, NATO ASI Series **292** (Plenum Press, New York, 1992).

[4] W. G. Hoover, "Nonequilibrium molecular dynamics: the first 25 years", Physica A **194** (1993) 450.

[5] W. G. Hoover, **Molecular dynamics**, Lecture Notes in Physics **258** (Springer-Verlag, Berlin, 1986).

[6] W. G. Hoover, **Computational statistical mechanics** (Elsevier, Amsterdam, 1991).

[7] H. E. Trease, M. J. Fritts and W. P. Crowley, editors, **Advances in the free-lagrangian method**, Lecture Notes in Physics, **395** (Springer-Verlag, Berlin, 1991).

[8] W. G. Hoover, T. G. Pierce, C. G. Hoover, J. O. Shugart, C. M. Stein, and A. L. Edwards, "Molecular dynamics, smoothed-particle applied mechanics and irreversibility", Computers and Mathematics with Applications **28** (1994) 155.

[9] O. Kum and W. G. Hoover, "Time-reversible continuum mechanics", Journal of Statistical Physics **76** (1994) 1075.

[10] J. J. Monaghan, "Smoothed particle hydrodynamics", Annual Review of Astronomy and Astrophysics **30** (1992) 543.

[11] L. B. Lucy, "A numerical approach to the testing of the fission hypothesis", Astronomical Journal **82** (1977) 1013.

CHAPTER 2

BASIC CONCEPTS OF SMOOTH PARTICLE APPLIED MECHANICS

Blank page

2.1 Introduction

Smooth Particle Applied Mechanics (SPAM) is an alternative name for conventional Smooth Particle Hydrodynamics (SPH) suggested by W. G. Hoover, which recognizes the inherent characteristics of the method [1,2]. There is no change in the basic idea. The SPAM name is more appropriate for the method than the conventional one because the method has its own characteristics which can be applied to systems more general than "hydro" (water) problems.

We begin in Section 2.2 with a short summary of the Lagrangian form of the conservation equations for mass, momentum, and energy. In Section 2.3, we describe the basic idea of smooth particle applied mechanics using three different smoothing functions: the B spline, Lucy, and Cusp weighting functions. We also derive the smooth particle hydrodynamic form of the conservation equations. Finally, in Section 2.4 we compare the smooth particle method to the conventional Free-Lagrangian method and Finite Element method.

2.2 Continuum equations of motion [3,4]

Smooth Particle Applied Mechanics is designed to solve problems in continuum mechanics. This includes heat flow, fluid flow or hydrodynamics, and deformable solid mechanics. Here, we review the fundamental equations of continuum mechanics which apply to all these cases. Continuum mechanics starts with the definitions of a local density $\rho(r,t)$, velocity $\mathbf{u}(r,t)$, energy per unit mass $e(r,t)$, stress tensor $\sigma(r,t)$, and heat flux vector $Q(r,t)$, that are differentiable functions of space and time. The distributions of mass, momentum, and energy are idealized to be sufficiently smooth so that their spatial derivatives exist and satisfy differential conservation equations.

The continuity equation expresses the differential conservation of mass at a point in terms of the mass flux gradient there:

$$\partial\rho/\partial t \equiv -\nabla\cdot(\rho\mathbf{u}), \tag{1}$$

where ρ is mass density and $\mathbf{u}$ is flow velocity.

The same idea can be applied to the conservation of momentum:

$$\partial(\rho\mathbf{u})/\partial t \equiv -\nabla\cdot(\rho\mathbf{uu}) + \nabla\cdot\sigma + \rho\mathbf{F}, \tag{2}$$

where σ is the stress tensor. In the case of viscous fluid, $\sigma = (-p + \lambda\nabla\cdot\mathbf{u})I + \mu[\nabla\mathbf{u} + (\nabla\mathbf{u})^t]$, where p is the equilibrium pressure, I is the unit tensor, $\lambda + (2/D)\mu\ (\equiv \eta_v)$ is the D-dimensional bulk viscosity coefficient, μ is the shear viscosity coefficient, and $\mathbf{F}$ is the external force per unit mass. For an elastic solid stress is expressed in terms of strain rather than the strain rate $\nabla\mathbf{u} + \nabla\mathbf{u}^t$.

For the energy balance equation, we begin with the time dependent version of the First Law of Thermodynamics:

$$\Delta\dot{e} = \Delta\dot{q} - \Delta\dot{w}\ , \tag{3}$$

where $\Delta\dot{e}$ is the change of the system energy, $\Delta\dot{q}$ is the heat rate absorbed into the system, and $\Delta\dot{w}$ is the work rate done by the system.

The continuum energy conservation law, a time-dependent version of the First Law of Thermodynamics, is

$$(\partial/\partial t)[\rho\tilde{e} + (1/2)\rho\mathbf{u}^2] = -\nabla\cdot[\rho\mathbf{u}\tilde{e} + (1/2)\rho\mathbf{u}^3] + \nabla\cdot\sigma\cdot\mathbf{u} - \nabla\cdot Q, \tag{4}$$

where $\tilde{e}$ is the total internal energy, including potential energy due to external forces but not including the kinetic energy due to the flow velocity **u**, Q is the heat flux vector defined by Fourier's Law, $Q = -\kappa \cdot \nabla T$, κ is the heat conductivity, and T is temperature.

Using the comoving time derivative d/dt ($\equiv \partial/\partial t + \mathbf{u} \cdot \nabla$), we can derive the corresponding but simpler Lagrangian forms of the conservation equations:

$$d\rho/dt \equiv -\rho \nabla \cdot \mathbf{u}; \quad \text{(mass conservation)}, \tag{5}$$

$$\rho (d\mathbf{u}/dt) \equiv \nabla \cdot \sigma; \quad \text{(momentum conservation)}, \tag{6}$$

$$\rho de/dt \equiv \sigma : \nabla \mathbf{u} - \nabla \cdot Q; \quad \text{(energy conservation)}, \tag{7}$$

where e is purely internal energy due to the microscopic nature of material. It does not include any external energies, for example, potential energy due to gravity, surface energy due to surface force, or electro-magnetic energy due to electric and magnetic field, etc. Therefore, even if we add some external forces to the momentum conservation equation, the energy conservation equation does not need to be changed due to applied external forces.

Adding Fick's Law for mass transport of a multicomponent system, all macroscopic nonequilibrium effects can be described by solving these equations. Constitutive equations depending upon material properties are required to solve them.

2.3 Basic concepts of smooth particle applied mechanics [5-7]

The basic idea underlying Smooth Particle Applied Mechanics is the conversion of the continuum partial differential equations to ordinary differential equations. The spatial gradients are converted to analytic forms by using an interpolating weighting function which allows any function to be expressed in terms of its value at a disordered set of points – the particles. The interpolating weighting function is defined, for any function f(r),

$$\int f(r')\, w(r-r'; h)\, dr' \approx f(r) \equiv \sum (m_j/\rho_j)\, f(r_j)\, w(r-r_j; h), \qquad (8)$$

where the integration is over the entire space. In the summation r_j is a known point. The interpolating weighting function, w, has the following three properties:

$$\int w(r-r' ; h)\, dr'=1 \ ; \ \lim w(r-r' ; h)=\delta(r-r') \ ; \ w(r-r')=0 \ \text{ for } \ |r-r'| > h. \qquad (9)$$

In theory, when the limit is taken as $h \to 0$, the integral is replaced by a sum. It is important that the weighting function and its first derivative be as smooth as possible to avoid large errors in the numerical calculations. Therefore, the fundamental quantities in this method are the weighting function and its first derivative. Figure 2.1 shows three popular normalized weighting functions. and Figure 2.2 shows their corresponding first derivatives. For clarity we use two space dimensions though one advantage of the smooth particle method is its easy extension to three space dimensions.

1) The B-Spline Weighting function was introduced by J. J. Monaghan [8] and has been much used since:

$$w(0.0 < x < 0.5) = (c_s/h^D)\,(1 - 6\,x^2 + 6\,x^3) \ ; \ w(0.5 < x < 1.0) = (2c_s/h^D)\,(1 - x)^3, \qquad (10a,b)$$

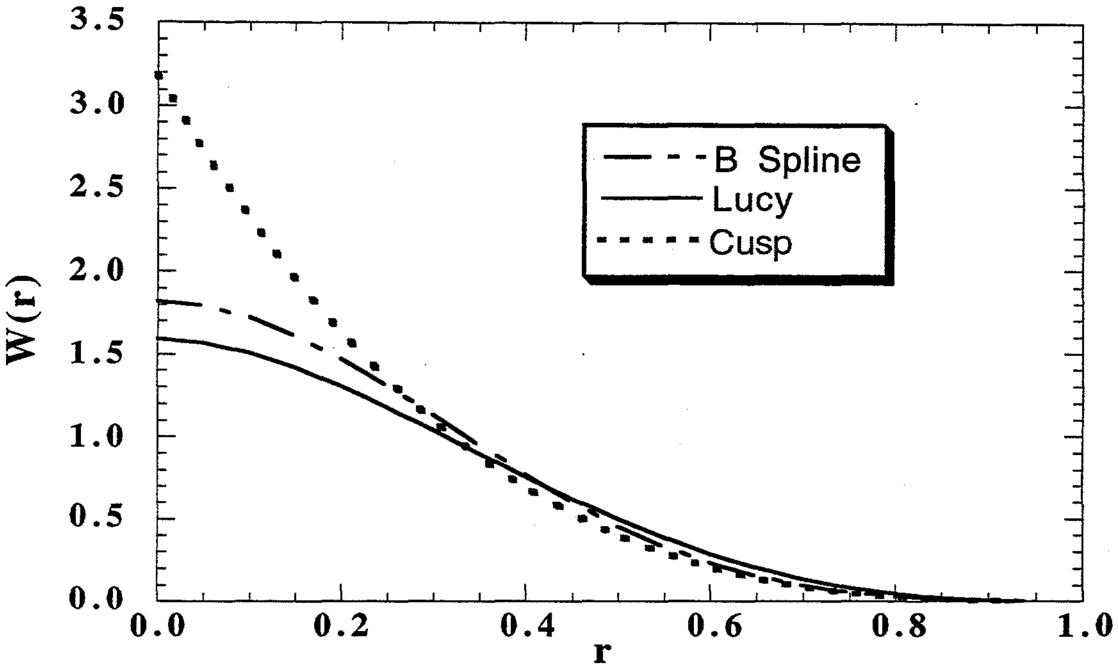

Figure 2.1 Three normalized weighting functions in two space dimensions: B spline, Lucy, and Cusp weighting functions.

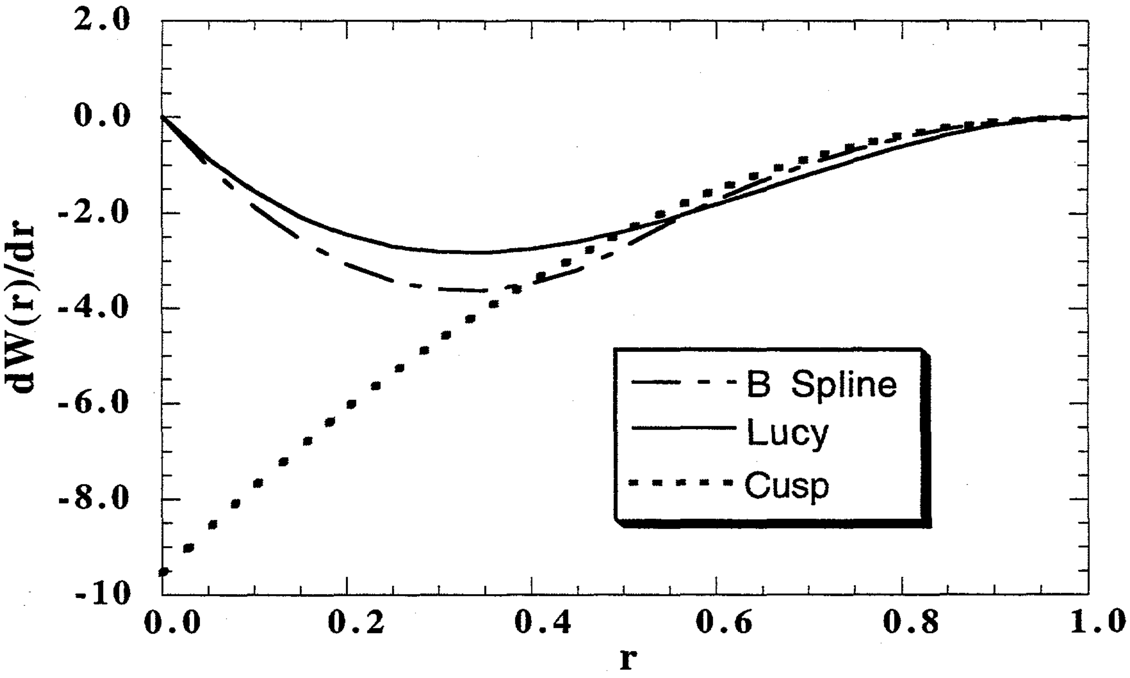

Figure 2.2 The first derivatives of normalized weighting functions shown in Figure 2.1.

where $x = |r_i - r_j|/h$, the pair particle distance divided by smoothing length. D is the dimension of the problem (1, 2, or 3), the normalization constant c_s is given by

$$c_s = 4/3 \ (D = 1)\ ;\ c_s = 40/(7\pi) \ (D = 2)\ ;\ c_s = 8/\pi \ (D = 3).$$

2) Lucy's weighting function [6], which he used in solving a rotating star bifurcation problem, is

$$w(0.0 < x < 1.0) = (c_L/h^D)\,(1 + 3x)\,(1 - x)^3, \tag{11}$$

where c_L is given by

$$c_L = 5/4 \ (D = 1)\ ;\ c_L = 5/\pi \ (D = 2)\ ;\ c_L = 105/(16\pi) \ (D = 3).$$

3) The cusp weighting function [1] is

$$w(0.0 < x < 1.0) = (c_c/h^D)\,(1 - x)^3, \tag{12}$$

where c_c is given by

$$c_c = 2 \ (D = 1)\ ;\ c_c = 10/\pi \ (D = 2)\ ;\ c_c = 15/\pi \ (D = 3).$$

Since the infinitesimal volume in the integration can be replaced by the ratio of mass to density at that point, the integral interpolant is approximated by a summation interpolant in numerical work:

$$f(r) \equiv \Sigma\,(m_j/\rho_j)\,f(r_j)\,w(r - r_j;\,h), \tag{13}$$

$$\nabla f(r) \equiv \sum (m_j/\rho_j)\, f(r_j)\, \nabla w(r - r_j;\, h), \tag{14}$$

here the summation index j includes index i. The basic assumption that the summation points are distributed in an uncorrelated way as h approaches zero needs to be checked. As discussed by Lucy (1977) this integration method resembles Monte-Carlo evaluation of integral.

The concept of a "particle" in Smooth Particle Applied Mechanics can be interpreted as an interpolation point rather an interacting point mass so that masses come from a continuous distribution rather than discrete points. No connectivity or spatial relation of points is assumed. In this sense the smooth particle method resembles the other approximate methods – Ritz, Galerkin, Petrov-Galerkin, least squares, and collocation methods [9]. We will discuss the smooth particle integration in detail in the next section.

Equation (14) provides a straightforward approximation for any spatial gradients which may be required in implementing the smooth particle algorithm. However, variants of this relation are sometimes used which start from the identities:

$$\nabla f(r) = (1/\rho)\,[\nabla(\rho f) - f\nabla\rho]\,;\ \nabla f(r) = \rho\,[\nabla(f/\rho) + (f/\rho^2)\nabla\rho]. \tag{15a,b}$$

Equation (15a) is a useful form for the calculation of *gradients* of physical variables, for example, shear rate, gradient of velocity, or heat flux, temperature gradient. Equation (15b) is a useful form of calculation of *conserved* quantities expressed by divergence, for example, force and divergence of heat flux.

Replacing the function f by ρ in equation (13), the density is,

$$\rho(r) = \sum m_j\, w(r - r_j\,;\, h). \tag{16a}$$

We can calculate the comoving time derivative of density directly from (16a) using the chain rule. Alternatively, use equations (5) and (14), with the identity $(\rho\nabla\mathbf{u})\,[\equiv(\nabla(\rho\mathbf{u})-\mathbf{u}\nabla\rho)]$, where f is replaced by $\mathbf{u}$ in equations (15a). Both approaches give the same result:

$$d\rho(r_i)/dt = \sum m_j\,(\mathbf{u}_j-\mathbf{u}_i)\cdot\nabla w_{ij}\ , \tag{16b}$$

where ∇w_{ij} is the gradient of $w(r_i - r_j\ ;\ h)$ taken with respect to the coordinates of particle i.

The smooth particle version of the continuum equation of motion (6) using (15b) and (14) with f replaced by σ gives

$$(d\mathbf{u}/dt)_i = \sum m_j\,[(\sigma/\rho^2)_j + (\sigma/\rho^2)_i]\cdot\nabla w_{ij}\,. \tag{17}$$

To derive the conservative smooth particle energy equation, we use (15a) and (14) in the work term $\sigma{:}\nabla\mathbf{u}$ with the identity of $(\sigma/\rho^2){:}(\rho\nabla\mathbf{u})\,[\equiv(\sigma/\rho^2){:}(\nabla(\rho\mathbf{u}) - \mathbf{u}\nabla\rho)]$,

$$(de/dt)_i = -(\sigma/\rho^2)_i \sum m_j\,\mathbf{u}_{ij}\cdot\nabla w_{ij} + (de/dt)_{heat}. \tag{18}$$

Applying equations (15a) and (14) with the identity $(\sigma/\rho){:}\nabla\,\mathbf{u}\ [\equiv\nabla\cdot\{(\sigma/\rho)\cdot\mathbf{u}\} - \mathbf{u}\cdot\nabla\cdot(\sigma/\rho)]$ gives likewise

$$(de/dt)_i = -\sum m_j\,(\sigma/\rho^2)_j\,\mathbf{u}_{ij}\cdot\nabla w_{ij} + (de/dt)_{heat.} \tag{19}$$

Averaging the two equations (18) and (19) then gives the symmetric form:

$$(de/dt)_i = -(1/2)\sum m_j\,[(\sigma/\rho^2)_j + (\sigma/\rho^2)_i\,]\,\mathbf{u}_{ij}\cdot\nabla w_{ij} + (de/dt)_{heat}. \tag{20}$$

Finally, including the heat conduction term, $(de/dt)_{heat}$ explicitly, the complete energy equation is, using equations (7), (15b), and (14),

$$(de/dt)_i = -(1/2) \Sigma m_j [(\sigma/\rho^2)_j + (\sigma/\rho^2)_i] \mathbf{u}_{ij} \cdot \nabla w_{ij} - \Sigma m_j [(Q/\rho^2)_i + (Q/\rho^2)_j] \cdot \nabla w_{ij} . \quad (21)$$

This form of energy equation conserves the total energy, $\Sigma[e + (1/2) u^2]_i$, exactly because the sum over indices i and j makes the equation anti–symmetric in the indices i and j.

2.4 Comparison with free-lagrangian and finite element methods.

Grid tangling occurs often in high-deformation turbulent problems solved in Lagrangian coordinates. Typical examples exhibiting grid tangling are hydrodynamic instabilities and shock/interface interactions. Lagrangian coordinates must be used for fluid flows with significant relative motion, particularly when the motion occurs across fluid interfaces.

Because these flows are characterized by large vorticity, the mesh distortion and grid tangling result in unacceptably large numerical errors. The Free-Lagrangian method, a method that does not use a mesh, was developed to avoid this difficulty [10].

Smooth Particle Applied Mechanics has many features in common with the Free-Lagrangian method. However, the Free-Lagrangian method uses the vertex or cell concepts made by the freely moving vertex points, which were used in conventional Lagrangian method. The Free-Lagrangian method incorporates control volume concepts. The control volumes are defined by sets of vertices. But Smooth Particle Applied Mechanics follows the Lagrangian scheme for treating the convective term, which is exactly the same method as molecular dynamics, without using grid or vertex concepts. Instead of control volume concepts, it uses smoothed kernel functions, which represent the local interaction range. In this sense, the vertex employed in the Free-

Lagrangian method and sample points in Smooth Particle method play similar roles in flows. Therefore, we can consider that Smooth Particle method has a cell centered scheme because all physical quantities are normally defined on a set of sample points. For example, if we pick the nearest neighbors in some way, we can use these points as vertices in a grid.

Moreover, the Smooth Particle method uses an interpolating function which is similiar to the Finite Element method or weak solution method [11]. J. W. Swegle derived the time variation of smooth Particle method following the Finite Element scheme [12]. In his derivation, he emphasizes the identity of the two methodologies. However, they are different in the sense that weighted residual methods employ an Eulerian scheme. From the physical or mathematical point of view, a weighted residual form of conservation equations is minimized to form a system of equations that can be integrated through time using the weighting function. Smooth particle equations also use a volume weighted sum to perform the spatial integration. Therefore, the Smooth Particle method can be viewed as a special case of the Finite Element method, where the connectivity of the elements is formed from a search for nearest neighbors. Comparison and rigorous derivation of these relations will help to analyze the Smooth Particle Method analytically.

2.5 Summary

The basic physical laws governing the behavior of fluid motion are the well known laws of mechanics - conservation of mass, Newton's equation of motion, and the laws of thermodynamics. These laws by themselves are not a complete description of material behavior. We use the appropriate constitutive equations - strain rate for the stress tensor, Fourier's law for heat transport, and Fick's law for the mass transport in a multicomponent system. The difficulties in these laws lie in their nonlinearities and are expressed finally in partial differential equations with respect to time and space variables.

The basic idea of Smooth Particle method is to convert the continuum partial differential equations to ordinary differential equations with respect to time. To convert them, we assume that all the physical variables are distributed smoothly in the system so that the variables at any point in the system can be calculated by interpolation using nearby values. Therefore we introduce a smoothly varying interpolation functions in such a way that partial derivatives with respect to space variables are converted to analytic forms containing the interpolation function and its first derivatives. We introduce the popularly used interpolation functions - B spline, Lucy, and Cusp interpolation functions.

The converted ordinary differential form of equations have the form of comoving time derivatives so that they are similiar in form to Molecular Dynamics equations of motion. Therefore, the time step integration corresponds to the direct movement of particles without considering separate advective or convective terms. It makes complex calculations very simple and easy: three dimensional problems are scarcely harder to program than one dimensional problems.

This method includes two old ideas, Free-Lagrangian and Finite Element methods: the Smooth Particle method is identical to Free-Lagrangian method if the given weighting function is applied at corresponding interpolation points. The identity with the Finite Element Scheme was derived by J. W. Swegle [12] by deriving the mass matrix in smooth particle method using the volume weighted sum integral approximation for the spatial integration. Smooth Particle method is thus a special case of Finite Element method, where the connectivity of the element is constructed by a search of nearest neighbors.

References

[1] W. G. Hoover, T. G. Pierce, C. G. Hoover, J. O. Shugart, C. M. Stein, and A. L. Edwards, "Molecular Dynamics, Smoothed-particle applied mechanics and irreversibility", Computers and Mathematics with Applications **28** (1994) 155.

[2] O. Kum and W. G. Hoover, "Time-reversible continuum mechanics", Journal of Statistical Physics **76** (1994) 1075.

[3] W. G. Hoover, **Computational statistical mechanics** (Elsevier, Amsterdam, 1991).

[4] D. A. McQuarrie, **Statistical mechanics** (Harper & Row, New York, 1973).

[5] R. A. Gingold and J. J. Monaghan, "Smooth particle hydrodynamics: theory and application to non-spherical stars", Monthly Notice of Royal Astronomical Society, **181** (1977) 375.

[6] L. B. Lucy, "A numerical approach to the testing of the fission hypothesis", Astronomical Journal **82** (1977) 1013.

[7] J. J. Monaghan, "Why particle methods work", SIAM Journal Scientific Statistical Computing **3** (1982) 422.

[8] J. J. Monaghan, "Particle methods for hydrodynamics", Computer Physics Reports **3** (1985) 71.

[9] C. A. J. Fletcher, **Computational galerkin methods** (Springer Verlag, New York, 1984).

[10] H. E. Trease, M. J. Fritts and W. P. Crowley, editors. **Advances in the free-lagrangian method**, Lecture Notes in Physics 395 (Springer, Berlin, 1991).

[11] J. N. Reddy, **An introduction to the finite element method** (McGraw-Hill, New York, 1984).

[12] J. W. Swegle, S. W. Attaway, M. W. Heinstein, F. J. Mellow and D. L. Hicks, **An analysis of smoothed particle hydrodynamics**, Sandia Report, SAND93 - 2513, UC - 705, (1994).

CHAPTER 3

NUMERICAL METHODS

Blank page

3.1 Introduction

In Chapter 2 we showed that an important advantage of the Smooth Particle method is the replacement of the continuum partial differential equations in space and time with ordinary differential equations in time. For the time integration the classic fourth-order Runge-Kutta method is a good choice because it retains good accuracy and computational speed compared to the other methods [1]. We describe the time integration method and computational procedures in Section 3.2.

Hydrodynamic conservation equations are not a closed set of equations until P(ρ, u, e) and Q(ρ, u, e) are specified. The constitutive equation for the stress tensor, the heat flux, as well as the initial and boundary condition must be specified. When the constitutive equations are applied to the continuum equations, for example, Fourier's heat flux vector to the energy equation, the continuum energy equation becomes a second order differential equation in temperature T. In Section 3.3, we discuss a method for treating the stress tensor and heat flux vector using the Smooth Particle method. We also describe related numerical instabilities and provide techniques for preventing them.

When the time integration is approximated with the classic fourth-order Runge-Kutta method, the major computational work is the search for interacting neighbor particles. In Section 3.4, we describe the three different algorithms for identifying the interacting neighbors. Direct searching algorithms require N(N−1)/2 number of calculations but almost all terms vanish because of the compactness of the weighting function. Neighbor-list algorithms use lists of interacting neighbor paticles list made at one time before calculating other physical variables. Computing time for this algorithm is proportional to NlnN but a relatively large memory space is used for lists of fluctuating neighbors. The linked-list algorithm [2] in which all neighbors in a given cell are linked in a list with the head particle number is the best method to compute the interacting forces. Computing time is proportional to NlnN and the required memory space is reduced.

Realistic systems are defined on a finite rather than infinite domain and contain boundaries. Boundaries play a critical role in the solution of both linear and nonlinear problems. The treatment of continuum boundary conditions with "particles" requires new methods. We illustrate the boundary methods with a surface tension problem in Section 3.5. We discuss the elastic shear modulus of the Smooth Particle method in Section 3.6. Section 3.7 includes a summary.

3.2 Numerical algorithms for SPAM

Smooth Particle Applied Mechanics converts the partial differential equations of continuum mechanics into ordinary differential equations with respect to time. One of the finite difference methods, the Method of (grid) Lines, also changes partial differential equations into ordinary differential equations. These two methods differ from each other in treating the convective terms in flow equations: SPAM uses Lagrangian coordinates and the Method of Lines uses Eulerian coordinates.

Numerical methods for solving ordinary differential equations are numerous and comparatively well developed. The most advanced methods in terms of efficiency, obtaining the most accuracy per unit of computational effort, are a group of methods invented by two German mathematicians, Runge and Kutta. The classic fourth-order Runge-Kutta (RK) method is widely used in the computer solution of ordinary differential equations. With this method the local truncation error is $O(dt^5)$ and hence, with a sufficiently smooth integrand, the global error is $O(dt^4)$ [1].

We checked the computational efficiency with our SPAM method using two different algorithms, the second order RK method and the fourth order RK method. To maintain the stability of the calculation we calculated the time step limit satisfying the "Courant condition", (dx/c), the information traveling time to the nearest neighbor, and the "diffusion time", $[(dx)^2/2\nu]$, together. We found that the fourth order RK method is more efficient than the second order RK method for time integration, even though the fourth order method requires twice as many force calculations per unit time step, because the ratio of allowed maximum time step dt, for stability, is greater than two.

Solution methods for SPAM closely resemble Molecular Dynamics techniques. However, SPAM solves three ordinary differential equations {dr/dt, dv/dt, and de/dt} while MD solves only two {dr/dt, and dv/dt}.

SPAM has several additional complexities [3]. First, the form of the weighting function and its range depends upon the judgment of the investigator. The solution can be sensitive to these arbitrary choices. We discuss this point in section 3.3 along with boundary conditions. Second, the accelerations depend upon more particle variables: the internal energy, the velocity gradient, plastic strain, and the like. The thermal equation of state, relating energy to temperature, and the mechanical equation of state, which gives the pressure, must be self-consistent and satisfy a Maxwell relation $\partial^2 A/\partial V \partial T = \partial^2 A/\partial T \partial V$. A(V,T) is the Helmholtz free energy. Third, rather than being derived from interatomic forces, the nonequilibrium constitutive properties (bulk and shear viscosity, heat conductivity, yield strength, surface force energy, ...) must be specified in advance. Fourth, in integrating the smooth particle equations of motion, three separate sums over pairs (rather than just the one sum needed in MD) must be carried out:

(1) Calculation of densities and equations of state.

(2) Calculation of heat flux and viscous stresses.

(3) Calculation of time derivatives of velocity and energy.

Finally, we integrate the velocity and energy derivatives using a Runge-Kutta method. Each step requires the completion of its predecessors. Figure 3.1 shows a simple flow chart. Fifth, the forms of the hydrodynamic equations underlying the approximation also depends on judgment, and allow corresponding choices among alternative sets of partial differential equations.

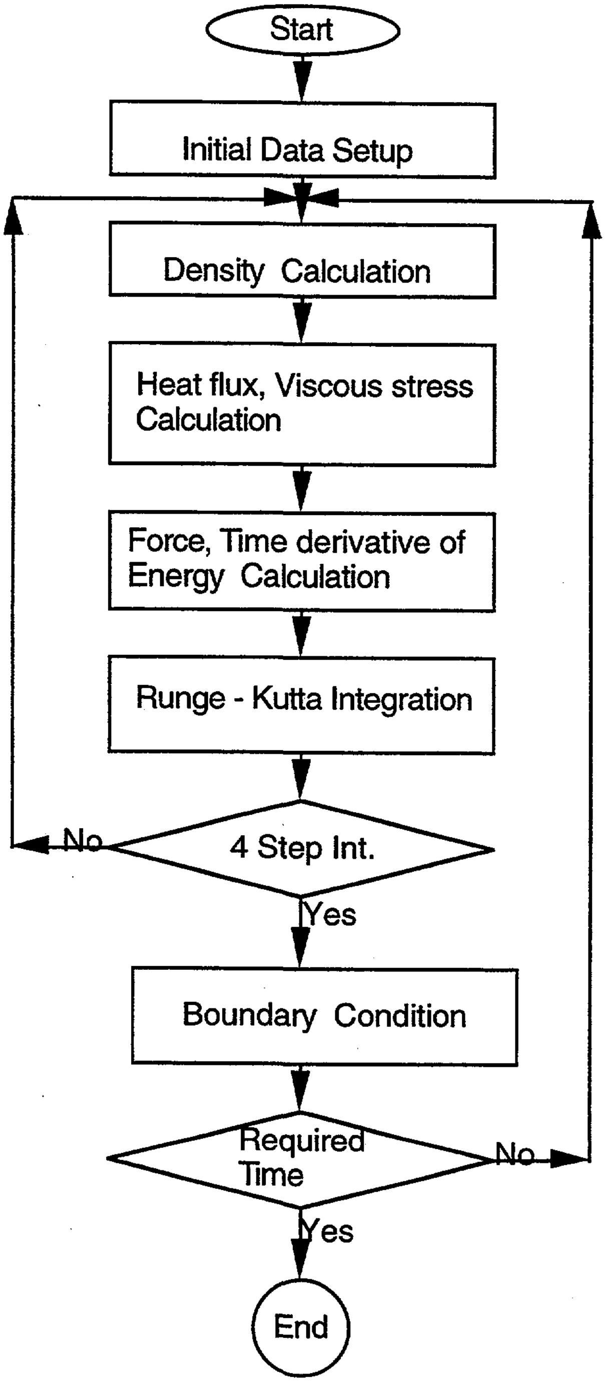

Figure 3.1 Simple flow of calculation

For instance, the density could be calculated by integrating the continuity equation, $d\ln\rho/dt = -\nabla\cdot\mathbf{u}$, rather than by summing the weighting functions. Likewise the heat flux and strain rates have several different alternative expressions [4,5].

For the approximation of heat flux and strain or strain rate terms, many difference forms of approximation to the differential equation are possible. Some of these forms are suitable. Others are not. In appearance, each step sum runs over all pairs of particles but actually it includes just a few dozen nearby interacting particles due to the imposed short range of the weighting function. Therefore a neighbor searching method is crucial to efficient Smooth Particle Applied Mechanics. We discuss the flux and neighbor calculations in detail in the following sections.

3.3 Computing heat flux and strain rate

Strain rate in the stress tensor and heat flux in the energy equation correspond to first derivatives in space according to Newton's viscous force law and Fourier's law respectively if we assume that viscosity and heat conductivity are independent of location. Smooth particle algorithms reproduce the first derivatives well but can cause numerical instability in second derivatives. J. J. Monaghan and L. Brookshaw used finite differente approximations to solve this problem [4,11] and Campbell suggested a different form to conserve the total fluxes [5]. Here we use a difference equation, equation (15a) in Chapter 2, based on differentiating the smoothed particle expressions for ($u\rho$) and ($T\rho$):

$$\nabla u = -\sum m_j \left[(u_i - u_j)/\rho_{ij}\right] \nabla w_{ij} \; ; \; \nabla T = -\sum m_j \left[(T_i - T_j)/\rho_{ij}\right] \nabla w_{ij} \, , \qquad \text{(1a,b)}$$

where the mean density ρ_{ij} can be chosen as the arithmetic or geometric mean of ρ_i and ρ_j. These difference forms of fluxes express the observation that no fluxes should occur if the two particles are in the same states. Otherwise the flux flows from the higher (u or T) state to the lower (u or T) state. On the other hand, if two particles are close enough to each other, then Taylor series expansion shows the identity with the difference equations. We applied these algorithms in our Smooth Particle Applied Mechanics and found that they are stable for all three different weighting functions. Numerical stability of the method is of course fundamental to numerical work. See J. W. Swegle' analysis [6].

3.4 Interacting neighbor search.

An important part of SPAM is an efficient algorithm to determine the particles within a specified distance of a given particle - those which give a non-zero contributions to interpolating sums. As we already mentioned in the previous section, SPAM requires three consecutive pair particle sums for each force calculation, twelve times for a fourth-order Runge-Kutta cycle. The simplest algorithm for summing over particles is;

```
SUM = 0.0
DO i =1,   Np-1
DO j = i+1 , Np
     SUM = SUM + P(i,j)
END DO
END DO
```

here Np is the total number of particles. This algorithm requires a long calculation with Np(Np − 1)/2 terms, but almost all of these vanish because of the compactness of the weighting function. One more efficient way is to make a neighbor table and to use it. Then the sum algorithm is;

```
SUM = 0.0
DO i =1,    Np-1
DO k =1,   nbr(i)
      j = inbr(i,k)
```

```
            SUM = SUM + P(i,j)
        END DO
        END DO
```

here `nbr(i)` is the number of neighbors of particle i and `inbr(i,k)` is the particle number of kth neighbor of the particle i. These are calculated in separate neighbor searching algorithm. Typically the maximum number of neighbors is fewer than 50. Most particles have fewer neighbors. Only i<j needs to be included in order to prevent a double calculation. This algorithm requires unnecessary memory and is not efficient in FORTRAN because FORTRAN has no flexible memory scheme. This algorithm takes a time proportional to NlnN for the fourth-order RK method, where N is the total number of particles.

A better algorithm for searching the neighbors with a compact weighting function is the linked list algorithm described by Hockney and Eastwood [2]. For this algorithm, we have to define two kinds of dimensioned variables, `IH(i)` is the highest particle number assigned to the cell i. `LL(i)` links all the particles in this cell in descending particle number order. We accomplish this by using the following algorithm:

```
DO  k = 1, ncell
    IH(k) = 0
END DO
DO  j = 1,    Np
    k = x(j)/dx + 1
    LL(j) = IH(k)
    IH(k) = j
END DO
```

where `x(j)` is, for example, the x coordinate of jth particle, ncell is the total number of cells, and dx is the cell length in the x direction. To use this algorithm, we first have to divide the whole system into many small cells with a size just exceeding the weighting function interaction range and assign the number to each cell and make a neighbor cell map which explains which pairs of cells can interact.

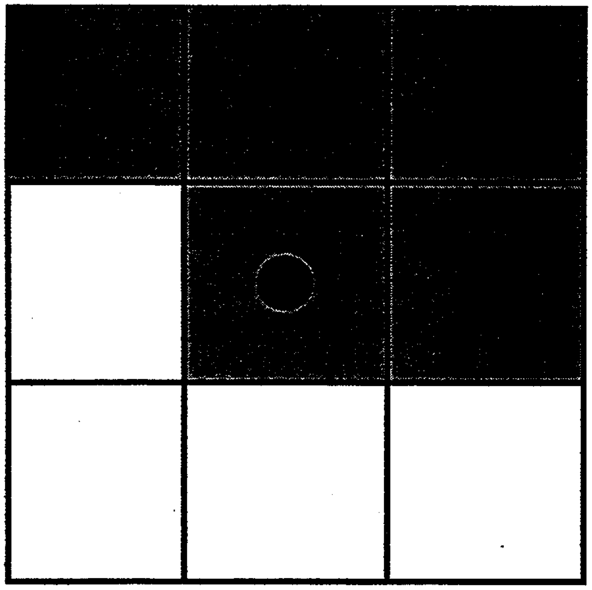

Figure 3.2 Neighbor cells of the black particle in the cell model. The black particle has nine neighboring cells but actually interacts with only five neighbor cells, including itself, indicated by shading, to prevent double pair calculation.

Figure 3.2 shows the neighbor cells of cell model in a two dimensional system for the linked-list algorithm. In the Figure, the particle marked by black dot interacts with the particles in the shaded cells. Finding the neighbor cells is done only once if the system does not change size or interaction ranges. Many workers have discussed variable smoothing lengths [7-12]. But we do not consider this problem here. With this step, we get a neighbor map for the i-th cell, say `NM(i,k)`. Now we are ready to do the neighbor sums,

```
SUM = 0.0
DO k =1,     ncell
   i = IH(k)
```

```
100     IF ( i > 0 ) THEN
           DO n =1,   nbc(k)
              j = IH( NM(k,n) )
200           IF ( j > 0 ) THEN
                  IF ( j = i )  GO TO 300
                  SUM = SUM + P(i,j)
                  j = LL(j)
                  GO TO 200
              END IF
300        END DO
           i = LL(i)
           GO TO 100
        END IF
     END DO
```

where `nbc(k)` is the neighbor cell number of the kth cell. We use `nbc(k)` variables because all cells do not have the same number of neighbor cells for reflective boundary problems. The neighbor map `NM(k,n)` does not occupy much memory because the total number of cells is much less than the total number of particles. Each cell has only a few neighbor cells (for example, the maximum is nine in two dimensions). This algorithm takes a time proportional to NlnN for an N particle system.

All macroscopic systems are finite so that boundary conditions and surface tension are important in a numerical algorithm. We discuss these in the next section.

3.5 Boundary conditions and surface tension.

To solve the partial differential equations, both initial and boundary condition are required.

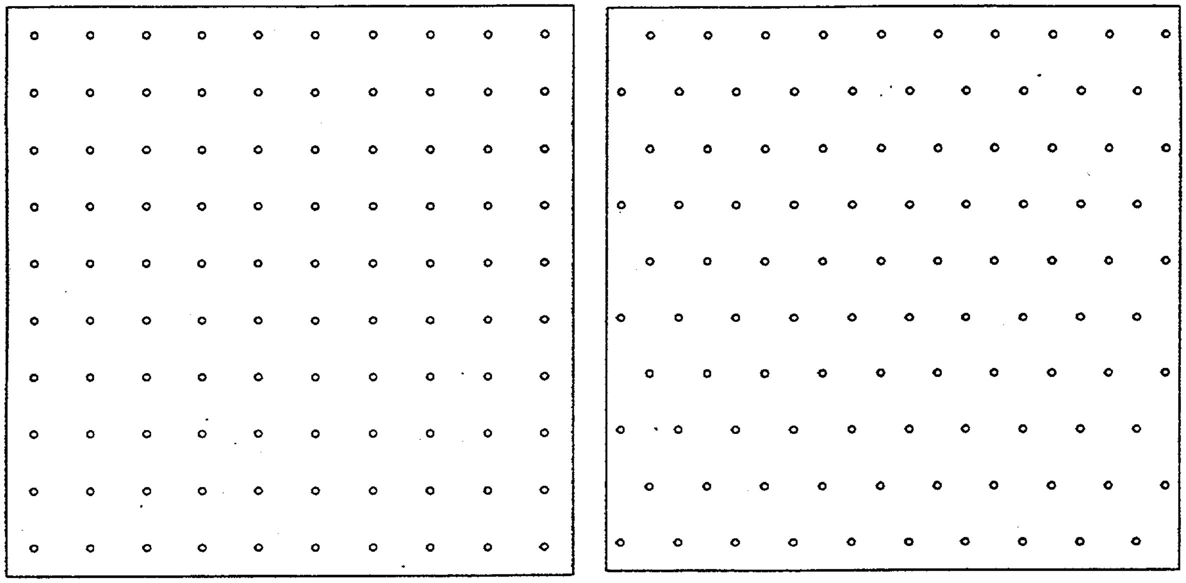

Figure 3.3 Simple initial conditions for a particle method: (a) square lattice system, (b) triangular system. In the smooth particle method, particles are not actual particles but rather interpolation points with known properties. For fluid simulations, even if the initial conditions are regularly spaced, all particles soon approximate the flow pattern.

Figure 3.3 shows simple initial spatial conditions, the square and triangular lattices. For fluids, even if the initial conditions are regularly spaced, all particles soon follow the flow. Boundaries are the critical link between the system of interest and the surroundings with which it interacts. In particle methods boundaries affect the equations of motion. Handling the boundary conditions and surface tension are important.

In the smooth particle case we have treated boundaries in three different ways. For an infinite system, we use periodic boundary conditions, which have no surface. Periodic

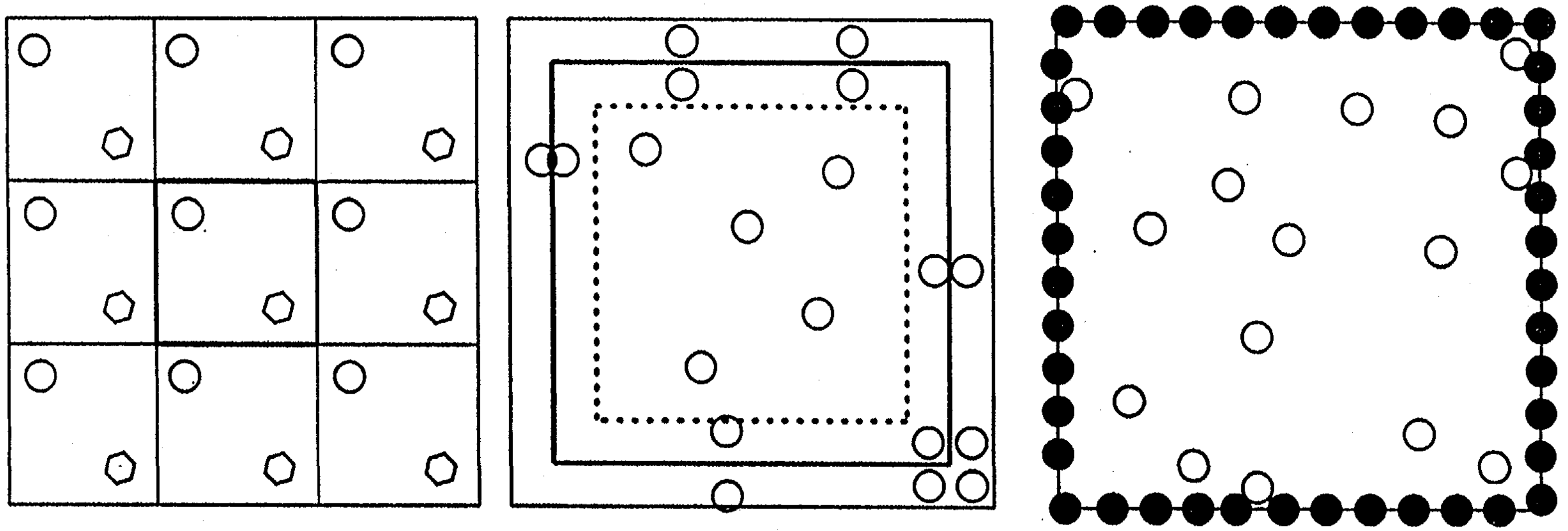

(a) (b) (c)

Figure 3.4 Three boundary systems used in particle method: (a) periodic boundaries. The real system is in the center and the neighboring systems are assumed to be made by duplications of the central system. The minimum neighboring distance principle is used in force calculations. (b) reflective boundary system with reflective image boundary particles. The real system is the box inside the solid lines. The interaction range is the distance between inside dashed lines and the inside solid lines. All the system particles outside the dashed lines spawn reflective image boundary particles. For the reflective boundary particles, their physical flow properties (heat flux and stress) are assumed the same as those of their respective system particles so that these properties are continuous across the system boundary. But the boundary can have controlled velocities and temperatures. (c) reflective system with fixed boundary particles. The boundary particles are fixed at given positions and have preassigned physical variables. Their main effect is to prevent the escape of particles through the system boundaries.

boundaries are usual in equilibrium Molecular Dynamic simulations [13]. Figure 3.4 shows three typical boundary conditions, periodic, reflective with image particles, and reflective with fixed boundary particles [3, 14]. The density sum, equation (16a) in Chapter 2, gives an undesirable decrease near the boundary if we have no special boundary treatment.

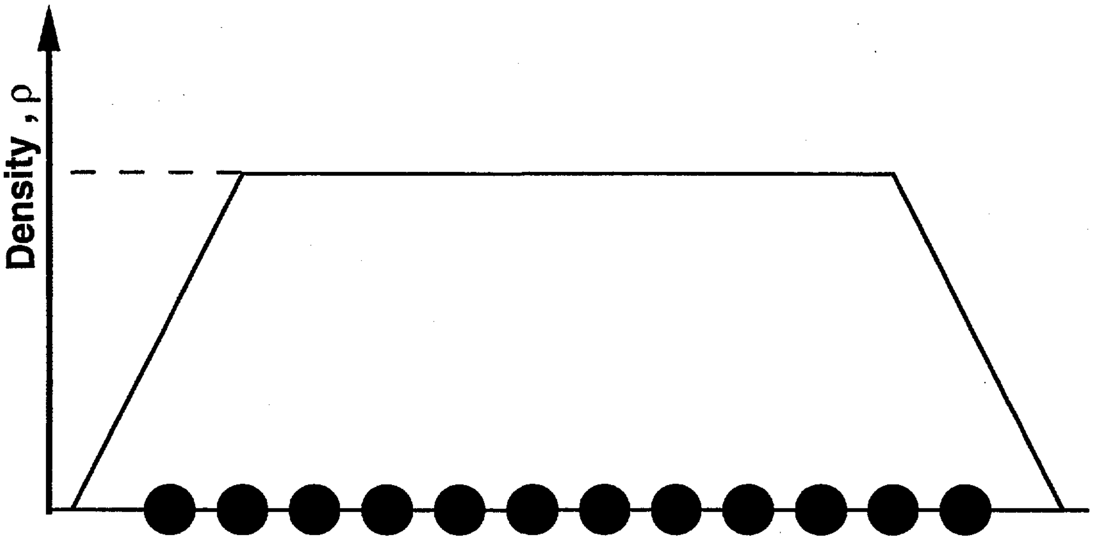

Figure 3.5 Density decrease in boundary regions in one dimension. The sharp decrease of density near the boundary gives the particles near the boundary region atypical and unphysical properties.

Figure 3.5 shows a graphical representation of the calculated density in one dimension from a set of equal masses, with an equal spacing of 0.4h, in which every particle within the system has four interacting neighbor particles. The boundary particles get a contribution from particles on only one side, rather than from both sides as in the interior, so that the calculated density decreases rapidly. The density sum (16a) in Chapter 2. thus results in boundary anomalies unless a special boundary treatment is implemented. This figure suggests why we need extra boundary particles in a finite system. An alternative is to solve the continuity equation directly using equation (16b) in Chapter 2.

Our trials with this approach in the two-fluid shock wave simulation (Riemann problem) gave disappointing results. We abandoned the continuity approach in this work.

Reflective boundaries with fixed boundary particles have also been used in particle methods including Molecular Dynamics. To compensate for the decreasing density near boundaries, sufficiently many particles fixed on the boundaries can provide a high density container capable of repelling approaching particles. These special boundary particles are treated in the same way as system particles in the density calculation but are fixed in space with preassigned physical variables. In this model, the physical variables are not continuous at the boundary.

A reflective boundary with image particles is a new method to make the physical variables continuous on the boundary in the Smooth Particle method. In this model, all the image boundary particles have the same physical stresses and fluxes as their respective system particles. But we control temperature and velocity for image boundary particles. In our work these controlled variables are assigned once and for all.

We consider the image particles as if they were real system particles (image particle numbers are counted consecutively following the last interior system particle). First, we calculate the density for each system particle using equation (16a) in Chapter 2. We assign the image particle density equal to the corresponding system-particle density. The density is thus continuous at the system boundary. Next, we calculate the interior velocity gradients and temperature gradients, which are needed to calculate the stress tensor and heat flux, using equations (1a) and (1b) respectively. With these gradient values, we calculate stress tensor and heat flux for all system particles and assign equal values to their respective image particles. Last, we calculate the acceleration and time derivative of energy using the same principles as before. The final time integration (Runge-Kutta algorithm) is evaluated only for the interior particles.

The image boundary algorithm is evaluated for an infinitesimal time step integration. The boundary particle's position varies with the respective system particle's position. Therefore, if we take a big time step, it is desirable to compute the boundary particle properties at each step in the Runge-Kutta integration algorithm. To calculate the new boundary particles is not expensive. It is proportional to the system surface $N^{1/2}$ in two dimensions. An advantage of the smooth particle approach is that the velocities and temperatures of the reflected boundary particles can be assigned independently of the other particles in their vicinity (even the mirror–image particles inside the system). Another method for handling boundary problems with the Smooth Particle algorithm can be found in Campbell's and Japanese work [5, 20].

It is difficult to treat internal boundaries too, across which two different kinds of material interact with each other. The surface forces and energies are important if the materials do not mix [14, 15]. SPAM usually has no surface tension while Molecular Dynamics include it automatically through the interatomic potential function.

From the molecular or atomic point of view, the free energy of molecules at a free surface is increased because they are surrounded by attracting neighbors in only a half space. Hence, the free energy of a fluid includes a term proportional to the volume and an additional term proportional to the area of free surface. If the surface energy is γ per unit area, γ is the surface tension. Extending the area by dS requires a work γdS. Thus the tendency of surface tension is to reduce all free surfaces toward minimum area. Small bubbles or fluid surfaces with a small radius of curvature are strongly influenced by surface tension.

In a macroscopic hydrodynamic system, the surfaces separating fluids are subject to forces arising from surface tension. At equilibrium, surface tension acts normal to the surface dS separating the two fluid elements. The force difference between the two sides is proportional to the surface tension. It is known that the pressure difference between the two sides of a surface element dS is proportional to the surface tension divided by the radius of the curvature. This follows from the microscopic free energy point of view [3]. In Smooth Particle Applied Mechanics, the forces are proportional to the gradient of the weighting function between the pair of particles. The curvature of the surface area can be considered inversely proportional to the weighted separations of nearby particle pairs. Therefore the surface tension of each particle has an additional force term of the form of $\Sigma\nabla W_{ij}/q_{ij}^2$ with some appropriate proportionality constant, where the sum includes all nearest neighbors. This form of force term guarantees that interior particles far from a free surface have no effect at all because the force term is antisymmetric in the indices i and j. This representation of surface tension looks reasonable but it has problems in simulation. We leave this as an open problem for the future.

3.6 Calculation of elastic constants.

In reference [16] we showed that the smooth particle equations of motion are equivalent to those of Molecular Dynamics for an isentropic ideal gas system, with an equilibrium pressure proportional to the density squared. Then the weighting function of the SPAM algorithm corresponds to a pair potential function from the Molecular Dynamics point of view. Smooth particles' trajectories are isomorphic to those of molecular dynamics for this isentropic ideal gas system. Since Molecular Dynamics includes elastic properties due to the potential, the Smooth Particle algorithm can have intrinsic elastic properties even though it has no explicit elastic constant in its stress tensor. Elastic properties of the system are described by the elastic constants $\{C\}$, which are the analogs of the bulk and shear moduli for a solid, in the linear Hooke's law relation linking the stress and strain tensors:

$$\sigma \propto \varepsilon. \tag{2}$$

The proportionality coefficients, which have units of stress, are the elastic constants. The adiabatic elastic constants $\{C^S\}$ determine the speed of propagating sound waves. The isothermal elastic constants $\{C^T\}$ describe the stresses required for isothermal deformations of these solids. For a general two-dimensional system, each of the three stress components $\{\sigma_{xx}, \sigma_{yy}, \sigma_{xy}\}$ responds to changes in the three elastic strains $\{\varepsilon_{xx}, \varepsilon_{yy}, \varepsilon_{xy}\}$, requiring an array of nine elastic constants to describe the linear response. For an isotropic system, the number of nonzero constants reduces to just four, among which only two are independent, C_{11}, and C_{12}. These two coefficients are equivalent to two Lame's constants, λ and η, which are related to the bulk and shear moduli, B and G: In two space dimensions,

$$\sigma_{xx} = C_{11}\varepsilon_{xx} + C_{12}\varepsilon_{yy} \; ; \; \sigma_{yy} = C_{12}\varepsilon_{xx} + C_{11}\varepsilon_{yy} \; ; \qquad (3a,b)$$

$$\sigma_{xy} = (1/2)(C_{11} - C_{12})\varepsilon_{xy} = \eta\varepsilon_{xy} \; ; \; C_{11} \equiv \lambda + 2\eta; \; C_{12} \equiv \lambda, \qquad (4a,b)$$

and in general, in D dimensions,

$$B \equiv \partial P/\partial \ln\rho = \lambda + (2/D)\eta \; ; G \equiv -P_{xy} / \varepsilon_{xy} = \eta, \qquad (5a,b)$$

where D is the dimensionality of the problem (2 or 3).

Two different ways of calculating the shear moduli are to calculate the change of potential energy (in Molecular Dynamic simulation) and the change of internal energy (in SPAM) [13]. The shear modulus due to energy change is given by

$$GV = 2\Delta E/\varepsilon^2, \qquad (6)$$

where G ($\equiv \eta$) is shear modulus, V is the volume, ΔE is the energy increase, and ε is the shear strain.

On the other hand, the coefficients C_{ij} can also be calculated indirectly from Gibbs canonical partition function by working out the Taylor series expansion of the internal energy or the Helmholtz free energy as a power series in the strains. The coefficients in the strain series are then obtained as equilibrium ensemble averages in the unstrained state. The detailed calculations are in references [17-19]. For example, at zero temperature,

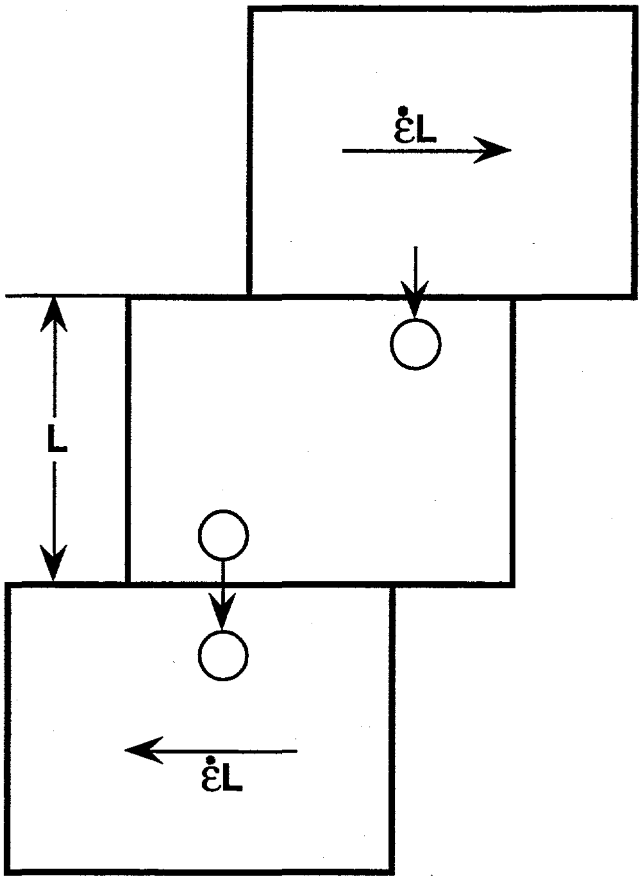

Figure 3.6 Numerical model of homogeneous shear with constant strain rate and periodic boundary condition in two space dimentions. The upper and lower boundaries move with the speed $\dot{\varepsilon}$ L in opposite directions so that the overall velocity profile is linear. If one particle moves through the system boundary it reenters at a different position. In the moving particle reference frame (comoving frame), the particle velocity does not change when it reenters in the system.

$$G = -C_{44} + P_{xx};\ P_{xx} = \Sigma\phi' x^2/r;\ VC_{44} = \Sigma(\phi'' x^2 y^2/r^2 - \phi' x^2 y^2/r^3), \qquad (7a,b)$$

where $\phi'(\equiv w')$ and $\phi''(\equiv w'')$ are the first and second derivatives of the weighting function respectively. In all, we have three different ways to obtain the moduli.

Our numerical model is shown in Figure 3.6. The system has a periodic boundary with horizontal boundaries of y-axes moving at a relative velocity of $\dot{\varepsilon}$ L. The particle velocities are linearly proportional to the end boundary velocities.

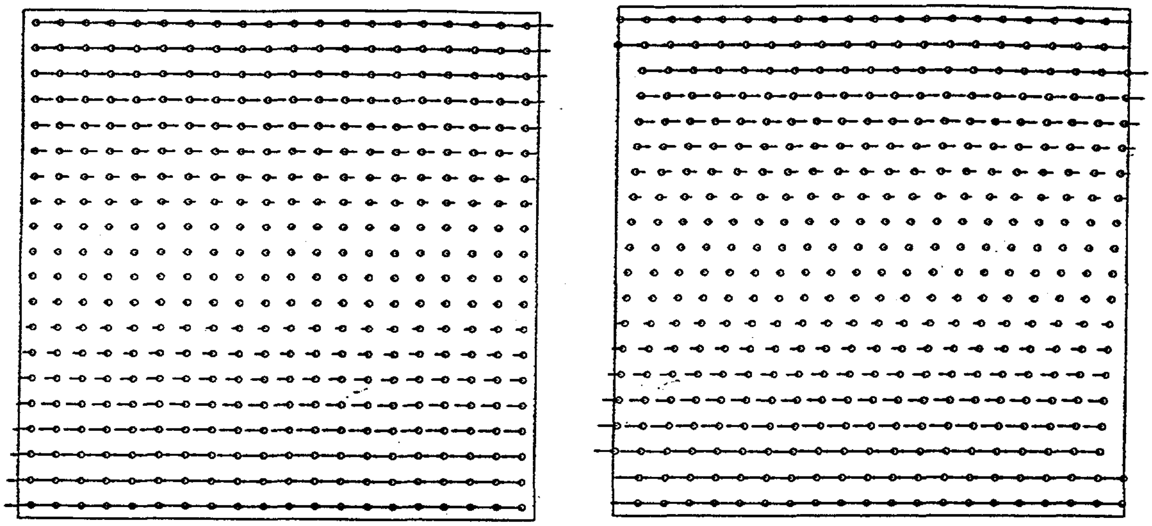

(a) (b)

Figure 3.7 Plane Couette flow with shearing model, Figure 3.6. (a) initial configuration of velocity field in square lattice system (20 x 20). (b) configuration at time t = 10. The strain rate is 0.005. We see the effect of the periodic boundary condition in the first and last rows. The calculation is done in the laboratory frame. Our dense fluid equation of state with the Lucy weighting function with smoothing length 3 are used. The total internal energy is 2977.2 (7.443 per particle) and the total kinetic energy is 0.665.

For the plane Couette flow, figure 3.7 (a) shows the initial condition. Figure 3.7 (b) shows a configuration of the system after an evolution of time (t = 10) giving a strain $\Delta x/\Delta y = 0.05$. We see the effect of the periodic boundary condition in Figure 3.7 (b).

The shear modulus results calculated from the three different methods described above, equation (6) and equation(7), all agreed with each other within maximum 3%.

Table I shows that the internal energy change does not depend on the shear rate for small slow deformations. Figure 3.8 shows energy increase as a function of strain for a small strain, equation (6). Table II contains the intrinsic shear moduli of SPAM for three different weighting functions with each of

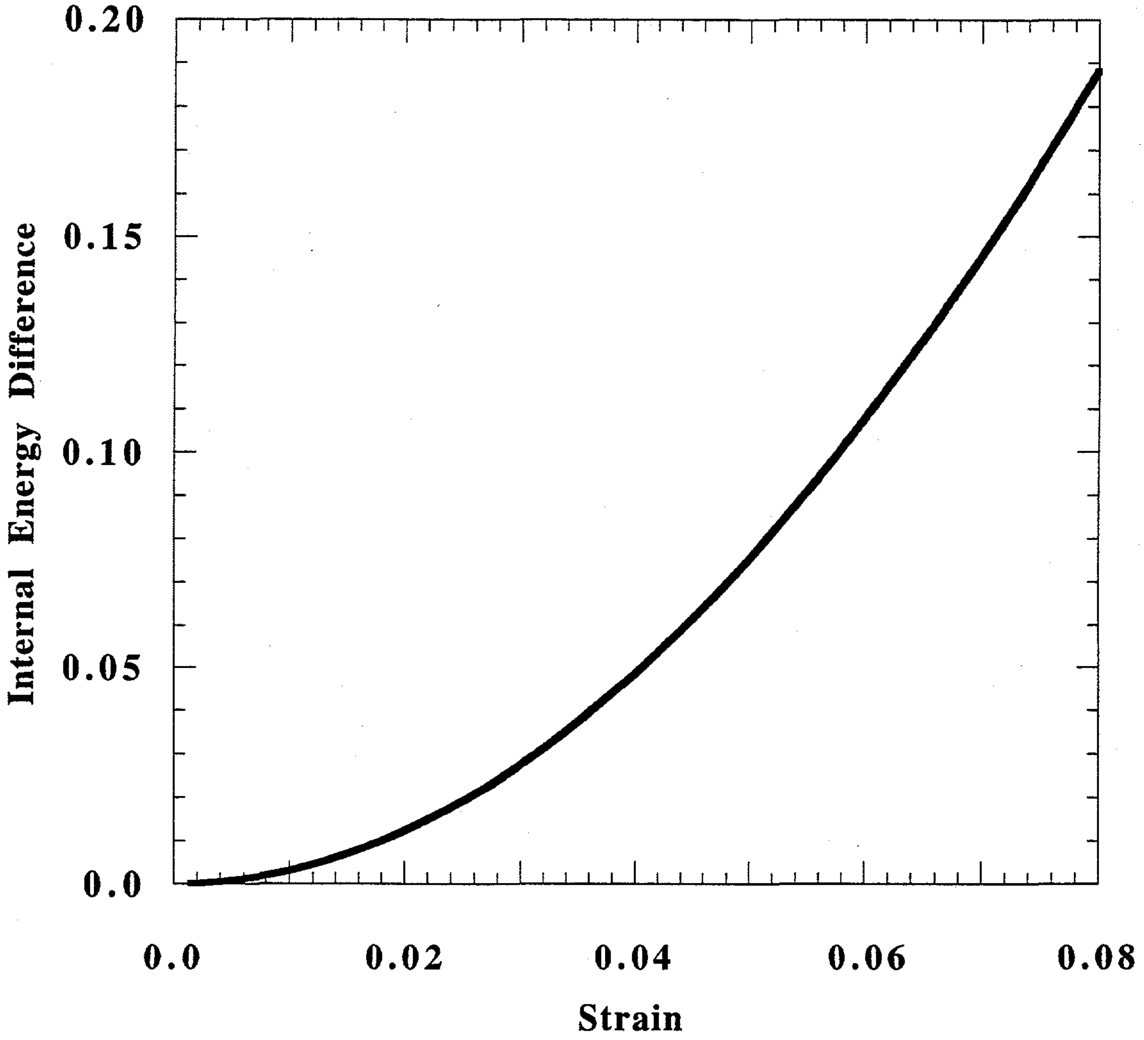

Figure 3.8 Internal energy difference as a function of strain in the elastic region. In the elastic region, the internal energy increase is essentially independent of the strain rate for rates less than 0.1. Square lattice structure of the unit reduced density with B spline weight function is used. See Table I.

Table I Internal energy change as a function of strain in three different strain rates $\dot{\varepsilon}$. Square lattice system of the unit density with B spline weighting function is used.

$\dot{\varepsilon}$ ε	0.1	0.01	0.001
0.01	0.003	0.003	0.003
0.02	0.012	0.012	0.012
0.03	0.027	0.027	0.027
0.04	0.047	0.048	0.049
0.05	0.074	0.075	0.075
0.06	0.106	0.108	0.108
0.07	0.144	0.146	0.146
0.08	0.186	0.188	0.189

Table II Shear modulus for three weighting functions and square lattice system as a function of smoothing length. Density of the system is unity.

Smoothing Length	Lucy	B spline	Cusp*
2.5	0.042	0.035	0.007
3.5	0.012	0.015	0.011
4.5	0.0032	0.0045	0.0045
5.5	0.0024	0.0024	0.0001

* For the Cusp weighting function, the shear modulus is 0.012 at a smoothing length 2.5 in the isosceles triangular lattice.

four different smoothing length for the square lattice system. For the Cusp weighting function, we calculated it also for the triangular lattice. The larger the smoothing length, the smaller the intrinsic shear modulus because we get the exact result if we include all interactions (information) for interpolation. For the same appropriate smoothing length, 2.5 ~ 3.5, the Cusp weighting function has the smallest shear modulus. Despite this desirable property, the Cusp function is not a good choice for SPAM because it fails to reproduce density well.

3.7 Summary

Given initial and boundary conditions, ordinary differential equations can be solved in many ways. We use the classic fourth order Runge-Kutta method, which is quite accurate, to carry out the Smooth Particle time integration. For still a different treatment of boundaries, using a continuous distribution of external particles, and different Runge-Kutta method, see Reference [20]. In this algorithm, the major computing work is the search for interacting neighbor particles. The Linked list algorithm, with computing time proportional to Nln(N) is used to find the neighbors in two space dimensions. Two typically used initial configurations of particles are described: the square and triangular lattices. Three different boundary conditions are described: periodic, reflective with fixed boundary particles, and reflective with image boundary particles. We showed that homogeneous shearing of the system with constant shear rate, which has been used in Nonequilibrium Molecular Dynamics, works well. We applied this model to the plane Couette flow to calculate elastic constants, shear modulus and Bulk modulus, in the small strain elastic range. In this calculation, the numerical value of the intrinsic fluid-phase shear modulus is not zero and depends on the weight functions. The modulus does approach zero for large interaction ranges.

References

[1] J. D. Hoffman, **Numerical methods for engineers and scientists** (McGraw-Hill, New York, 1992).

[2] R. W. Hockney and J. W. Eastwood, **Computer simulation using particles** (McGraw-Hill, New York, 1981).

[3] W. G. Hoover, T. G. Pierce, C. G. Hoover, J. O. Shugart, C. M. Stein, and A. L. Edwards, "Molecular dynamics, smoothed-particle applied mechanics and irreversibility", Computers and Mathematics with Applications, **28** (1994) 155.

[4] L. Brookshaw, "Solving the heat diffusion equation in SPH", Memorie *della* Societa Astronomica Italiana, **65** (1994) 1033.

[5] P. M. Campbell, **Some new algorithms for boundary value problems in smooth particle hydrodynamics**, Mission Research Corporation, DNA-TR-88-286 (1988).

[6] J. W. Swegle, S. W. Attaway, M. W. Heinstein, F. J. Mellow and D. L. Hicks, **An analysis of smoothed particle hydrodynamics**, Sandia Report, SAND 93 - 2513, UC - 705, (1994).

[7] M. Steinmetz and E. Müdler, "On the capabilities and limits of smoothed particle hydrodynamics", Astronomy and Astrophysics. **268** (1993) 391.

[8] L. Hernquist, "Some cautionary remarks about smoothed particle hydrodynamics", The Astrophysical Journal, **404** (1993) 717.

[9] P. Laguna, W. A. Miller, and W. H. Zurek, "Smoothed particle hydrodynamics near a black hole", The Astrophysical Journal, **404** (1993) 678.

[10] P. J. Mann, "Smoothed particle hydrodynamics applied to relativistic spherical collapse", Journal of Computational Physics **107** (1993) 188.

[11] J. J. Monaghan, "Smoothed particle hydrodynamics", Annual Review of Astronomy and Astrophysics **30** (1992) 543.

[12] W. G. Hoover, **Computational statistical mechanics** (Elsevier, Amsterdam, 1991).

[13] W. G. Hoover, "Nonequilibrium molecular dynamics at Livermore and Los Alamos", in **Microscopic simulations of complex hydrodynamic phenomena**, edited by M. Mareschal and B. L. Holian, (Plenum Press, New York, 1992).

[14] L. Rosenhead editor, **Laminar boundary layers** (Oxford, London, 1966).

[15] S. Chandrasekhar, **Hydrodynamic and hydromagnetic stability** (Oxford, London, 1961).

[16] O. Kum and W. G. Hoover, "Time-reversible continuum mechanics", Journal of Statistical Physics **76** (1994) 1075.

[17] D. R. Squire, A. C. Holt and W. G. Hoover, "Isothermal elastic constants for argon. theory and monte-carlo calcualtions", Physica **42** (1969) 388.

[18] W. G. Hoover, A. C. Holt and D. R. Squire, "Adiabatic elastic constants for argon. theory and monte-carlo calculations", Physica **44** (1969) 437.

[19] A. C. Holt, W. G. Hoover, S. G. Gray and D. R. Shortle, "Comparison of lattice-dynamics and cell-model approximations with monte-carlo thermodynamic properties", Physica **49** (1970) 61.

[20] H. Takeda, S. M. Miyama, and M. Sekiya, "Numerical simulation of viscous flow by smooth particle hydrodynamics", Progress of Theoretical Physics **92** (1994) 939.

Blank page

CHAPTER 4

IRREVERSIBILITY AND INSTABILITY

Blank page

4.1 Introduction

The basic physical equations governing the behavior of fluids and solids in motion are the well known laws of mechanics – conservation of mass, the Newtonian laws of motion, and the laws of thermodynamics. These equations are very simple and neat in appearance but complexities arise because these equations are nonlinear [1]. Even steady nonequilibrium systems behave in a very complex way. We begin our study of microscopic and macroscopic stability problems by reviewing the basic physical terms involved in this complexity.

We describe Lyapunov instability and fluctuations in microscopic steady nonequilibrium systems in Section 4.2. The scope of SPAM for dealing with hydrodynamic systems is also described in this Section. In a time reversible algorithm Lyapunov exponents should be reversible too. This is unlike expected behavior in a dissipative system [2]. Most algorithms are not time reversible. For microscopic molecular dynamic systems, Levesque and Verlet devised a bit reversible integer algorithm [3]. We applied their algorithm to the macroscopic SPAM algorithm and found a bit reversible SPAM algorithm for a non-dissipative system. For the special case of an isentropic ideal gas, we show that SPAM simulations produce continuum particle trajectories identical to those in molecular dynamics so that the continuum weight function $w(r)$ plays the role of an atomistic potential function $\phi(r)$ [4]. We describe time reversible continuum mechanics in Section 4.3. In this Section, we also discuss numerical errors due to Lyapunov instability.

Macroscopic instability is also present in some solutions of the hydrodynamic equations [5]. The solutions of the hydrodynamic equations can have an intrinsic instability in their reaction to the small perturbations to which any physical system is subject. In Section 4.4 we review the nature of different kinds of hydrodynamic instabilities – Rayleigh-Bénard, Couette, Rayleigh-Taylor, Kelvin-Helmholtz, Richtmyer-Meshkov.

4.2 Lyapunov instability and fluctuations.

"The present-day challenge for simulation and for statistical mechanics lies in understanding nonequilibrium systems, particularly those which exhibit macroscopic Lyapunov instabilities", Professor Hoover emphasizes [6]. Lyapunov instability is pervasive in both microscopic and macroscopic dynamics. Many-body systems, both at and away from equilibrium, are generally unstable, so that trajectory stability deserves discussion.

In reference [10], Lyapunov instability is defined to exist whenever nearby solutions separate from one another *exponentially* fast in time. But here we expand the definition of hydrodynamic instability to include *linear* growth of perturbations from impulsive forces in some hydrodynamic systems. However, the definition of Lyapunov instability is unchanged: nearby trajectories separate exponentially fast in time. The Lyapunov spectrum of exponents is a quantitative phase-space measure of instability. Exponents measure the growth and decay of chaotic fluctuations in the system, calculated from neighboring "satellite" trajectories in the vicinity of an unperturbed "reference" trajectory [7]. They are related to the occupied phase-space dimension of the system, Hausdorff dimension, measure, and Kolmogorov-entropy through a few mathematical theorems, a few plausible conjectures, and a wealth of numerical exploration [8].

Trajectory separation can be measured in either configuration space, momentum space, or the full phase space [9]. The exponential instability of a perturbation, varying as $\exp(\lambda t)$, where λ is the Lyapunov exponent, is important for two reasons: first it is typical, and limits the time for which an accurate numerical solution can be found; second it is the type of motion which requires just as much information in the initial conditions as can be extracted from the trajectories [10, 11].

From the geometrical point of view, these instability notions lead to phase-space strange attractors, an essential aspect of dissipative nonlinear dynamics. The phase space volume of any dissipative system contracts in the process of evolution and the motion is confined to a certain fractional-dimensional "multifractal" attractor in the long time limit $t \rightarrow \infty$. The phase space information dimension of the attractor D, is typically not an integer and is always lower than the dimension of the original embedding phase space [7,8].

By applying this notion to microscopic nonequilibrium molecular dynamics simulations, the irreversible time evolution that results from reversible mechanics can be understood in a simple geometric way, without the need of any approximations. This provides a valid explanation of the Second Law of Thermodynamics, extending Boltzmann's celebrated dilute-gas H theorem to more general systems [12].

The Lyapunov instability in macroscopic hydrodynamic systems, "turbulence", results from a complex fluctuating flow which generates macroscopic information more rapidly than it can be dissipated by viscosity, making the future of the flow unpredictable. Irreversible macroscopic flows are described by dissipative constitutive equations, which typically include plasticity, or Newtonian viscosity, as well as Fourier heat conduction.

Turbulence is intrinsically a macroscopic nonequilibrium fluctuation property, and is analogous to microscopic chaos [13]. Much the same at, and away from equilibrium, turbulent mixing, a macroscopic manifestation of the chaos lurking in most nonlinear problems, occurs at a high Reynolds number because the ratio of the time required for decay to the time required for shear is so large that the fluid is "turbulent". The *decay time* is defined as the time in which viscosity can dissipate the velocity gradients causing the shape to change (L^2/ν), where L is a typical system dimension; ν is the kinematic viscosity, defined by the ratio of shear viscosity η to density ρ. The *shear time* is defined by the time required for the comoving Lagrangian volume element of macroscopic flow to change its shape (L/u), where u is a typical flow speed. The details of turbulence also depend upon the boundary conditions which provide momentum and heat to the system from the surroundings.

The understanding of flows, including spontaneous thermal fluctuations, requires an explicit treatment of source terms (usually related to boundary conditions) to offset the continual damping provided by viscosity and heat conduction since the macroscopic hydrodynamic equations typically incorporate constitutive relations which proceed irreversibly towards a maximum entropy (equilibrium) state.

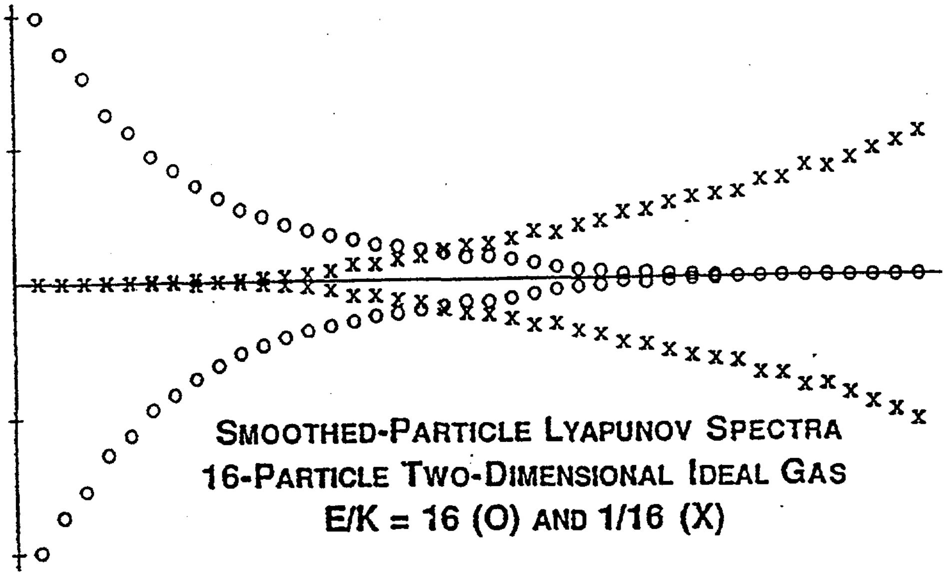

Figure 4.1 Lyapunov spectra for two-dimensional ideal gases made up of 16 smoothed particles, each with unit mass and described by Lucy's weighting function with a range of 1.5. The particles originally occupied a perfect triangular lattice, with a periodic area 4 x $(12)^{1/2}$. The initial ratios of inertial to kinetic energy are indicated. From reference [16].

The usual macroscopic hydrodynamic equations can lose the microscopic chaos inherent in the fluid they describe by ignoring fluctuations. Accordingly, some authors [14,15] emphasize the difficulty in establishing chaos, from numerical solutions, in systems of partial differential equations. When fluctuations are important, smooth particle simulation provides a natural way to include them [16].

In Smooth Particle Applied Mechanics, a truly stationary state, without fluctuations, is possible only if the underlying w-fluid freezes. For example, smooth particle applied mechanics contains velocity fluctuations, with two different estimates of the velocities at the nodal points, {v}, the velocities at which the points move, and {<v>}, the spatially-averaged velocities characterizing the neighborhoods of the moving points. The smooth particle continuum approach to hydrodynamics includes chaotic fluctuations which can be quantified by measuring the Lyapunov spectrum. Figure 4.1 [16] shows that macroscopic fluctuations, measured by Lyapunov spectra for macroscopic SPAM systems, look very much like those of microscopic molecular dynamics systems [17]. This result comes from Liouville's theorem - the equilibrium form of the phase-space continuity equation. The system is convective, conserving phase-space volume, because the sum of all the Lyapunov spectrum exponent pairs is zero.

There is an extremely interesting relationship between the Newtonian equations of motion for a dense fluid and the smooth particle equations for an ideal gas. For the isentropic ideal gas equation of state, $P \equiv \rho^2/2$, the smooth particle motion equations are isomorphic to the motion equations of molecular dynamics using weighting function $w(r) \equiv \phi(r)$ as the governing pair potential [4]. This isomorphism appears peculiar, because the molecular dynamics motion, although conservative and perpetual, must certainly exhibit the long-wavelength viscous dissipation and heat conduction associated with irreversibility in numerical simulation. At the same time, the Eulerian equations of fluid mechanics contain no explicit dissipation, and applied to an isentropic ideal gas, correspond to an infinite Reynold number, but with time-reversibility. SPAM also shows an intrinsic shear modulus with elastic properties similar to those found using molecular dynamics. The intrinsic shear modulus of SPAM, which comes from the isomorphism to molecular dynamics, was discussed in section 3.6 in Chapter III.

Before investigating the shear modulus and viscosity, we investigate the time reversibility of SPAM with the Euler equations, using a method analogous to molecular dynamics, invented by Levesque and Verlet and illustrated in their bit-reversible leapfrog algorithm [3]. We discuss the time-reversibility of SPAM in detail in the next section.

4.3 Time reversible continuum mechanics [4]

The "leapfrog algorithm" of atomistic molecular dynamic [3],

$$\{ r_+ - 2r_o + r_- \equiv dt^2(F/m)_o \}; \tag{1}$$

is patently time reversible. Any "trajectory", a selection of discrete time-ordered coordinates $\{r(ndt)\}$, going forward in time is mathematically equivalent to a time-reversed trajectory $\{r(-ndt)\}$ obeying the same motion equations. But ordinarily, computer roundoff errors lead to small errors in the last decimal place. Such errors can then grow in time, with Lyapunov instability, as $\exp(\lambda t)$, restricting the effective time-reversibility of trajectories to just a few "Lyapunov times"; that is, a few times $1/\lambda$. For a description of Lyapunov instability in many-body systems see reference [17].

Levesque and Verlet showed [3] that the combined irreversible effect, due to roundoff error plus Lyapunov instability, can be eliminated entirely by using an integer representation of coordinate space $\{r\}$. Here we explore that same idea from the standpoint of macroscopic continuum mechanics, employing a version of continuum mechanics, smooth particle applied mechanics, which closely resembles microscopic molecular dynamics, but which extends the state space to include densities $\{\rho\}$ and internal energies $\{e\}$ for each particle.

The leapfrog representation of the continuum particles' equations of motion can be combined with a time-symmetric energy equation to give the following explicit algorithm:

$$(r_+ - 2r_o + r_-)_i \equiv dt^2\Sigma\{[(m\sigma/\rho^2)_i + (m\sigma/\rho^2)_j]\cdot\nabla_i w_{ij}\}_o ; \quad (2)$$

$$(e_+ - e_-)_i \equiv dt\Sigma\{[(m\sigma/\rho^2)_i + (m\sigma/\rho^2)_j]_o : u_{ij}(\nabla_i w_{ij})_o\} ; \quad (3)$$

$$2dt\, u_{ij} \equiv (r_+ - r_-)_i - (r_+ - r_-)_j . \quad (4)$$

The initial values required are coordinates and energies at two successive times, $t = -dt$ and $t = 0$, for instance. Numerical tests indicate that this scheme is stable, with local errors which are third order in the time step dt and global errors which are second order. That the scheme is stable is by no means obvious *a priori.* For example, a similar difference scheme for the first-order differential equations of molecular dynamics, and taken from Milne's text [18],

$$r_+ - r_- \equiv 2dt\, u_o ; \quad u_+ - u_- \equiv 2dt(F/m)_o, \quad (5a,b)$$

though formally equivalent to the leapfrog scheme for a doubled time step of 2dt, turns out to be unstable for molecular dynamics [13].

After our successful trials in one dimension suggested the possibility of stability for this approach, we tested this scheme in two space dimensions with the hydrostatic nonlinear equation of state,

$$P \equiv -\sigma \equiv \rho^2 - 1 + e, \quad (6)$$

containing both tensile and compressive parts, as well as thermal expansion.

The numerical results, for 25 particles of unit mass, in a 2.5x2.5 periodic container with initial internal and kinetic energies of 25 and 25, conserved energy well with time steps of 0.01 and 0.02, showing the expected second-order global errors.

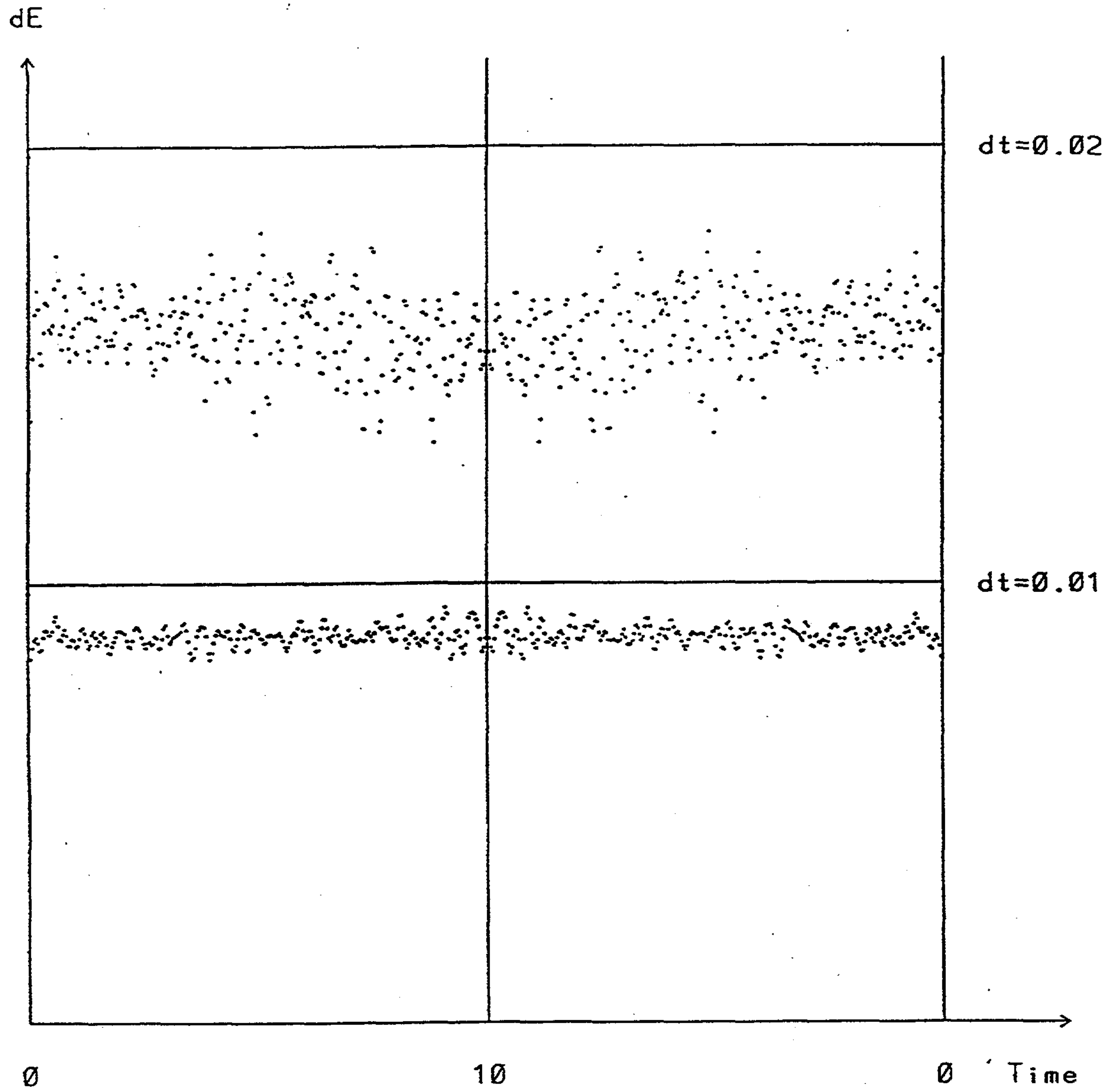

Figure 4.2 Time development of the 25-particle energy error (with a total energy fluctuating about 50.0) using generalized leapfrog timesteps of 0.01 (below) and 0.02 (above) to solve equations (16a), (17), and (21) in Chapter 2. A timestep 0.04 is unstable. At time 10 the velocities were reversed and the simulations returned exactly ("bit reversibly") to the initial condition shown in Figure 4.3.

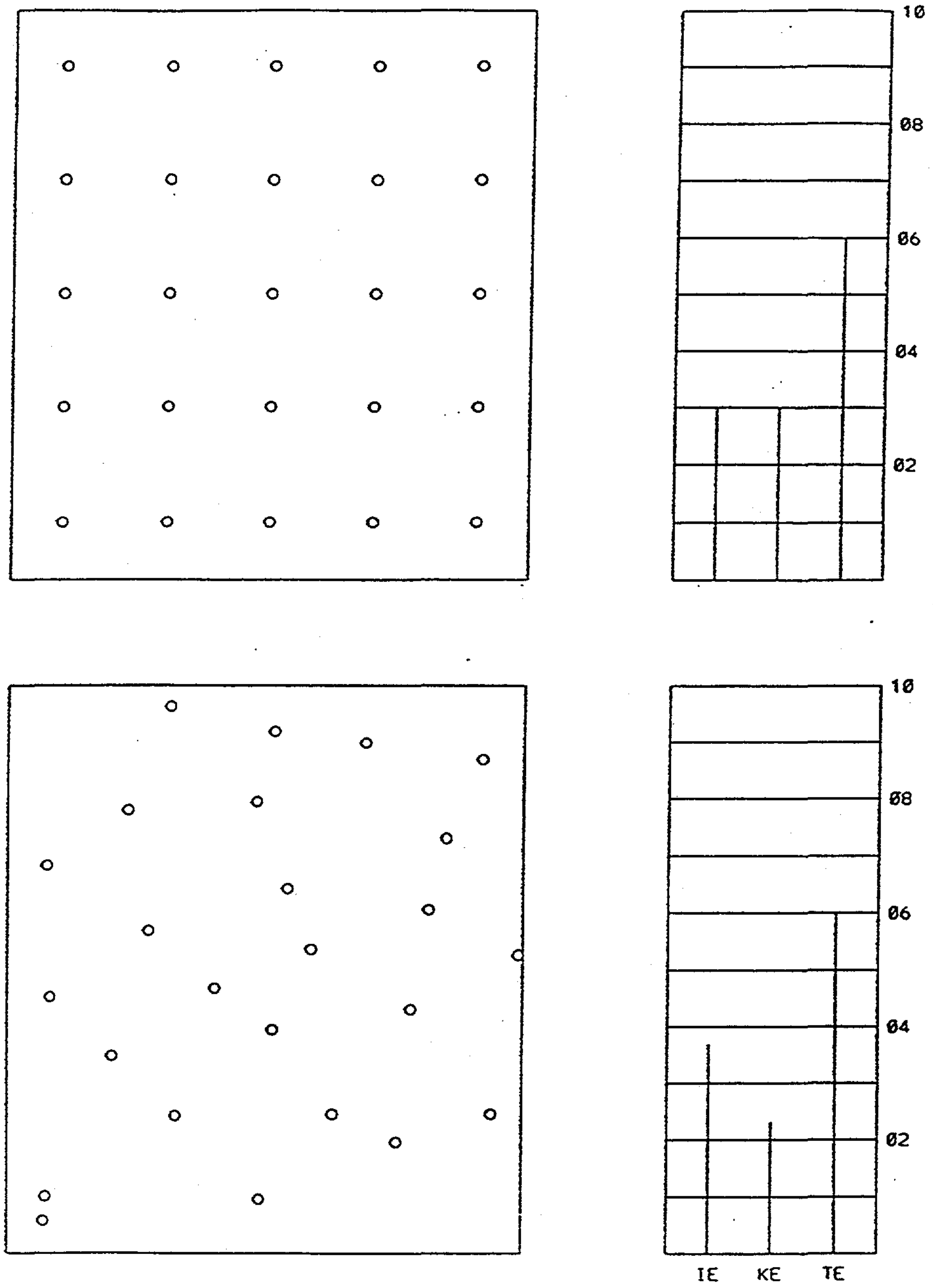

Figure 4.3 Initial and final configuration (time 1000 with timestep 0.01) for 25 periodic continuum particles with the equation of state $p = \rho^2 - 1 + e$. The time-averaged internal and kinetic energies are 33.94 and 16.05. The vertical bars indicate (from left to right) internal, kinetic, and total energy.

See the energy errors plotted in Figure 4.2. The overall density in this case is 4, around which the smoothed-particle sum fluctuates. The particles were initially arranged in a square lattice, with random velocities summing to zero. The ordered arrangement gives way to disordered fluid arrangements of the type shown in Figure 4.3.

Following Levesque and Verlet [3], we replaced the coordinates and energies by 32-bit integers, carrying out intermediate operations in floating point arithmetic and then truncating the results for the $\{r\}$ and $\{e\}$ to integers. Tests showed bit-perfect time reversibility (as would be expected from the time-symmetry of the difference equations) over computations of tens of thousand of time steps.

We conclude that the same reversibility properties which apply to molecular dynamics can be extended to the Euler equations of continuum mechanics by using the smooth particle approach (bit-reversible for an integer state space).

In the special case of an isentropic ideal gas, the smooth particle approach to the continuum simulation produces trajectories identical to those found in molecular dynamics, so that the continuum weight function $w(r)$ is equivalent to an atomistic potential function $\phi(r)$. When dissipation is present, we were unable to find a similar time-symmetric stable formulation in the *continuum* case. We were also unable to extend Levesque and Verlet's approach to the *atomistic* case with a *constrained kinetic energy* [13,19]:

$$\{dr/dt \equiv u;\ du/dt \equiv (F/m) - \xi u\};\ \xi \equiv (1/2K)\sum F\cdot u;\ K \equiv (m/2)\sum u^2;$$

$$dK/dt = 0. \qquad (7a,b,c,d)$$

We conjecture that a stable time-symmetric bit-reversible algorithm for these atomistic *isokinetic* equations *cannot* be found. From the physical standpoint, this might be expected, because such thermostatted equations can be used to drive steady nonequilibrium heat currents, producing multifractal strange attractor and repellor objects in the phase space [13,19]. These fractal structures are the antithesis of the conserved phase volume which characterizes equilibrium flows.

4.4 Hydrodynamic instabilities [5, 20, 21]

Solutions of the hydrodynamic equations can have an inherent instability in their reaction to the small perturbations to which any physical system is subject. The hydrodynamic stability problems originate in the differentiation of stable from unstable patterns of flow. In considering the stability of the hydrodynamic system with a given set of parameters defined by the system states, we determine the reaction of the system to small perturbations.

The important question is this: if the system is perturbed, will the perturbation gradually die down, or will it grow in amplitude in such a way that the system progressively departs from the initial state, especially exponentially fast, and never reverts back to it? In the former case, we say that the system is stable with respect to the perturbation; in the latter case, we say that it is unstable. Clearly, a system must be considered as unstable even if there is only one special mode of perturbation with respect to which it is unstable. In other words, stability means stability with respect to *all* possible infinitesimal perturbations. Most stability problems involve dissipative systems. In non-dissipative, conservative systems, the situation is generally different. Stable states, when perturbed, execute undamped oscillations with certain definite characteristic frequencies or grow linearly in time; in unstable states small initial perturbations grow exponentially with time.

There are several different types of instabilities intrinsic to hydrodynamics — Rayleigh–Bénard [22], Couette [23,25], Rayleigh–Taylor [24], Kelvin–Helmholtz [25], Richtmyer–Meshkov [26]. To simplify the study of these instability phenomena, we combine various system parameters into nondimensional combinations. Among all hydrodynamic instability problems, the best known of such numbers is the Reynolds number Re:

$$\mathrm{Re} \equiv Lu/\nu, \tag{8}$$

where L is a typical dimension of the system, u is a typical speed, and ν is the kinematic viscosity.

The origin of the instability is always the same–a potentially unstable arrangement of the fluid results from a variety of externally imposed conditions. We can also have an unstable arrangement of flow resulting from a prevailing adverse gradient of angular momentum in Couette flow: in a steady circular flow of a liquid between two rotating coaxial cylinders. This instability can be interpreted in terms of Taylor number (Ta). A discussion of this problem can be found in references [23, 25]. For Couette flow, viscous flow between two rotating coaxial cylinders, the Taylor number Ta, including cylinder radii and angular velocities, is used:

$$\mathrm{Ta} \equiv (4\Omega_1{}^2R_1{}^4/\nu^2)[(1-\mu)(\eta^2-\mu)/(\eta-\eta^3)^2]; \tag{9}$$

$$\eta \equiv R_1/R_2\,;\ \ \mu \equiv \Omega_2/\Omega_1, \tag{10a,b}$$

where R_1 and R_2 are the radii of two cylinders, and Ω_1 and Ω_2 are the angular velocities of their rotations.

Similarly, for the thermal stability of a horizontal layer of fluid, heated from below, the Rayleigh number and Prandtl number are used:

$$\mathrm{Ra} \equiv g\alpha\beta L^4/(\kappa\upsilon)\,;\ \ \mathrm{Pr} \equiv \upsilon/\kappa, \tag{11a,b}$$

where g is the acceleration due to gravity, L is the depth of the layer, β is the imposed temperature gradient, α and κ are the coefficient of thermal expansion and thermal diffusivity, the ratio of heat conductivity to specific heat capacity times density.

Rapid low-cost simulations are replacing the complex theoretical approaches and structures of the pre-computer era. It is nowadays easy to study instabilities by computer simulation. We study two types of instabilities, Rayleigh-Bénard and Richtmyer-Meshkov, using SPAM. Before we discuss our results, we describe the fundamental features of these instabilities.

The Rayleigh-Bénard problem in horizontal layers of fluid heated from below is now nearly 100 years old, demonstrated by Bénard in 1900, but still the subject of intensive investigations and still regularly yielding surprising results relevant to the general theory of hydrodynamic stability. A horizontal layer of fluid with an adverse temperature gradient is maintained by heating the underside. The temperature gradient maintained is adverse since, on account of thermal expansion, the fluid at the bottom will be lighter than the fluid at the top. Gravitational force is applied to the system in adverse direction of temperature, yielding a top-heavy, potentially unstable, arrangement of the system. Because of this latter instability there is a tendency for the fluid to redistribute itself. This natural tendency is inhibited by viscosity. We expect that the adverse temperature gradient must exceed a certain value before instability can occur. The theoretical foundation of this phenomenon involves the non-dimensional Rayleigh number (Ra), named for Lord Rayleigh. We report simulation results using SPAM in Chapter V.

The onset of instability of the fluid can occur in heterogeneous fluids—two contiguous fluids, possibly with different densities accelerated toward each other. There are at least three different instabilities of this type. Rayleigh-Taylor instability occurs when a light fluid supports a heavy one in a gravitational field. The upper heavy fluid in the nonlinear stage of the Rayleigh-Taylor instability forms falling spikes while the light one forms rising bubbles. For the small interface perturbations, the instability grows exponentially.

In the same situation but with the layers in relative horizontal motion, the instability of the plane interface is called Kelvin-Helmholtz instability.

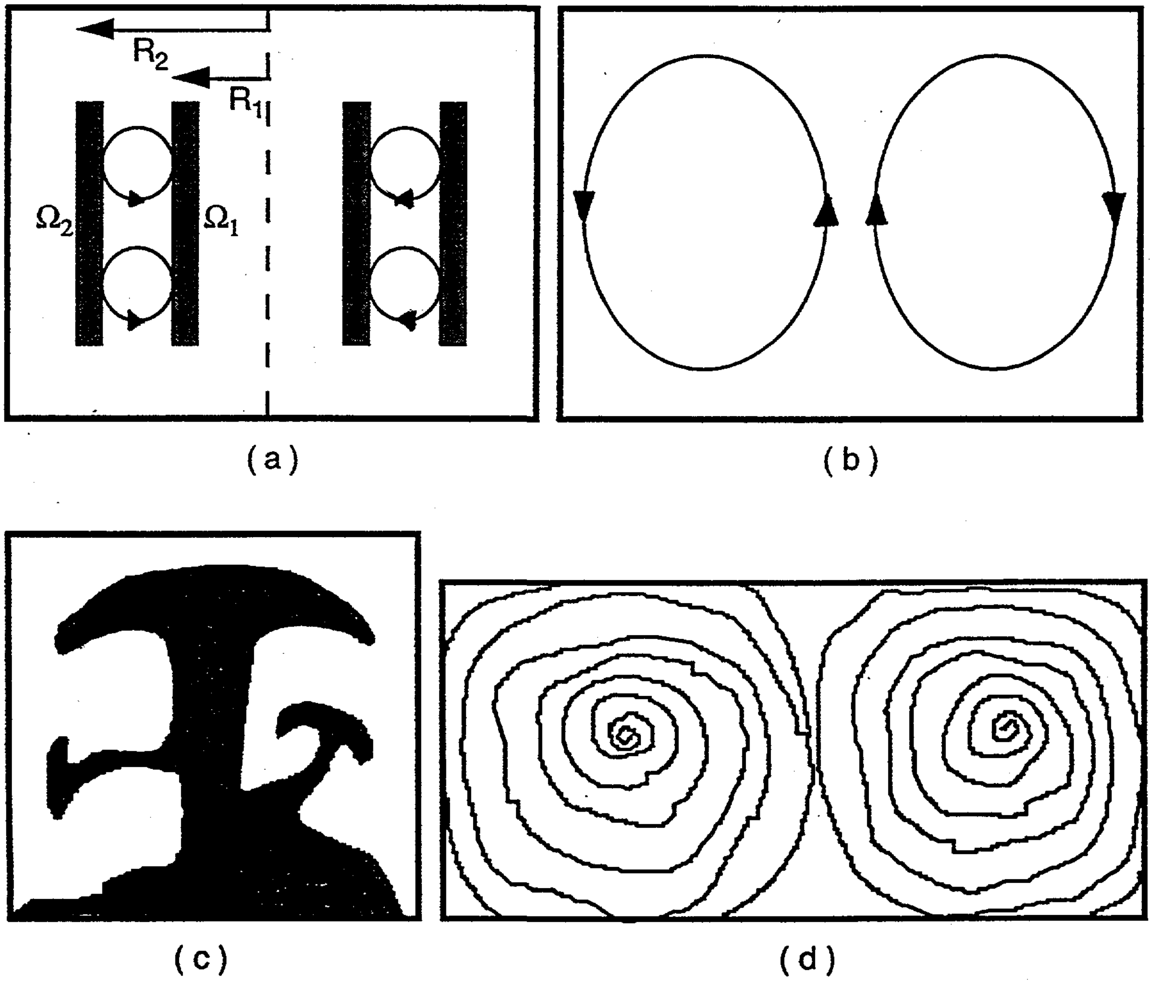

Figure 4.4 Schematic Diagram of fluid dynamic instabilities: (a) instability arising from rotating Couette flow (arrangement of Taylor cells), (b) Rayleigh-Bénard instability (Rayleigh-Bénard cells), (c) Richtmyer-Meshkov instability in shock impulsive force field, or Rayleigh-Taylor instability in gravitational field (bubbles and spikes), (d) Kelvin-Helmholtz instability (shear instability in stratified fluid).

Instead of gravitation, as in Rayleigh-Taylor instability, a shock wave can accelerate one fluid into the other. This type of instability is called Richtmyer-Meshkov instability, predicted by Richtmyer and confirmed experimentally by Meshkov. When a shock wave collides with the interface between two different materials, the interface perturbations grow into nonlinear structures having the spike-and-bubble form of Rayleigh-Taylor instability. There is no theory or computation providing a comprehensive understanding of this instability. However, for small perturbations the instability grows linearly. Lawrence Livermore National Laboratory's A Division has much interest in studying these hydrodynamic instabilities. Dr. Mikaelian [27] (A Division) has studied theoretically these instability problems for more than 10 years. We report our SPAM studies of this instability in Chapter VII. Figure 4.4 shows the four different kinds of instabilities—Rayleigh-Bénard, Couette, Kelvin-Helmholtz, and Richtmyer-Meshkov, which is qualitatively the same as Rayleigh-Taylor instability.

4.5 Summary

Usually macroscopic hydrodynamic calculations reduce the fluctuations intrinsic to the microscopic molecular level. But SPAM incorporates fluctuations characterized by two different velocities: velocity calculated from direct time integration of the motion equation and the velocity calculated from the spatial averages using weighting function. These fluctuations occur whether the flow is turbulent, or not. However, for conservative macroscopic hydrodynamic systems, Lyapunov spectra calculated from SPAM algorithm resemble those from Molecular Dynamics: sums of pairs of exponents vanish so that phase space volume is conserved with time - the result from Liouville's theorem.

For an isentropic ideal-gas system, the Smooth Particle equation of motion is identical to that of Molecular Dynamics. It generates the same trajectories as those of Molecular Dynamics so that the Smooth Particle method has intrinsic viscosity, conductivity, and elastic constants. These constants are intrinsic to Molecular Dynamics.

Extending the "Bit reversible integer algorithm" developed by Levesque and Verlet for molecular dynamics, we showed that smooth particle applied mechanics is also time reversible for non-dissipative macroscopic hydrodynamic systems. For the Bit-reversible leapfrog algorithm, SPAM with B spline weighting function of the smoothing length 2.5 is stable with time steps up to 0.02. Our system goes forward 100 000 cycles to time 1000, with time step 0.01, and then reverses back to the exact initial configuration at time 2000.

For hydrodynamic systems, instabilities are ubiquitous due to nonlinearities. We described different types of instabilities and non-dimensional variables used in simplifying analyses of instability problems: Reynolds number, Taylor number, Rayleigh number, and Prandtl number. Schematic pictures of fully developed instabilities were presented.

References

[1] J. Gleick, **CHAOS, making a new science** (Viking, New York, 1988).

[2] W. G. Hoover, C. G. Tull (now C. G. Hoover), and H. A. Posch, "Negative Lyapunov exponents for dissipative systems", Physics Letters A **131** (1988) 211.

[3] D. Levesque and L. Verlet, "Molecular dynamics and time reversibility", Journal of Statistical Physics, **72** (1993) 519.

[4] O. Kum and W. G. Hoover, "Time-reversible continuum mechanics", Journal of Statistical Physics, **76** (1994) 1075.

[5] S. Chandrasekhar, **Hydrodynamic and hydromagnetic stability** (Oxford, London, 1961).

[6] W. G. Hoover, In Lecture of EAL 228C "Nonequilibrium statistical mechanics", **Winter quarter** (1994).

[7] Hao Bai-Lin, **Chaos** (World Scientific, Singapore, 1984).

[8] H. G. Schuster, **Deterministic chaos, An introduction**, 2nd ed., (VCH, Weinheim, 1989).

[9] S. D. Stoddard and J. Ford, "Numerical experiments on the stochastic behavior of a Lennard-Jones gas system", Physical Review A **8** (1973) 1504.

[10] E. T. Jaynes, "Information theory and statistical mechanics", Physical Review, **106** (1957) 620; E. T. Jaynes, "Information theory and statistical mechanics. II", Physical Review, **108** (1957) 171.

[11] J. Ford, "How random is a coin toss", Physics Today **36** (1983) 40.

[12] W. G. Hoover, **Molecular dynamics**, Lecture Notes in Physics **258** (Springer-Verlag, Berlin, 1986).

[13] W. G. Hoover, **Computational statistical mechanics** (Elsevier, Amsterdam, 1991).

[14] P. Cvitanovic, **Universality in chaos** (Adam Hilger, Bristol, 1984).

[15] I. Goldhirsch, R. B. Pelz, and S. A. Orszag, "Numerical simulation of thermal convection in two-dimensional finite box", Journal of Fluid Mechanics, **199** (1989) 1.

[16] W. G. Hoover, T. G. Pierce, C. G. Hoover, J. O. Shugart, C. M. Stein, and A. L. Edwards, "Molecular dynamics, smooth-particle applied mechanics and irreversibility, Computers and Mathematics with Applications **28** (1994) 155.

[17] H. A. Posch and W. G. Hoover, "Equilibrium and nonequilibrium Lyapunov spectra for dense fluids and solids", Physical Review A **38** (1988) 473.

[18] W. G. Milne, **Numerical calculus** (Princeton University Press, Princeton, New Jersey, 1949).

[19] D. J. Evans and G. P. Morriss, **Nonequilibrium liquids** (Academic Pres, New York, 1990).

[20] D. J. Tritton, **Physical fluid dynamics** (Oxford, London, 1988).

[21] G. K. Batchelor, **An introduction to fluid dynamics** (Cambridge University Press, Cambridge, 1967).

[22] M. Mareshal, M. Malek Mansour, A. Puhl, and E. Kestemont, "Molecular dynamics versus hydrodynamics in a two-dimensional Rayleigh-Bénard system", Physical Review Letters, **28** (1988) 2550; E. Knobloch and J. Guckenheimer, "Convective transitions induced by a varying aspect ratio", Physical Review A **27** (1983) 408.

[23] R. E. Meyer, editor, **Transition and turbulence** (Academic Press, New York, 1981).

[24] C. L. Gardner, J. Glimm, O. McBryan, R. Menikoff, D. H. Sharp, and Q. Zhang, "The dynamics of bubble growth for Rayleigh-Taylor unstable interfaces", Physics of Fluids **31** (1988) 447.

[25] J. S. Walker, G. Talmage, S. H. Brown, and N. A. Sondergard, "Kelvin-Helmholtz instability of Couette flow between vertical walls with a free surface", Physics of Fluids A **5** (1993) 1466.

[26] K. A. Meyer and P. J. Blewett, "Numerical investigation of the stability of a shock-accelerated interface between two fluids", Physics of Fluids, **15** (1972) 753.

[27] K. O. Mikaelian, "Oblique shocks and the combined Rayleigh-Taylor, Kelvin-Helmholtz, and Richtmyer-Meshkov instabilities", Physics of Fluids **6** (1994) 1943.

CHAPTER 5

RAYLEIGH - BÉNARD INSTABILITY

Blank page

5.1 Introduction

We had a coarse grained introduction to this topic in section 4.3, "hydrodynamic instabilities", but it was only a glimpse of a larger problem. The Rayleigh-Bénard problem originated in the study of regular convection cell structures seen in fluid layers heated from below. The overall configuration with which we are concerned was shown in Figure 4.4(a): a layer of fluid is bounded by two horizontal rigid planes separated by a vertical [y] distance L and at different constant uniform temperatures T_1 and T_2 – the lower plate is hotter than upper one ($T_2 > T_1$). In everyday experience, this configuration is common – for example, in boiling water, hot fluid tends to rise and cold fluid tends to fall. The principle is very simple but its consequences are among the most complex in fluid dynamics. For nearly incompressible fluids, Lorenz' classic set of three coupled nonlinear equations describes the mechanical instability.

The history of related hydrodynamic investigations spans a century. The references listed in the work by Goldhirsch, Pelz and Orszag [1] provide access to the early work. As we already mentioned, some nondimensional parameters (the Rayleigh number, the Prandtl number, the aspect ratio, and the Nusselt number) play important roles in this problem.

As a geometric parameter, the aspect ratio of the system, Γ is defined as the ratio of the horizontal, x direction to the vertical, y direction, L_x/L_y. Horizontal dimensions are sometimes assumed infinite (modelled with periodic boundary condition) but the classical Rayleigh-Bénard problem has a finite boundary on which the fluid is at rest. The Rayleigh number and Prandtl number were defined in section 4.3. One of the most convenient nondimensional numbers in this instability problem is the Nusselt number, Nu [$\equiv QL_y/(k\Delta T)$], where Q is heat flux, $\Delta T = T_2 - T_1$, k is thermal conductivity, and L_y is the system height. The Nusselt number is the ratio of the actual heat transfer to the heat transfer that would occur by conduction alone were the fluid at rest. The onset of Rayleigh-Bénard instability is marked by Nu increasing above unity [1-5].

As an analytic method for solving this problem the Boussinesq approximation together with variational approximation methods have been used with many approximations [6, 7]. These methods explain the basic physics behind this problem. We review these in Section 5.2. Because cases in which the fluid equations can be solved analytically are limited, numerical methods play an important role in this problem. Numerical methods can be applied to the full set of hydrodynamic equations.

In the analysis of this problem with SPAM, we have several different models – with different configurations and boundary conditions, with different forms of weighting functions, and with different constitutive equations. We review the classic analytic methods in the next section. From this review, we see the essential physical concepts of this problem. We describe different parameters used in our numerical models in Section 5.3. In Section 5.4 we briefly describe the Navier-Stokes continuum model for comparison. We report our results and conclusion in Section 5.5. Section 5.6 includes a summary.

5.2 Analytic methods [6-8]

Imagine the fluid in between two different temperature plates. Heat is conducted into the fluid from a hot wall, transported through the layer and conducted out at the cold wall. There is no overall mass transport in this process. The time-averaged upward and downward mass currents balance. If the space were filled with a solid instead of a fluid, the transport through the layer would be by conduction so that the temperature would fall approximately linearly from the hot wall to the cold. In the case of fluid in motion, the temperature distribution is more complicated but the fluid close to the hot wall is at higher temperature than the fluid close to the cold wall. Density variation accompanies this temperature variation: the hot fluid expands, and so becomes less dense than the cold fluid. The cause of motion is the differing gravitational force per unit volume acting on these density differences: the fluid would remain at rest if the applied temperatures were equal ($T_1 = T_2$), if the density did not vary with temperature, or if there were no gravitational force field applied. Consequently, an analysis includes all three concepts.

The Boussinesq approximation method, which is the simplest analytic method, deserves review here. In this approximation, variations of all fluid properties other than the density and pressure are ignored completely. Variations of the density are ignored except in so far as they give rise to a gravitational force. From this approximation, the fluid is incompressible:

$$\nabla \cdot \mathbf{u} = 0. \tag{1}$$

Similarly the term, $\rho d\mathbf{u}/dt$, in the motion equation is replaced by $\rho_o d\mathbf{u}/dt$ with constant ρ_o imposed in the initial condition. Only the gravitational force in the vertical direction is not approximated,

$$F = \rho g = (\rho_o + \Delta\rho)g = \nabla \cdot (\rho_o g y) + \Delta\rho g, \tag{2}$$

where we assume that a specific potential energy due to gravity is gy in the vertical direction. The pressure due to density change is linearized:

$$P = p_o + \rho_o g y, \tag{3}$$

where p_o is hydrodynamic pressure and $\rho_o gy$ is hydrostatic pressure due to mass density ρ_o. Then the Navier-Stokes motion equation becomes,

$$\rho_o d\mathbf{u}/dt = -\nabla P + \eta \nabla^2 \mathbf{u} + \Delta\rho g \qquad (4)$$

If $\Delta\rho = 0$, this is the same as the Navier-Stokes equation without gravity except that P has been replaced by p_o. Because the Rayleigh-Bénard problem has no pressure boundary conditions this change makes no difference. Additionally one can linearize the dependence of ρ on T, $\Delta\rho = -\alpha\rho_o\Delta T$, where $\Delta T = T - T_{initial}$ and α is the coefficient of the thermal expansion. Then the Boussinesq equation of motion is,

$$d\mathbf{u}/dt = -(1/\rho_o)\nabla P + \nu\nabla^2\mathbf{u} - g\alpha\Delta T, \qquad (5)$$

where $\Delta T = T - T_{initial}$ and ν is kinematic viscosity, η/ρ_o.

In addition to the dynamical equation of motion, we need an energy conservation equation. If the heat conductivity and specific heat constant are constants in space and time, the energy conservation equation has the same form as does the Lagrangian heat transfer equation,

$$dT/dt = \kappa\nabla^2 T, \qquad (6)$$

where κ [$\equiv k/(\rho_o C_v)$] is the thermal diffusivity. Note that the work term is ignored in this approximation.

Let us consider the physical meaning of each term in these equations. The term, $-g\alpha\Delta T$, is known as the "buoyancy force" because this term represents the tendency for light fluid to rise. The term $\nu\nabla^2\mathbf{u}$ is the familiar "damping force" due to viscosity. The "inertia force" term, $\mathbf{u}\cdot\nabla\mathbf{u}$, is concealed in the Lagrangian comoving derivative of motion equation, $d\mathbf{u}/dt$. The right hand side term in heat transfer equation, $\kappa\nabla^2 T$, is the "conduction term". The "convection term", $\mathbf{u}\cdot\nabla T$, is also concealed in the comoving time derivative of temperature T. The boundary values are closely tied to the heat transfer equation (6) because the given boundary conditions provide temperature differences between the two vertical plates.

Since the dynamic roll mechanism is damped by viscosity the rolls are dormant for small temperature differences. Sufficient temperature difference can keep the rolls moving through the buoyant driving force of thermal expansion. The critical condition is that the two forces balance for large temperature differences, $\Delta T = T_2 - T_1$:

$$g\alpha\Delta T = \nu\nabla^2\mathbf{u} \quad \Rightarrow \quad u = (g\alpha\Delta TL^2)/\nu. \tag{7}$$

The Rayleigh number is just the ratio of the two competing heat fluxes, heat transfer by convection divided by heat transfer by conduction, when the roll velocity is estimated from force balance:

$$(\mathbf{u}\cdot\nabla T)/(\kappa\nabla^2 T) \sim (uL)/\kappa = (g\alpha\Delta TL^3)/(\kappa\nu) \equiv \mathrm{Ra}. \tag{8}$$

The Rayleigh number, Ra, represents the ratio of the two competing heat fluxes. The critical Rayleigh number is, however, not unity, but of order $(2\pi)^4 \sim 1000$. Provided that the Rayleigh number is sufficiently small the problem is a simple one with a linear temperature profile and with heat being transmitted from bottom to top by conduction. When the temperature difference becomes large enough a more efficient mode of energy transport is the formation of convective, and finally turbulent rolls, "Rayleigh-Bénard rolls."

The Prandtl number ($\mathrm{Pr} \equiv \nu/\kappa$) is related to the ratio of the inertia force due to the convective term in the motion equation to viscous dissipative forces;

$$(\mathbf{u}\cdot\nabla\mathbf{u})/(\nu\nabla^2\mathbf{u}) \sim (u^2/L)/[(\nu u)/L^2] = (uL)/\nu \equiv \mathrm{Ra}/\mathrm{Pr}. \tag{9}$$

Turbulent flows are rotational. Buoyancy forces can directly generate local vorticity. To see this, apply the curl ($\nabla\times$) operation to the Boussinesq motion equation (5),

$$d\omega/dt = \omega\cdot\nabla u + \nu\nabla^2\omega + \alpha g\times\nabla(\Delta T), \qquad (10)$$

where ω ($\equiv \nabla\times\mathbf{u}$) is the vorticity vector. The horizontal component of the temperature difference gradient, [$\nabla(\Delta T)$], contributes to generate vorticity perpendicular to the temperature difference gradient and gravity force. This is obvious: horizontally separated hotter fluid and colder fluid move in different directions to each other, the torque produces rotation about the third axis. The vertical component of the temperature difference gradient cannot contribute to generate the turbulence. See Figure 5.1 for the detailed geometry.

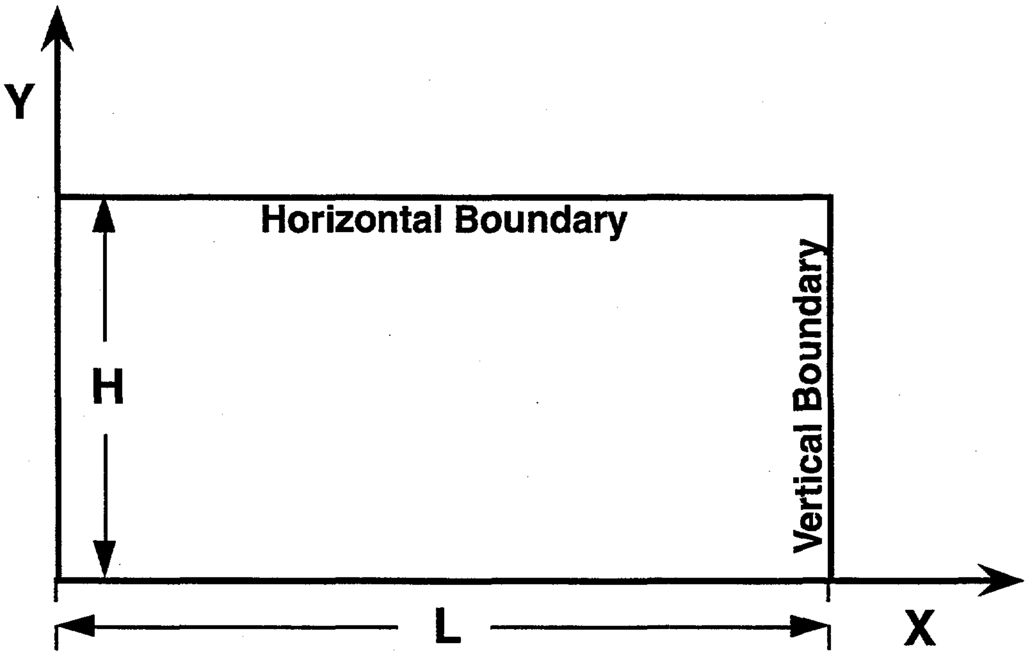

Figure 5.1 Coordinate system in two dimensional problem. The aspect ratio Γ is defined by L/H.

Another approximation, independent of this method, is the perturbation approach, which leads to a normal mode analysis. For details of this method, see reference [6]. In either approach, Boussinesq or perturbation, the solutions are subject to boundary conditions. Two different kinds of boundary conditions are typical of analytic methods: rigid surfaces on which no slip occurs and free surfaces on which no tangential stress acts. The condition that no slip occurs on a surface implies that not only the vertical component of velocity, but also the horizontal component of the velocity vanishes in a two-dimensional problem:

$$u_x = u_y = 0. \tag{11}$$

The condition on a free surface is likewise;

$$p_{xy} = 0 \text{ and } p_{yy} = 0. \tag{12}$$

Because the isotropic term $-p\delta_{ij}$ has no transverse component, the zero tangential stress condition implies, using the condition that u_y vanishes for all x on the boundary surface,

$$\partial u_y/\partial x = \partial u_x/\partial y = 0, \tag{13}$$

on the free surface. Therefore, boundary conditions for the Rayleigh-Bénard problem can be given in either of two ways: vanishing velocities or stress tensor components in the momentum conservation equation; fixed temperatures on the boundaries in the energy conservation equation. With these boundary conditions the critical Rayleigh number can be calculated analytically.

Another method to calculate the critical Rayleigh number comes from Schmidt and Milverton's experimental method. They determine the Nusselt number, which is also a non-dimensional parameter, by measuring heat flux quantities in convection. This number can also be used to calculate the critical Rayleigh number in computer simulation. To do this we calculate the Nusselt number as a function of Rayleigh number. Above the critical Rayleigh number the Nusselt number exceeds unity. Below the critical Rayleigh number it fluctuates around unity. Lastly the temperature distribution has a bifurcation at the critical Rayleigh number: the central temperature becomes different from the lateral edge temperatures. This temperature bifurcation phenomenon has also been used for calculating the critical Rayleigh number [13]. In SPAM simulations to calculate a critical number we can use either the Nusselt number or temperature bifurcation. We describe our simulation models in the next Section.

5.3 Simulation models [1, 9, 10]

Analytical results gives us the basic physical concepts regarding nondimensional parameters and approximate critical values for some simple systems. However, the cases in which the fluid equations of motion can be solved analytically are very limited. Numerical simulation plays an important role in the analysis of complicated fluid systems. Numerical experiments resemble laboratory experiments but can deal with problems out of the range of laboratory experiments [11]. Numerical experiments including microscopic systems, must also deal with simplified models, not real systems [12-19]. We use our SPAM algorithm to analyze the Rayleigh-Bénard problem. Since we already described the detailed numerical method in Chapter III, we describe only the parameters used in the models here.

Initially all system particles are placed on square lattice positions in two space dimensions. They have no initial velocities at all. Two different temperatures are applied to the two horizontal boundaries for an uniform adverse temperature gradient. The problem requires also a gravitational field g. To maintain thermal contact at the upper

[cold] boundary, g cannot be too large. For static equilibrium, and at constant density, gravity satisfies the force balance equation,

$$(\partial P/\partial T)_\rho \, dT - \rho g dy = 0. \tag{14}$$

For the ideal gas equation, gravity g is the ratio of temperature difference to the vertical boundary length. For the dense fluid equation of state, g is five times greater than that of ideal gas equation of state because the pressure is approximately five times greater than that of ideal gas equation of state. We also chose it in such a way that the maximum-to-minimum density ratio was not too large, always less than two.

We simulate two different models with rigid boundary conditions: four reflective boundaries using image particles, and two horizontal reflective boundaries with two periodic lateral boundaries. With image particles, temperature and velocity are fixed on the two horizontal boundaries as explained in Chapter III. We also tested fixed boundary particles. For still a different treatment of boundaries, using a continuous distribution of external particles, see Reference 23.

We use three different equations of state. The simplest of the three state equations is the ideal gas law, appropriate to a dilute gas:

$$P = \rho e; \ \beta e = e/k_B T = 1, \tag{15}$$

where k_B is Boltzmann's constant per unit mass. We have also used van der Waals' equation, which augments the ideal-gas equation of state to include both the effects of attractive forces (through the parameter a) and excluded volume effects (through the parameter b). In the single phase region of the phase diagram:

$$\beta P = [\rho/(1 - \rho b)] - \beta a \rho^2; \ \beta e = 1.0 - \beta \rho a; \ a = \varepsilon \sigma^2/2m; \ b = \sigma^2/2m. \tag{16}$$

We choose these values for the two material properties, a and b, in order that unit reduced number density, $n\sigma^2 = N\sigma^2/V = \rho\sigma^2/m = 1$, somewhat exceed the critical reduced number density (2/3) and that our reduced temperature range $0.5 < mk_BT/\varepsilon < 1.5$ lies well above the critical reduced temperature (8/27).

In addition to the ideal-gas and van der Waals models, we have also used a more-complex equation of state (macroscopic dense fluid equation of state) from molecular dynamics. The macroscopic dense fluid equation of state corresponds to a simple inter-atomic pair potential with three vanishing derivatives at the cutoff distance, $r = \sigma$ [15]:

$$\phi(r) = 100\varepsilon[1 - (r/\sigma)^2]^4. \tag{17}$$

More details of this potential are discussed in the reference [15]. For numerical purposes, we rewrite the forms of equation of state in terms of the density, ρ temperature, (kT/ε) pressure, $(PV/N\varepsilon)$ and energy, $(E/N\varepsilon)$. N is the number of particles with unit mass in molecular dynamic systems and ε is the strength of the potential. At unit (number) density and reduced temperature, ρ and (kT/ε), and the reduced pressure and energy, $(PV/N\varepsilon)$ and $(E/N\varepsilon)$, are respectively 1.00, 1.00, 5.04 and 1.443. For small deviations from this standard state, the following expansions apply [15]:

$$PV/N\varepsilon = 5 + 8\delta\rho + 2.5\delta\varepsilon + 9(\delta\rho)^2 + 2\delta\rho\delta\varepsilon; \tag{18}$$

$$mk_BT/\varepsilon = 1 - \delta\rho + 0.7\delta\varepsilon - 0.8(\delta\rho)^2 - 0.5\delta\rho\delta\varepsilon; \tag{19}$$

$$me/\varepsilon \equiv E/N\varepsilon = 1.443 + 1.5\delta\rho + 1.5\delta\tau + 2.4(\delta\rho)^2 + 1.2\delta\rho\delta\tau; \tag{20}$$

$$\delta\rho \equiv (N\sigma^2/V) - 1.0;\ \ \delta\varepsilon \equiv (E/N\varepsilon) - 1.443;\ \ \delta\tau \equiv (kT/\varepsilon) - 1.000. \tag{21}$$

It should be noted that this quadratic dense-fluid equation of state is not quite "thermodynamically consistent". For instance, the Maxwell relation based on differentiating Helmholtz' free energy A with respect to temperature and volume:

$$\partial^2(\beta A)/\partial\beta\partial V = (\partial E/\partial V)_T = \partial^2(\beta A)/\partial V\partial\beta = -\partial[(\beta P)/\partial\beta]_v;\ \beta = 1/mk_BT, \qquad (22)$$

is not exactly satisfied. This means that thermodynamic cycles can be constructed in such a way as to violate conservation of energy. To illustrate, consider just linear variations around the reference state. $(\partial E/\partial V)$, evaluated from the energy equation, is $1.5\varepsilon/\sigma^2$ while $\partial(\beta P)/\partial\beta = P + \partial P/\partial \ln\beta$, evaluated by combining the mechanical equation of state and the energy equation, is $1.25\varepsilon/\sigma^2$. This lack of consistency causes no apparent trouble in smooth particle simulations. On the other hand, we believe that it is the underlying cause of a slow divergence, at very long times, of some of our attempts to find corresponding Navier-Stokes "solutions".

Our dense fluid equation of state was especially useful in revealing a fundamental shortcoming of the smooth particle method in treating dense fluids. Our early attempts to compare Navier-Stokes and smooth particle solutions for the molecular dynamics based equation of state led repeatedly to "frozen" states with the smooth particles crystallizing into static hexagonal-symmetry structures with either one (Lucy) or two (Monaghan) particles per site. See Figure 5.2 for an example. In the calculation of Figure 5.2, a simpler **linear** (in δV and $\delta\beta$) version of dense fluid equation of state is used. The **linear** dense fluid equation of state has the same reference states as those of equations (18), (19), and (20) and satisfies exactly the Maxwell relation just described but without the **second** order terms. With exactly the same imposed boundary conditions, the Navier-Stokes equations with this **linear** version equation of state easily generate reproducible convecting flows.

In Figure 5.2 it is obvious that the density is nearly constant ($\rho \approx 1$) when the system is crystallized. The temperature gradient in the y direction (height) is likewise constant. Heat only flows through the conduction. The average temperature, T_{AV}, is $(T_H + T_L)/2$. The energy and pressure, e(ρ, T) and P(ρ,e), are both given by the equilibrium equation of state so that the pressure gradient balances the gravitational acceleration. This constant density, constant gradient crystallized system keeps its stationary structure forever.

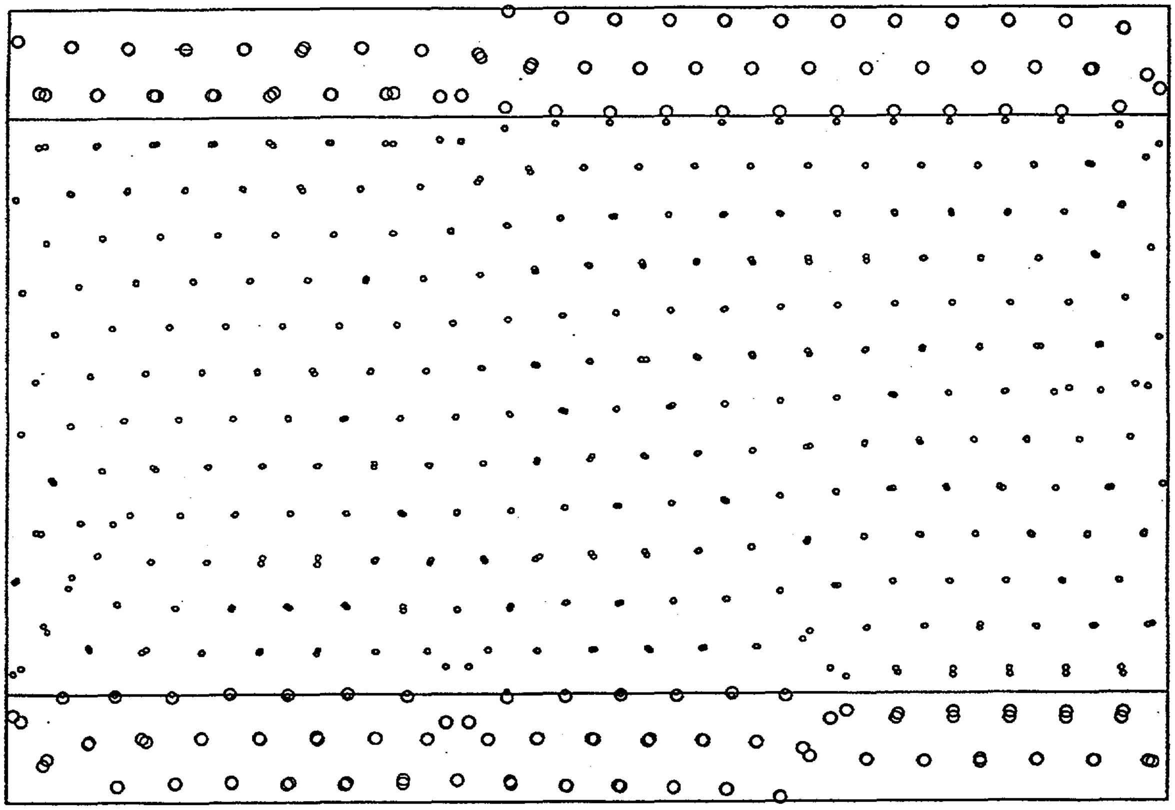

Figure 5.2. "Freezing" of the smooth particle fluid (Ra ≈ 2000). The **linear** dense-fluid equation of state is used. But the Navier-Stokes equations with the same equation of state show a convective solution with two rolls at this Rayleigh number. The high pressure, using Monaghan's weight function with a range h = 3σ, leads to an unphysical freezing of the smooth particles. Similar results are obtained using Lucy's weighting function. For the freezing system, density is constant and temperature and pressure gradients are constant. This constant density, constant gradient crystallized system keeps its stationary structure forever.

This unphysical high-pressure freezing can be traced to the form of the smooth particle equation of motion. At sufficiently low pressures a typical smooth particle kinetic energy exceeds the maximum value of the effective potential energy from which the smooth particle accelerations are determined:

$$mv^2 > g(0) = 2P(V/N)^2(\sigma/h)^2w(0). \tag{23}$$

At sufficiently high pressure, on the other hand, P(V/N) approximates mc^2, where c is the sound speed, so that ordinary hydrodynamic flows cannot overcome the potential barrier to smooth particle motion.

A more precise criterion for the applicability of the smooth particle technique for fluids can be based on an analog of Lindemann's melting criterion. In two or three space dimensions, melting occurs when the fluctuation in the nearest-neighbor separation is of order 10%. In order for the corresponding potential energy to be available from the flow, the pressure cannot be too large:

$$mv^2 > 2Pn^{-2}[w(0.9\sigma) - w(\sigma)]. \tag{24}$$

For our Lucy weight function the combination in square brackets is about 0.01n. In the molecular dynamics case $2Pn^{-1} \approx mc^2$, where c is the sound velocity, while in the van der Waals case it is considerably smaller. Thus it is not surprising that the smooth particle approach is successful only in the latter case. In conventional continuum mechanics a constant pressure addition does not affect the accelerations at all, because they depend upon the *gradient* $\nabla\cdot P$. It is obvious that an additional constant pressure in the combined term, $(P/\rho^2)\cdot\nabla w$, used in smooth particle method does *not* affect the accerelations for a 1-dimensional regularly-spaced system because of the symmetric cancellation of forces. But if the particles move or vibrate, then the nonlinear part of $(P/\rho^2)\cdot\nabla w$ by analogy with molecular dynamics melting affects the accelerations. Freezing can be avoided by using the difference form used in the flux calculation, $(P_i - P_j)/\rho_{ij}$. This expression does not guarantee the conservation of the total momentum and turns out to be unstable.

We use three different forms of weighting functions described in Chapter II: B spline, Lucy's, and Cusp weighting functions. The reason why we use the different weighting functions is that SPAM algorithm depends explicitly on the weighting function. We see the different results due to different weighting function in Section 5.5. We also calculate the temperature bifurcation and the Nusselt number versus Rayleigh number and estimate the critical Rayleigh number of our system. In the next Section we describe compressible continuum Navier-Stokes model.

5.4 Continuum Flow Solutions

Only a brief description of our method for solving the Navier-Stokes equations is warranted, because the approach we developed turned out not to be new [16]. We spanned the system with a grid of square cells, evaluating $\{v, e, \partial v/\partial t, \partial e/\partial t\}$ at the grid points, and $\{\rho, P, Q, \partial\rho/\partial t\}$ at the cell centers. The centered-difference equations for the time development of $\{\rho, v, e\}$ at these fixed locations were integrated with the same fourth-order Runge-Kutta integrator which we used in the Smooth Particle work. The required values of density from cell centers just outside the system were set equal to the nominally constant reference-state value of unity. With this scheme we found no trouble in obtaining fully converged results for systems of several thousand cells.

Two aspects of the continuum results were especially interesting. First, we found that there is a considerable range of Rayleigh-Number values for which the kinetic energy varies almost exactly linearly when plotted as a function of $Ra^{-1/2}$. Furthermore, the slopes and intercepts of these lines also varied almost exactly linearly with L^{-2}. These two simple linear dependences made it possible to extrapolate accurately to a fully-converged

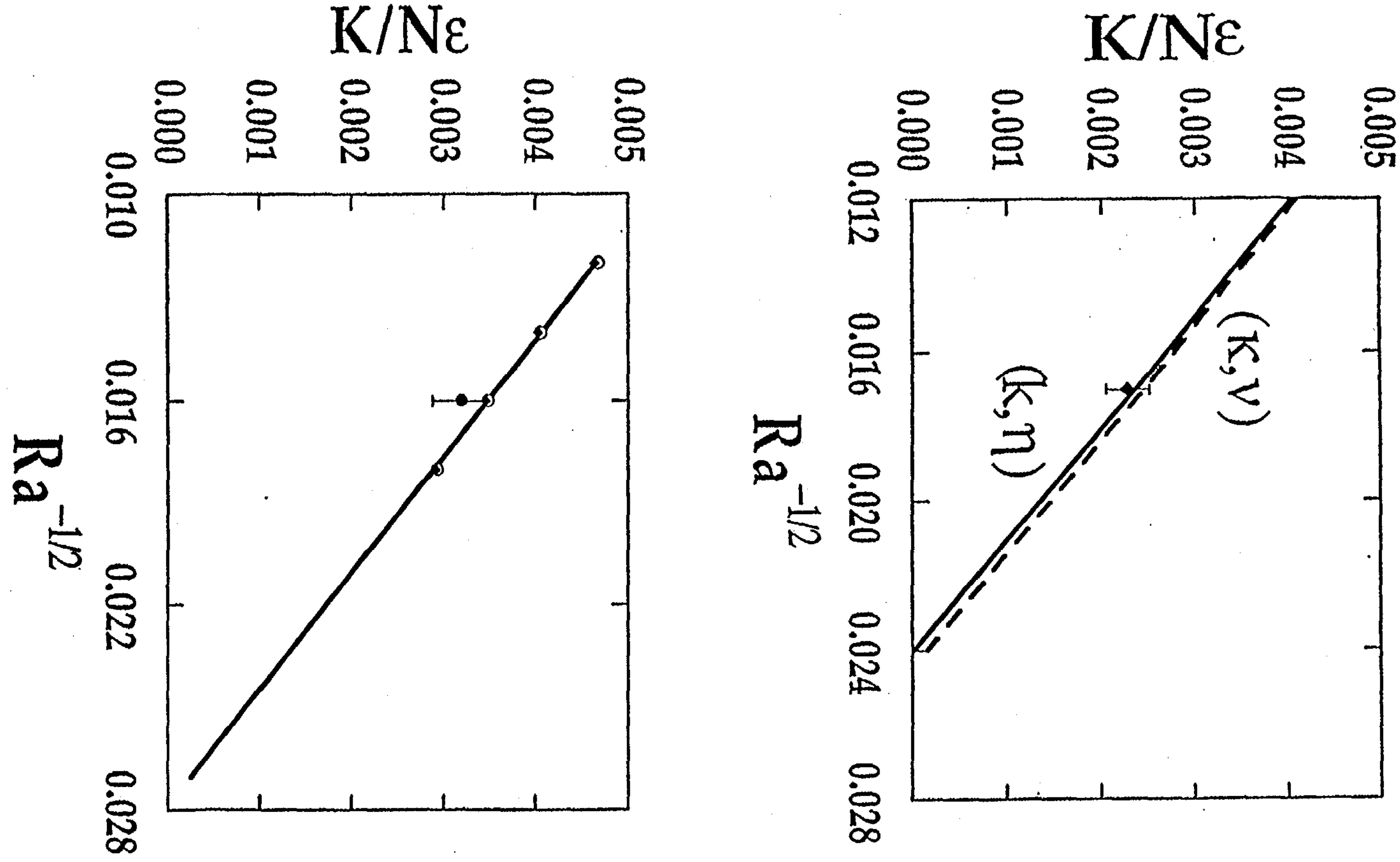

Figure 5.3. Fully-converged (L → ∞) variation of reduced kinetic energy K/Nε with Rayleigh number Ra with periodic lateral boundaries, fixed upper and lower boundaries, an aspect ratio of 2, and $\eta \equiv k/k_B \propto (m\varepsilon)^{1/2}/\sigma$. Both ideal-gas (top) and van der Waals (bottom) results are shown. In the ideal-gas case additional results using $\nu \equiv \eta/\rho \equiv \kappa \equiv k/(\rho C_V) \propto (\varepsilon/m)^{1/2}\sigma$ are included for comparison. In the van der Waals graph empty circles are results from 60x30 squares system and diamonds are results from 40x20 squares system. For the ideal gas system the fully-converged critical Rayleigh numbers are 1680 and 1729. For the van der Waals system the fully-converged critical Rayleigh number is 1287. The Lucy-weighted smooth particle points shown, for comparison to the Navier-Stokes solutions, are the results of simulations using 5000 particles.

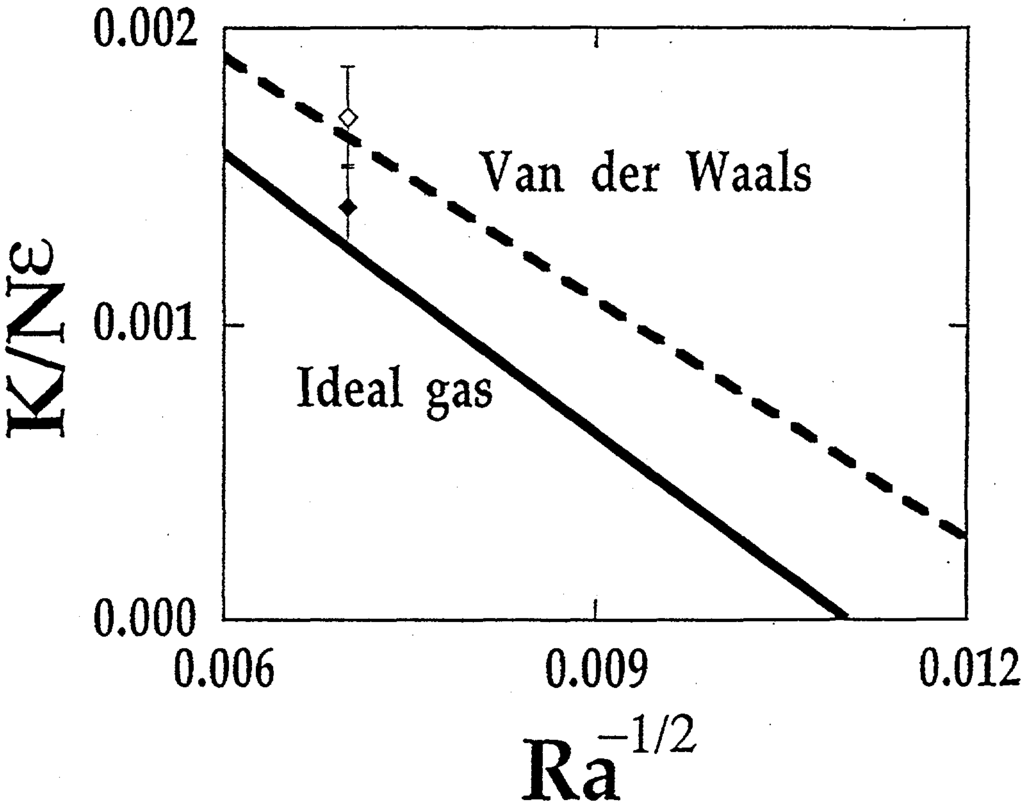

Figure 5.4 Fully-converged (L → ∞) variation of reduced steady-state kinetic energy K/Nε with Rayleigh number Ra in square systems with four reflecting boundaries. The temperature along the lateral boundaries is a linear interpolation between the temperatures of the two horizontal boundaries. The points shown are the results of corresponding Lucy-weighted smooth particle simulations using 1600 particles.

critical Rayleigh Number using just a few calculations, with either NxN or Nx2N square zones and with N values of 30, 40, 50, ... Fully-converged (extrapolated) results are shown in Figures 5.3 and 5.4 for the two kinds of boundary conditions. These numerical results make it possible to assess the accuracy of the Smooth Particle solutions discussed in the following section.

5.5 Results and Discussion.

5.5.1 Nusselt number calculation [1-5]

In the absence of convection, there would be a uniform vertical temperature gradient and a thermometric flux $F_o = \kappa\Delta T/L$, where L is the system height. When the convection occurs the horizontally averaged thermometric flux defined in the laboratory frame is

$$F = \langle v_y T - \kappa \partial T/\partial z \rangle \tag{25}$$

and the normalized flux or Nusselt Number is given by their ratio [2, 4, 5]:

$$Nu = F/F_o = L/\Delta T[(1/\kappa)\langle v_y T\rangle - \langle dT/dz\rangle]. \tag{26}$$

We calculated the Nusselt number for different Rayleigh numbers. The Rayleigh number [$Ra = (g\alpha\Delta TL^3)/(\kappa\nu)$] is given by equation (8) and depends on the product of thermal diffusivity κ and kinematic viscosity ν. For the same size system with same temperature difference, different artificial coefficients of thermal diffusivity and kinematic viscosity correspond to different Rayleigh numbers.

We simulate 2500 (50x50) particles system ($\Gamma = 1$) using B spline weighting function with smoothing length 2.5, four reflective boundaries, dense fluid equation of stste, high temperature at lower boundary 10, lower temperature at upper boundary 0.5, gravity 1 as a function of thermal diffusivity and kinematic viscosity. Figure 5.5 shows Nusselt number of the system as a function of Rayleigh number represented by the product of $\kappa\nu$. In this calculation, we keep the Prandtl number unity.

Figure 5.6 shows the same system averaged temperatures at the three different positions as a function of Rayleigh number: central temperature, average of two vertical edge temperatures, and horizontal temperature average at the central height.

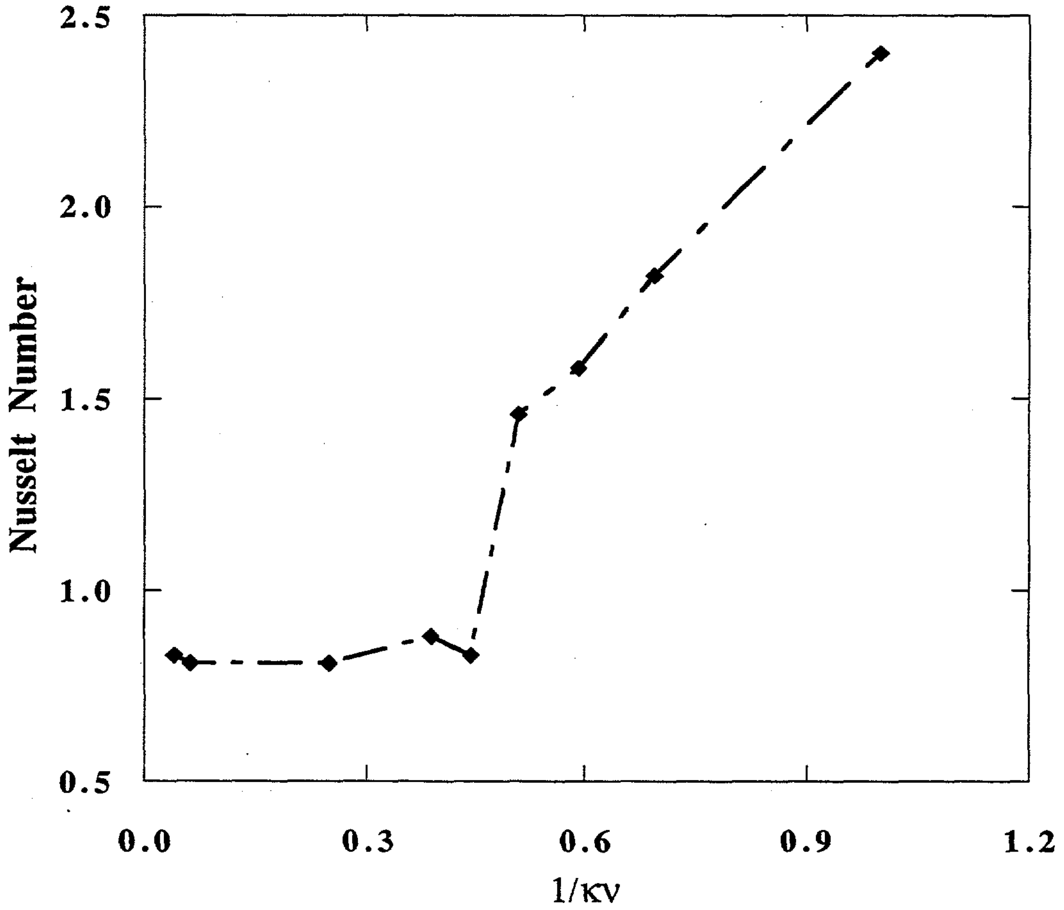

Figure 5.5 Nusselt number as a function of 1/κν. The system consists of 2500 particles (50x50) with four reflective boundaries. Dense-fluid equation of state is used. In equation (8) Rayleigh number Ra = $(g\alpha\Delta TL^3)/(\kappa\nu)$ ($\equiv 47500/\kappa\nu$), where gravity g = 1.0, temperature difference $\Delta T = 9.5$, system height L = 50, thermal expansion coefficient α = 0.04 for dense-fluid equation of state. The critical Rayleigh number occurs about $1/\kappa\nu$ = 0.45, corresponding to Ra = 21375.

For systems with Rayleigh number bigger than the critical Rayleigh number in the Figure 5.5, we also see temperature bifurcation in Figure 5.6 [13, 20]. The critical Rayleigh number depends on the boundary conditions in temperature which is affected by the heat diffusion equation and, in the equation of motion, by the slip or no slip boundary condition on velocity.

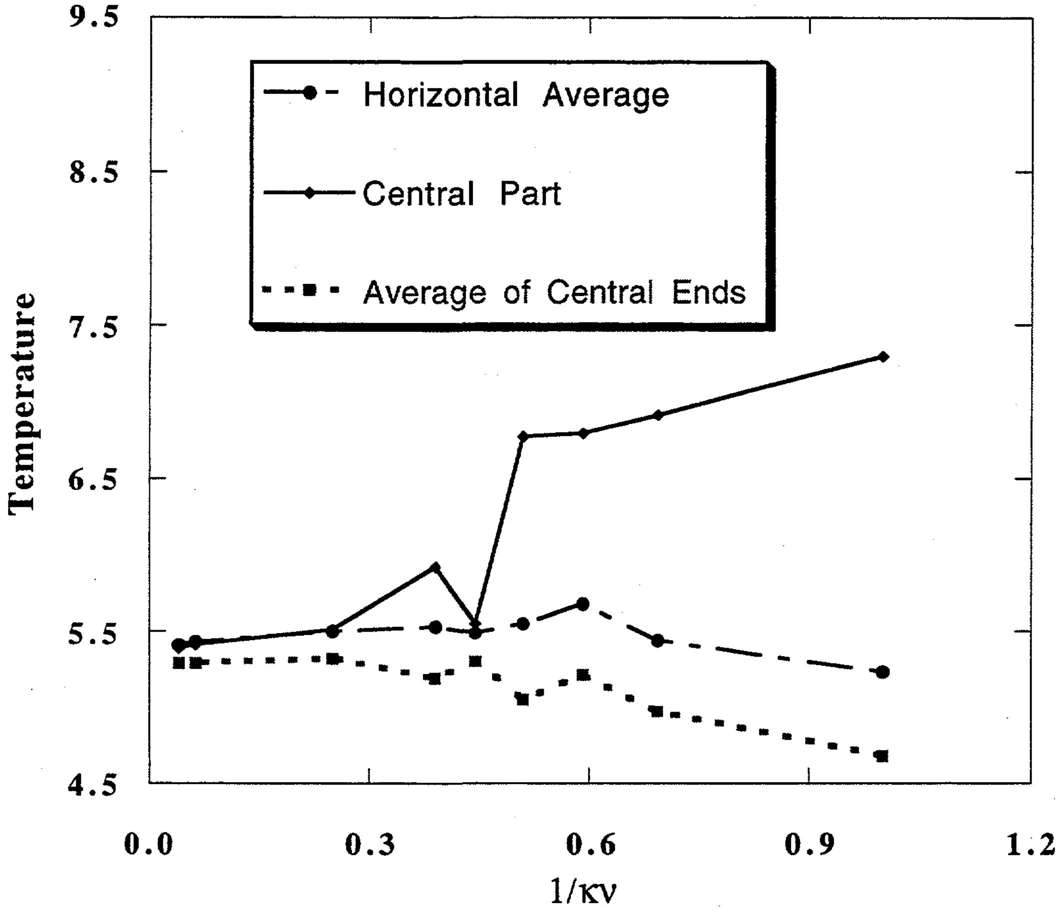

Figure 5.6 Temperature bifurcation as a function of $1/\kappa\nu$. This system has the same physical parameters as those used in Figure 5.5. Horizontal average value is the average of the horizontal temperature at the central hight of the system. Central part is the average temperature of the central area of one interaction range at the center of the system. Average central ends is the average temperature of two lateral edges at the central height of the system. We see the temperature bifurcation at the critical Rayleigh number of Figure 5.5.

Table III shows the numerical values of Figures 5.5 and 5.6. In the table, Nu represents Nusselt number, Ha horizontal average, Cp central part, Ae average of central ends. In the dense fluid equation of state temperature depends on the system density and internal energy with respect to their unit reference values [15].

Table III Numerical values of Nusselt number and temperature of horizontal average (Ha), central part (Cp), and average central ends (Ae) in Figures 5.5 and 5.6. Corresponding Rayleigh number Ra = 47500/($\kappa\nu$) for the system.

Transport coefficients ($\kappa=\nu$), ($1/\kappa\nu$)	Nusselt number	Temperature		
	Nu	Ha	Cp	Ae
1.0 (1.000)	2.40	5.23	7.29	4.68
1.2 (0.694)	1.82	5.44	6.91	4.97
1.3 (0.592)	1.58	5.68	6.79	5.21
1.4 (0.510)	1.46	5.55	6.77	5.05
1.5 (0.444)	0.83	5.49	5.55	5.30
1.6 (0.391)	0.83	5.53	5.92	5.19
2.0 (0.250)	0.82	5.50	5.51	5.32
4.0 (0.063)	0.82	5.43	5.41	5.29
5.0 (0.040)	0.83	5.41	5.39	5.29

It is hard to analyze an intrinsic shear viscosity quantitatively because intrinsic shear viscosity is a function of energy and nonlinear as is shown quantitatively in Figure 5.7. We discuss this problem in Section 5.5.5 in detail.

We simulate 5000 (100x50) particles system ($\Gamma = 2$) using Lucy weighting function with smoothing length 3, ideal gas equation of state, vertically periodic boundary conditions, transport coefficients, $\kappa = \nu = 1$, gravity 1/50. The system corresponds to Rayleigh number about 2500. Figure 5.8 shows the roll patterns, iso-temperature curves, and isodensity curves. This system size and transport coefficients are large enough so that the intrinsic shear viscosity effect is negligible compared to the values shown in Figure 5.7. But eventually the intrinsic viscosity property can be reduced by using many particles or longer smoothing length which we saw in Chapter 3.

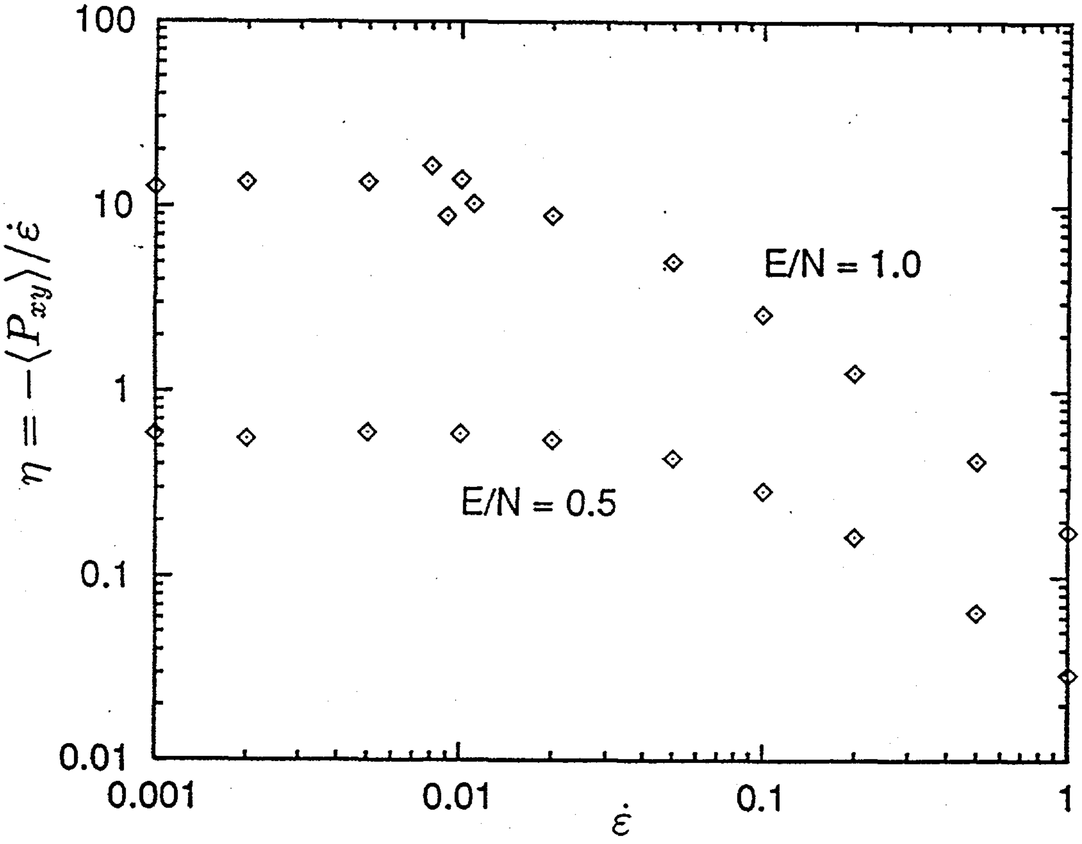

Figure 5.7 Shear viscosity coefficients as a function of strain rate in microscopic model with Lucy potential function with smoothing length 3 at energies E = Nε and E = Nε/2. Viscosity coefficients decrease as the strain rates increase. Data from Professor H. A. Posch [University of Vienna].

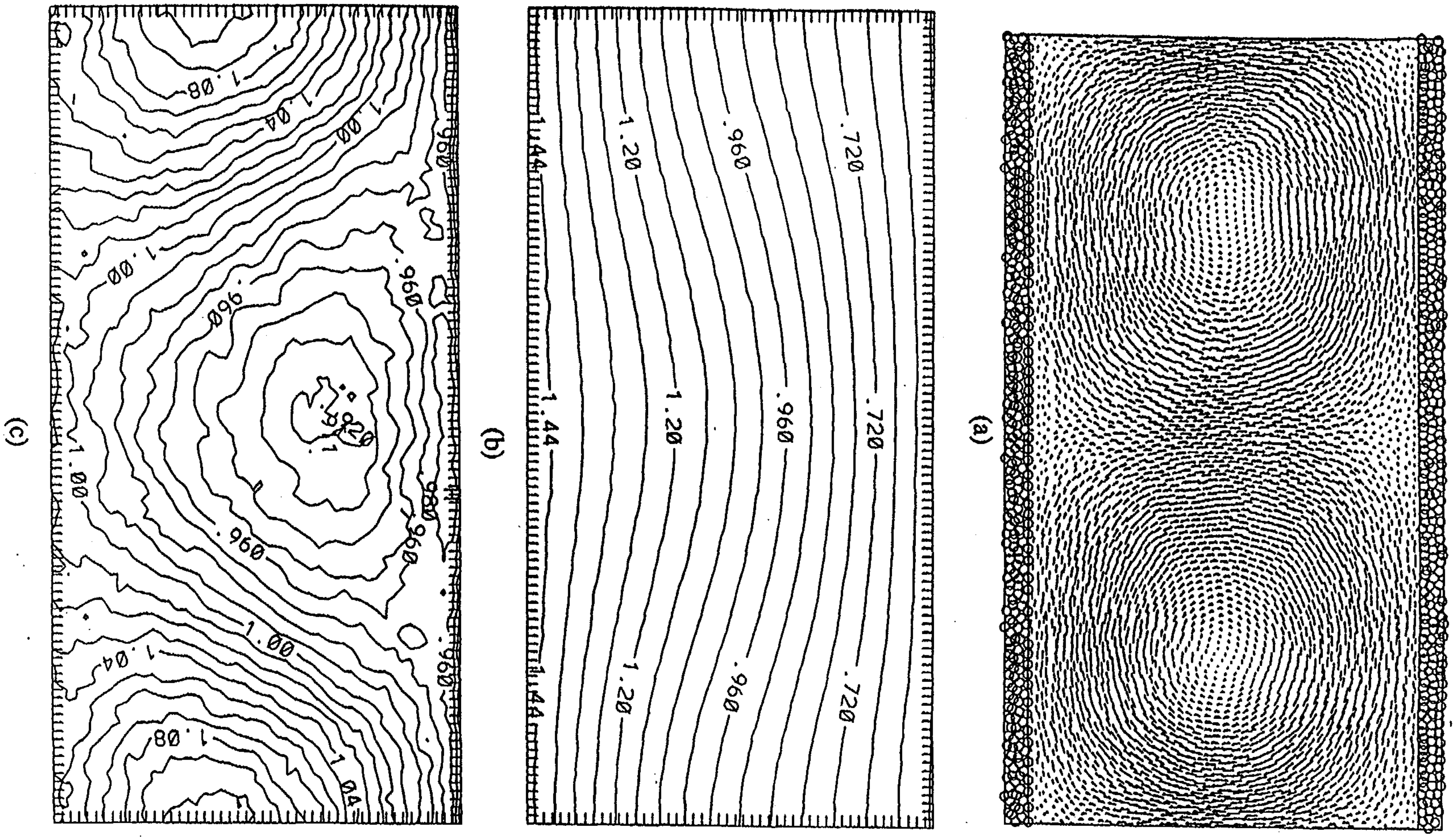
(a)

(b)

(c)

Figure 5.8 Rayleigh-Bénard rolls, Iso-temperature and Iso-density contours near the critical Rayleigh number 2500. This system contains 5000 particles (100x50) (Γ=2) with the ideal gas equation of state. Lucy's weighting function with smoothing length 3 is used. Transport coefficients $\kappa = \nu = 1$. (a) Rayleigh-Bénard rolls in vertically periodic boundary system. (b) Iso-temperature contours. (c) Iso-density contours. The temperature contours are slightly convex around the critical Rayleigh number.

5.5.2 Different weighting function effects.

In Table II of Chapter 3, we showed that SPAM has different intrinsic shear moduli for the three different weighting functions: B spline, Lucy, and Cusp weighting functions. The Cusp weighting function has the smallest shear modulus and Lucy has the largest one.

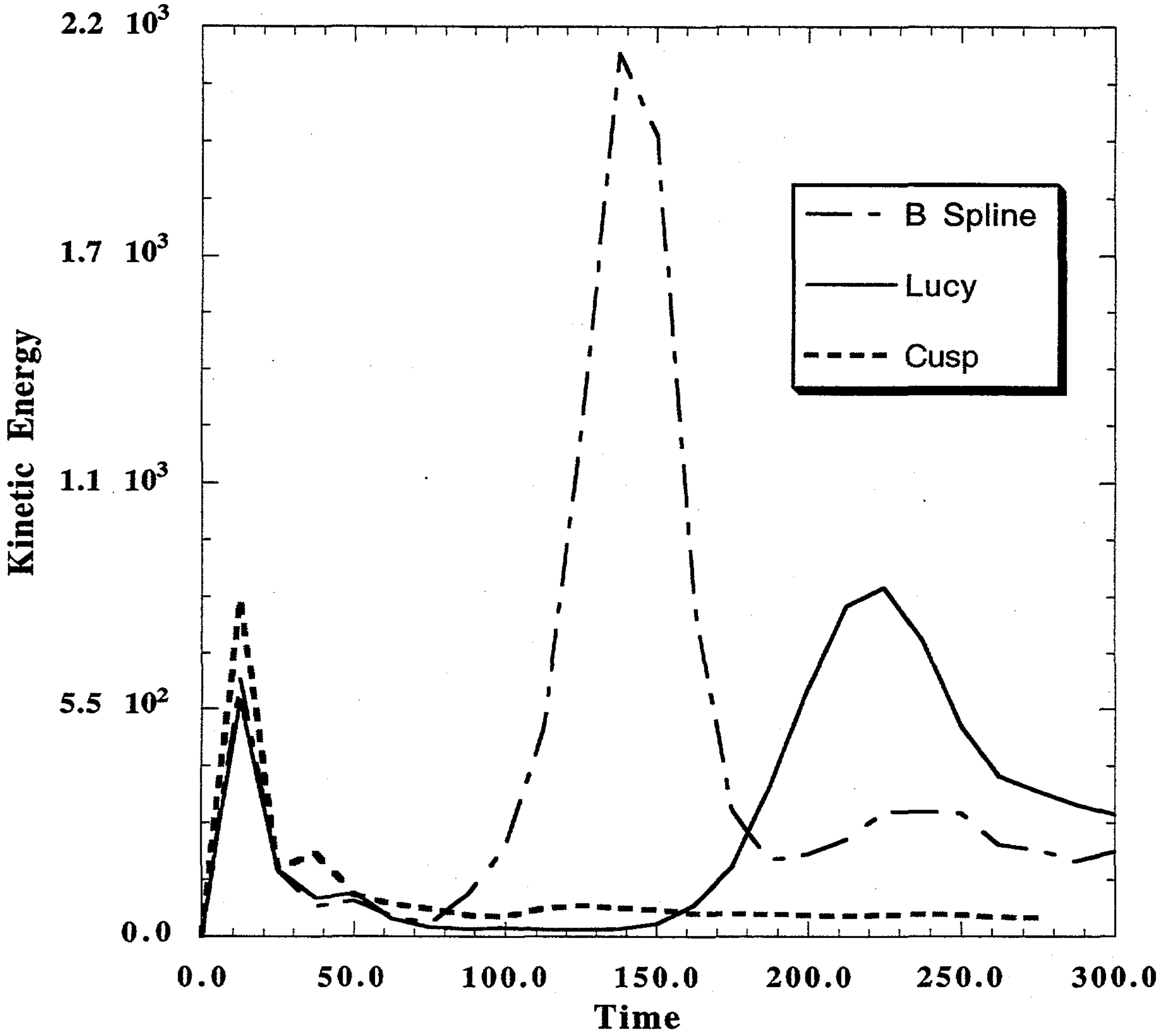

Figure 5.9 Kinetic energy fluctuation as a function of time for three weighting functions: B spline, Lucy, and Cusp weighting functions. Dense fluid equation of state is used. We see that the initial kinetic energy increase depends inversely on the shear moduli calculated in Chapter 3 at the early time of about 25, about one half the sound traversal time.

This effect appears in the kinetic energy fluctuations as a function of time in Figure 5.9. At the early time in this graph, we see the effects of the intrinsic shear modulus: the kinetic energy increase is inversely proportional to the intrinsic shear modulus of the weighting function.

The calculation was done on the square lattice system with the same horizontal and vertical dimension (= 50) so that the total number of particles are 2500. Initially the particles are placed on the square lattice site with no velocity at all. Boundary conditions used are reflective ones, with image particles. In this system the global density of the system is unity. As transport coefficients, we use the same value for thermal diffusivity and kinematic viscosity (= 0.4) so that Prandtl number is unity. As an equilibrium pressure, we used the dense fluid equation of state and smoothing length (= h) is 2.5.

Fully developed Rayleigh-Bénard rolls show up in the second cycle of kinetic energy increase, in the middle part of Figure 5.9. Unit gravity is big enough to set up the initially static equilibrium status without convection. We then increase the gravity step by step to adjust the whole system in equilibrium condition during the calculation. Otherwise the system breaks down. The shapes of fully developed Rayleigh-Bénard rolls are different with different weighting functions with reference system, as shown in Figure 5.10. Two symmetric rolls are developed with B spline weighting function, two skew symmetric roll for Lucy weighting function, and no roll at all for Cusp weighting function. The hydrodynamic equations do not necessarily provide a unique flowing path so that two symmetric rolls in B spline and two skew symmetric rolls (big one and small one) in Lucy could both possibly be correct in the given condition. But the Cusp weighting function definitely fails for this problem because it has no rolls at all. While developing the rolls, different weighting functions change the initial square lattice structure to different lattice types: the Cusp weighting function gives triangular lattice, the B spline tends to order the particles in pairs, and the Lucy weighting function makes another type of structure. The lack of rolls in the Cusp case is due to the forming of a stable triangular lattice with lower

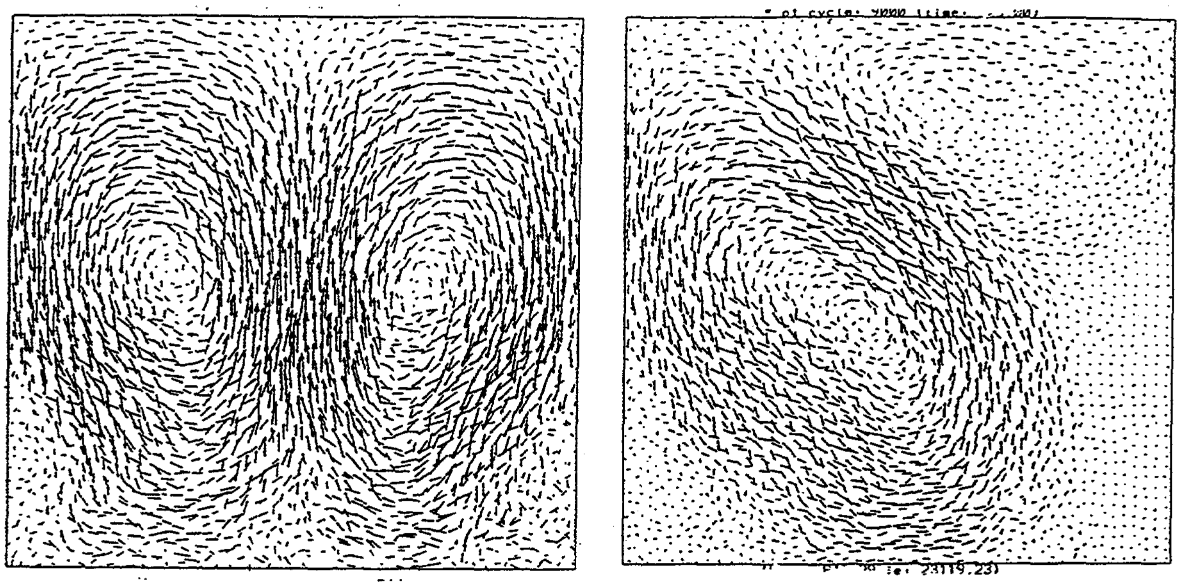

B spline

Lucy

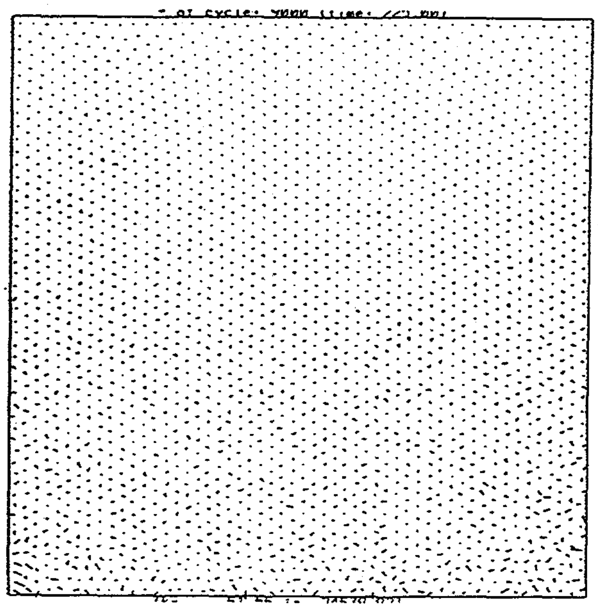

Cusp

Figure 5.10 Fully developed Rayleigh-Bénard rolls for three different weighting functions with the system shown in Figure 5.9. Dense fluid equation of state is used. Two symmetric rolls using the B spline weighting function. One skew symmetric big roll and one small roll using the Lucy function. No roll using the Cusp weighting function. This experiment shows that the solid-like Cusp weighting function is not appropriate for this problem even though it shows the lowest shear modulus in Chapter 3.

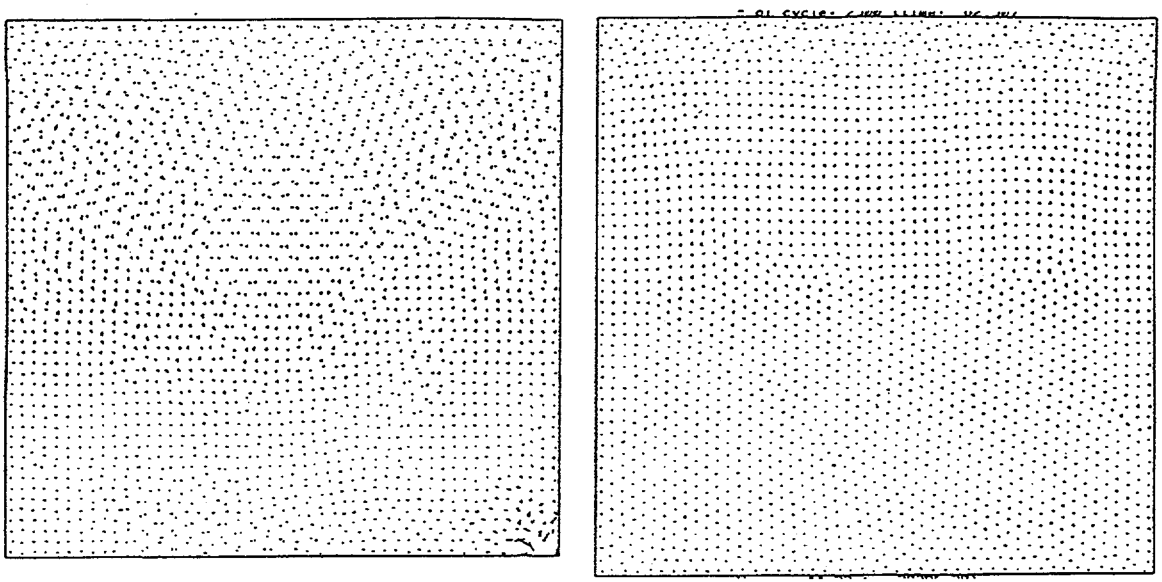

B spline

Lucy

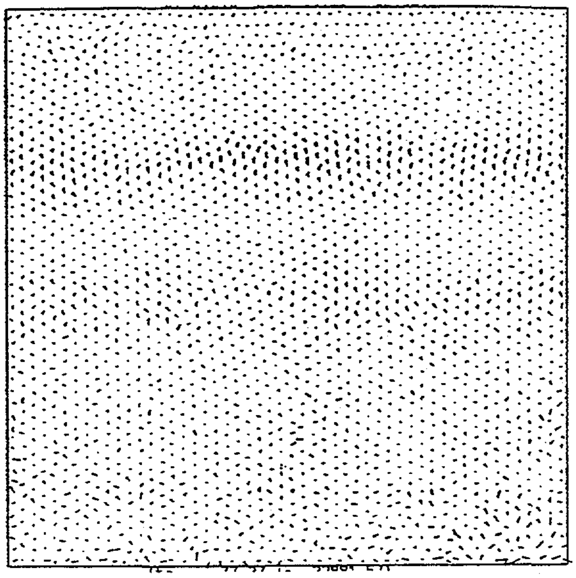

Cusp

Figure 5.11 Characteristic particle motions at time 62.5 for three different weighting function long before making rolls with the same system parameters as in Figure 5.9. The dense fluid equation of state is used. Note the pair particle structure for the B spline weighting function. Lucy's crystal structure forms from an initial square lattice structure. The Cusp's triangular lattice structure comes from that same initial square lattice structure. This crystalization phenomenon can be understood through the analogy with molecular dynamics.

energy than the square lattice. Figure 5.11 shows typically different particle motions corresponding to different weighting functions.

5.5.3 Different boundary condition effects.

As discussed in Chapter 3, we can have different reflective boundary conditions with different boundary particles: image particles and fixed particles [15]. We simulated a system with two vertical periodic boundaries and an aspect ratio $\Gamma = 2$. See Figure 5.12. Figure 5.13 shows the roll patterns of the same systems ($\Gamma = 1$, B spline weighting function with smoothing length 2.5, transport coefficients [$\kappa=\nu=0.4$]) with different types of boundary particles. Both conditions can be applied. The image particle choice is much less intrusive.

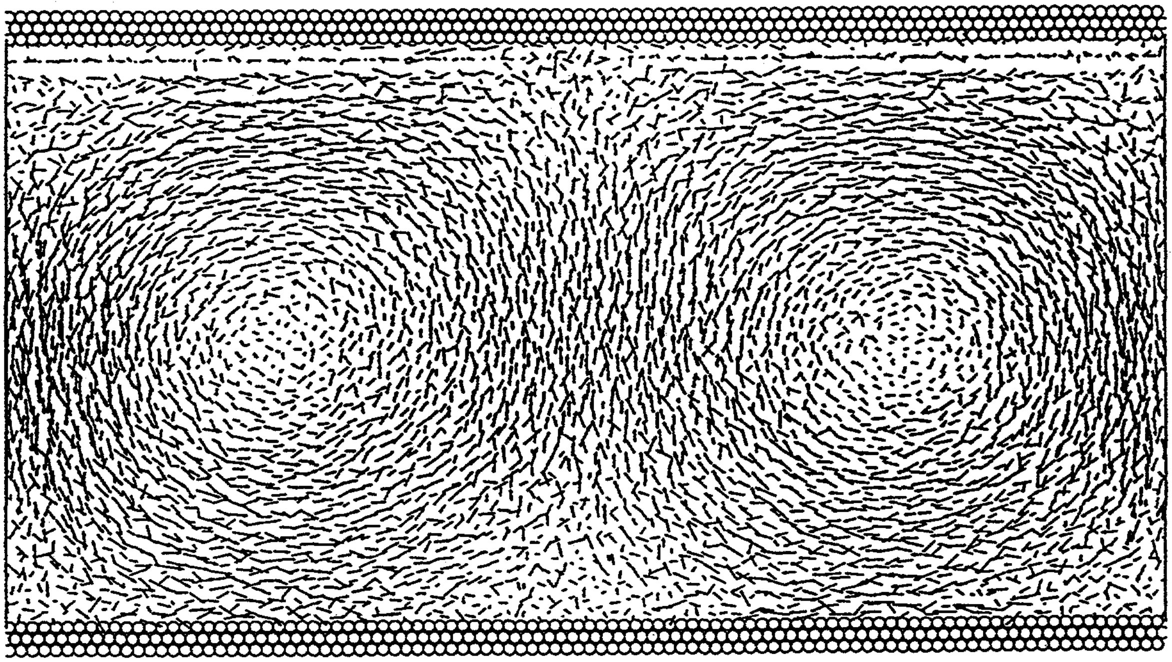

Figure 5.12. Rigid boundary rows of fixed particles (with specified temperatures) are used to confine the bulk fluid. The fixed boundary particles are shown as open circles while the bulk smoothed particles are indicated by arrows with a length proportional to the individual particle velocities. The illustration shows an ideal gas Rayleigh-Bénard flow with $\eta \equiv k/k_B = 0.5(me)^{1/2}/\sigma$ at a Rayleigh Number of 10 000. There are 5000 bulk particles in a rectangular 50 x 100 box. Data from Professor H. A. Posch [University of Vienna].

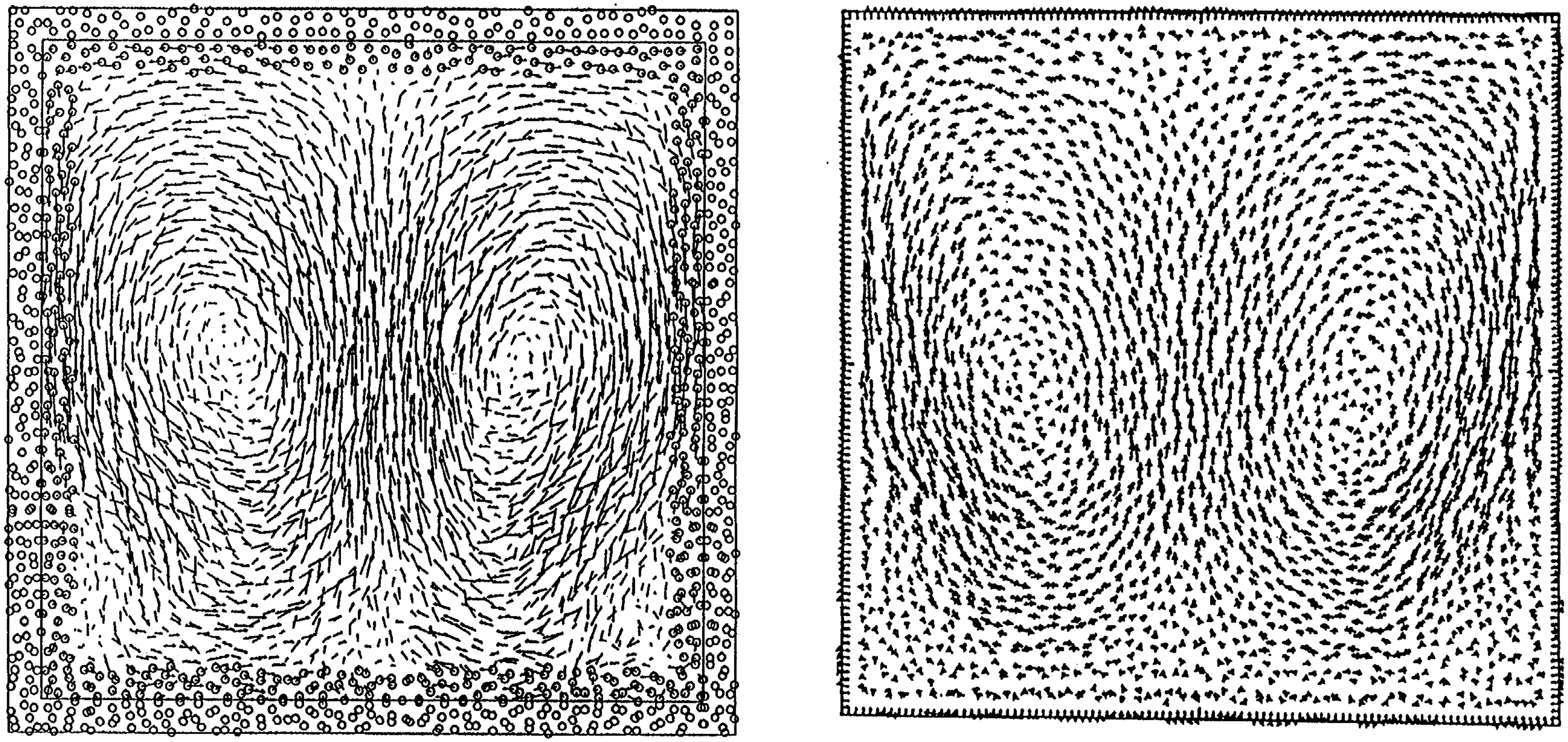

(a)

(b)

Figure 5.13 Rayleigh-Bénard rolls for different boundary particles. Both systems have 2500 particles (50x50) and use the dense-fluid equation of state. Transport coefficients $\kappa = \nu = 0.4$. Rayeligh number is about 250 000. (a) image particles (b) fixed particles. Figure (b) is calculated by Dr. Carol G. Hoover at the Lawrence Livermore National Laboratory. They show similar roll shapes.

5.5.4 The effects of equation of state [15].

The equation of state is the required material description in hydrodynamics. We compare results with two different equations of state: a dense-fluid equation of state and an ideal gas equation of state with the specific heat ratio two. The two systems are exactly the same except for the value of gravity: in the dense fluid gravity is unity but 0.2 using the ideal gas equation of state system. These values were estimated from equation (14). Gravity in the ideal gas equation of state is approximately ΔT/L and the pressure in dense fluid is approximately five times greater than that of ideal gas equation of state near the equilibrium region. Therefore, the different gravity values do not change the essential physics.

A dramatic difference between the two systems is shown in the direction of rolls: up in the center in the dense fluid system and down in the center in the ideal gas system. Figure 5.14 shows two different roll directions for the two different equations of state. We calculated the iso-temperature curves and iso-density curves for the corresponding systems shown in Figure 5.14. Figure 5.15 shows the iso-temperature profiles. In the ideal gas case with central downward stream line, iso-temperature profiles show a concave shape. But in dense fluid with the central upward stream line, iso-temperature profiles show a convex shape. Figure 5.16 shows iso-density profiles for the two systems. Density profile is not linear for the fully developed rolls. However, the ideal gas system changes its roll directions, first counter clockwise then clockwise then counter clockwise, ... While changing the roll directions, as an intermediate step the system displays four rolls. From this result, we see that the solutions of hydrodynamic systems are not unique.

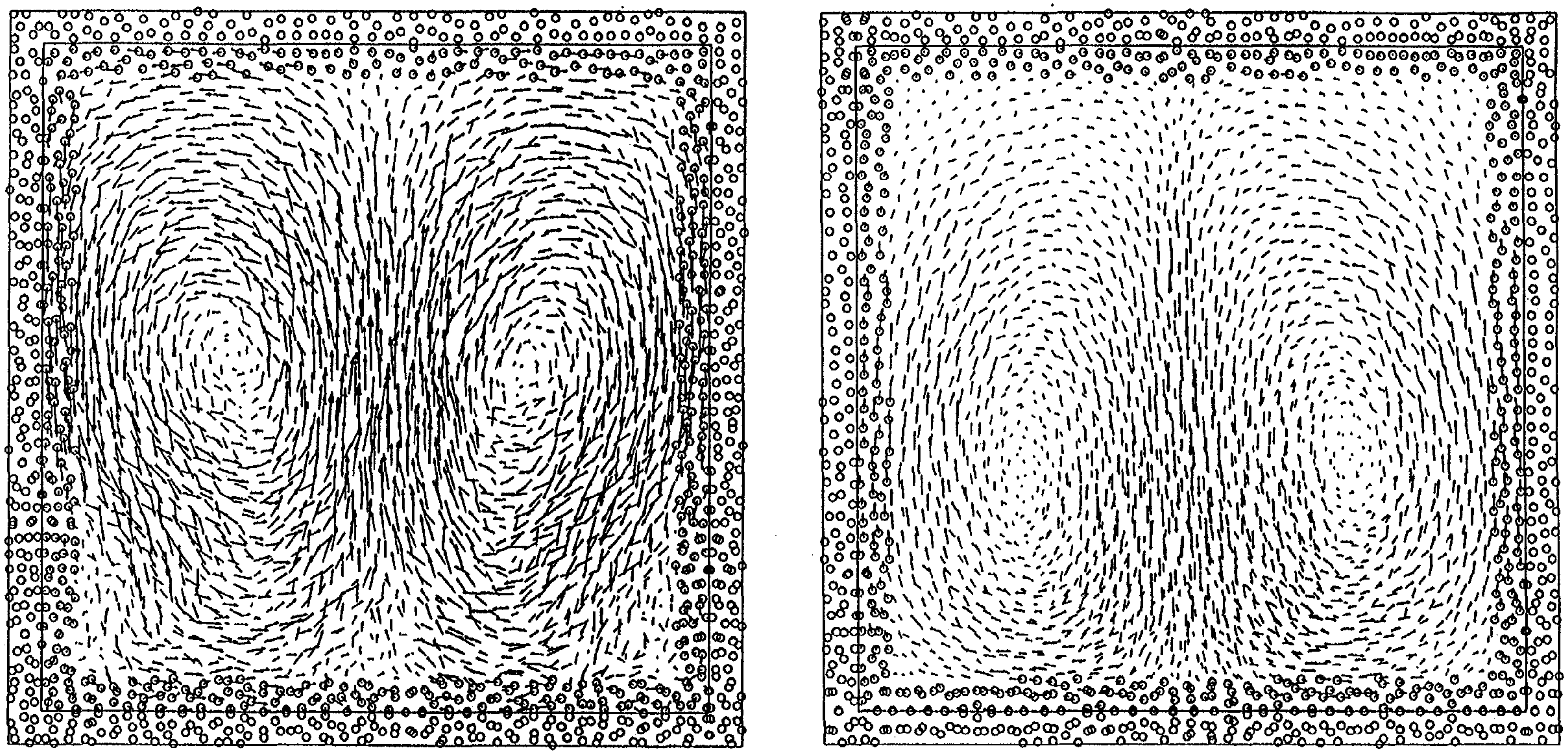

(a) (b)

Figure 5.14 Fully developed rolls with two equations of state: (a) Dense-fluid equation of state Rayleigh number is about 250 000. (b) Ideal gas equation of state. Rayleigh number is about 1 000 000. Two systems are the same system as with Figure 5.9: transport coefficients $\kappa = \nu = 0.4$, hot temperature 10 and cold temperature 0.5, B spline weighting function with smoothing length 2.5. The roll direction is different for different equation of states. For the ideal gas equation of state, however, the roll direction changes during a long calculation. As an intermediate state it has four rolls.

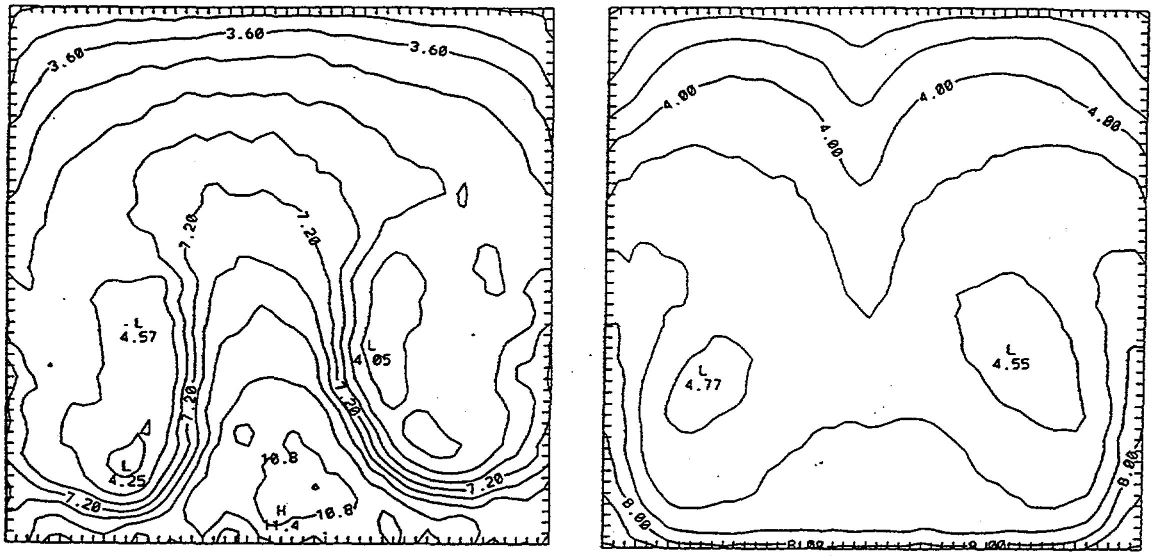

(a) (b)

Figure 5.15 Iso-temperature profile of the rolls corresponding to Figure 5.14. (a) dense fluid equation of state: convex shape corresponding to central upward stream. (b) ideal gas equation of state: concave shape corresponding to central downward stream.

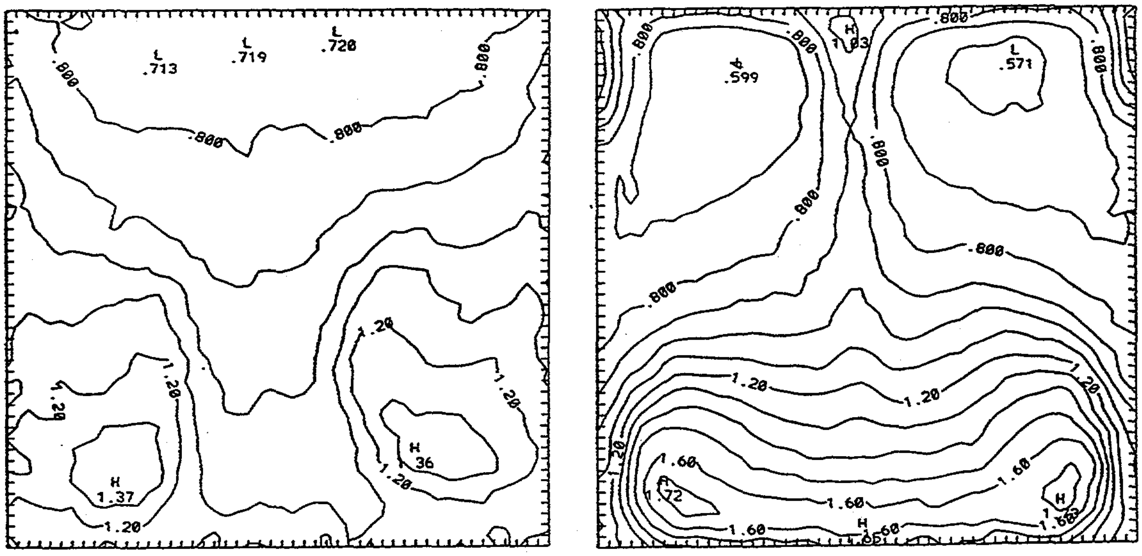

(a) (b)

Figure 5.16 Iso-density profile of the rolls corresponding to Figure 5.14. (a) dense fluid equation of state. (b) ideal gas equation of state.

5.5.5 Quantitative analysis of intrinsic shear viscosity.

This analysis is based on molecular dynamics data calculated by Professor H. A. Posch at the University of Vienna, shown in Figure 5.7. He calculated the viscosities for the total energy $E = N\varepsilon$ and $E = N\varepsilon/2$. We call them hot and cold particles respectively. For hot particles, temperature or kinetic energy is 0.54 and for cold it is 0.07. Shear viscosities of hot and cold particles are 12 and 0.6 as shown in the Figure 5.7. Posch used Lucy's weighting function with smoothing length 3 for this calculation.

To understand the results consider the following approximate arguments. The mean force on a particle is proportional to the potential gradient times the square root of the number of interacting neighbor particles:

$$F = -\phi' \sqrt{N}, \qquad (27)$$

where N is the number of interacting neighbor particles. The velocity of a particle is $\sqrt{(2mkT)}$, where T is temperature. The number of weak collisions required to change this velocity is,

$$N_c = (u/F)^{\#}, \qquad (28)$$

where u is velocity and # is the number of degrees of freedom. The collision time is equal to the potential range divided by the velocity,

$$\tau_c = L/u. \qquad (29)$$

The relaxation time is equal to the collision time times the number of collisions,

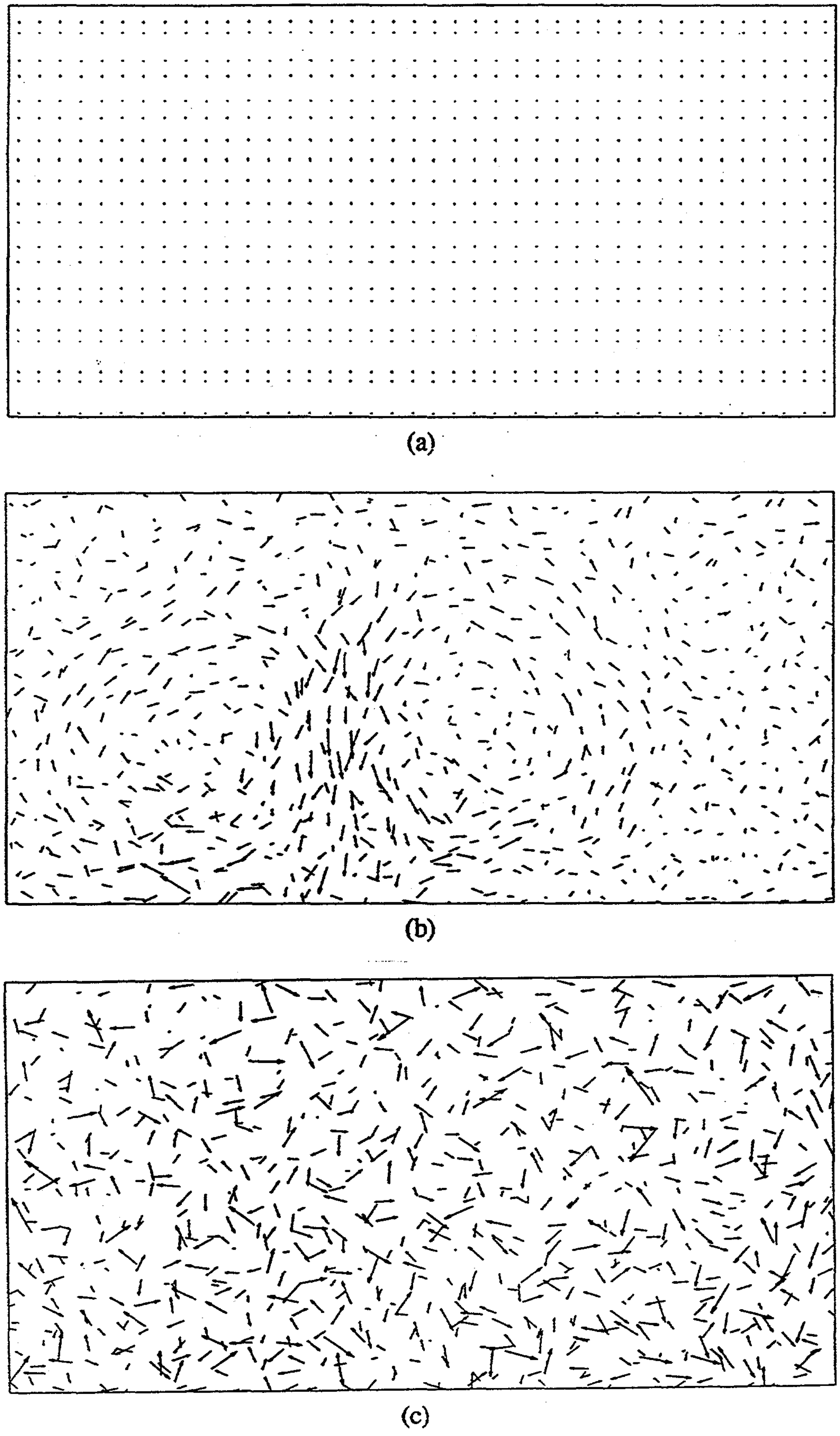

Figure 5.17 Zero viscosity Rayleigh-Bénard rolls. The system consists of 800 particles (40x20). Heat conductivity $\kappa = 0.1$, ideal gas equation of state and Lucy's weighting function with smoothing length 3 are used. Initial velocities are zero. (a) time 50, kinetic energy 0.228, (b) time 500, kinetic energy 23.102, (c) time 2000, kinetic energy 61.633.

$$\tau_r = N_c \tau_c. \tag{30}$$

Then the mean free path, λ is calculated by the number of collision times the potential length. Finally the kinematic viscosity ν ($\equiv \eta/\rho \equiv \lambda u/3$) turns out to vary as $T^{3/2}$ for the particles of the thermal velocity $T^{1/2}$. This argument describes the temperature dependence of our viscosities very well and also provides semiquantitative agreement with the numerical values:

$$\eta = 35(mkT)^{1/2}(kT/\varepsilon\sigma), \tag{31}$$

restricted to the case of unit number density $N\sigma^2 = V$. We expect that a similar argument would provide an effective heat conductivity for the Lucy potential, but we have not checked this notion.

Usually the full blooming Rayleigh-Bénard rolls are formed at the maximum energy state in smooth particle simulations. In that maximum energy state, the intrinsic viscosity also increases maximally. The intrinsic viscosity of the Lucy flow, though evidently less than our estimate for an energy $E = N\varepsilon/2$, is still sufficiently great to exceed the specified viscosity, and can dominate the flow. To emphase this point we carried out a simulation with the viscosity set equal to zero (thermal conductivity is still required, in order to drive the flow). Again rolls formed, though irregularly and many in number, suggesting the persence of viscous dissipation in the smooth particle model of an *inviscid* fluid.

Figure 5.17 shows the zero viscosity rolls at times 50, 500, and 2000. Initial velocities are zero. The system consists of 800 particles (40x20). Lucy's weighting function with smoothing length 3 and ideal gas equation of state are used. Rolls are formed clearly at time 500 and it looks as if many rolls are formed later. Heat conductivity $\kappa = 0.1$.

5.5.6 Comparison with Navier-Stokes simulation

The comparison with Navier-Stokes simulations was done for two different system shapes, with aspect ratios of 1 and 2, in order to make contact with earlier calculations [1, 6]. A system with periodic lateral boundaries and an aspect ratio of 2 corresponds closely to Chandrasekhar's classic analysis [6], which predicts — for sticking boundaries — that stable convection begins to occur as the Rayleigh number exceeds 1708. A square system, with specified temperature on the boundaries corresponds to Goldhirsch, Pelz, and Orszag's simulation, using a spectral method [1]. These workers did not estimate the precise critical Rayleigh number for this system. In both cases we control the boundary values of temperature and velocity by specifying these for all image particles. Both Chandrasekhar and Goldhirsch-Pelz-Orszag consider the nearly-incompressible Bousinesq approximation. Though we first believed that the small deviations from Chandrasekhar's analysis were due to our relatively large temperature gradient (with $\Delta T \approx \langle T \rangle$) additional calculations, with much smaller temperature differences ΔT produced only small changes, so that we believe that the Boussinesq approximation is responsible for the disagreements. The usual theoretical perturbation analyses typically assume either an isochoric or an isobaric thermal diffusivity. In fact, for a compressible fluid, any hydrodynamic process is neither isochoric nor isobaric, so that an intermediate heat capacity is appropriate.

In addition to the equilibrium equation of state, irreversible momentum and energy transport must be described. For simplicity, we have in every case chosen constant, and equal, reduced transport coefficients, corresponding to a Prandtl number of unity. We have explored the two simplest choices. First:

$$\eta \equiv k/k_B \propto (m\varepsilon)^{1/2}/\sigma \,, \tag{32}$$

where η is the shear viscosity, k is the thermal conductivity, and k_B is Boltzmann's constant per unit mass. Second:

$$\nu \equiv \eta/\rho \equiv \kappa \equiv k/(\rho C_V) \propto (\varepsilon/m)^{1/2}\sigma\ , \qquad (33)$$

where ν is the kinematic viscosity and κ is the thermal diffusivity $\kappa \equiv k/(\rho C_V)$. C_V is the isochoric specific heat. The transport coefficients η and κ are defined by Newton's and Fourier's Laws in equations (4), (5), (6). Though the two choices above are equivalent for the reference state, they in fact lead to slightly different critical Rayleigh numbers, close to, and bracketing, Chandrasekhar's analytic result based on the Boussinesq approximation. See Figures (5.3) and (5.4).

In the continuum simulations we have assigned the densities and fluxes of image particles to match those of the corresponding bulk particles. Thus the density and fluxes are continuous at all system boundaries. To satisfy the condition of static equilibrium at an exactly constant density, we have further chosen the magnitude of the gravitational acceleration to satisfy the static force balance equation (14). Thus, for the ideal gas equation of state, g is chosen equal to $k_B\Delta T/L$, where k_B is Boltzmann's constant, L is the system height and ΔT is the temperature difference $T_{HOT} - T_{COLD}$. For the dense fluid and van der Waals equations of state, we have used the same constant-density condition, evaluating the thermodynamic derivative $(\partial P/\partial T)_\rho$. All of our simulations have been carried out with the overall reduced density equal to unity; most have a mean reduced temperature $mk_B\langle T\rangle/\varepsilon = (mk_B/\varepsilon)[T_{HOT} + T_{COLD}]/2$ of unity as well.

Our smooth particle calculations were typically carried out with from 500 to 5000 particles, though even a million particles could be used on a modern parallel computer. 500 particles can easily generate convincing and realistic convection currents. See Figure 5.18 for a 512-particle flow using van der Waals' equation of state.

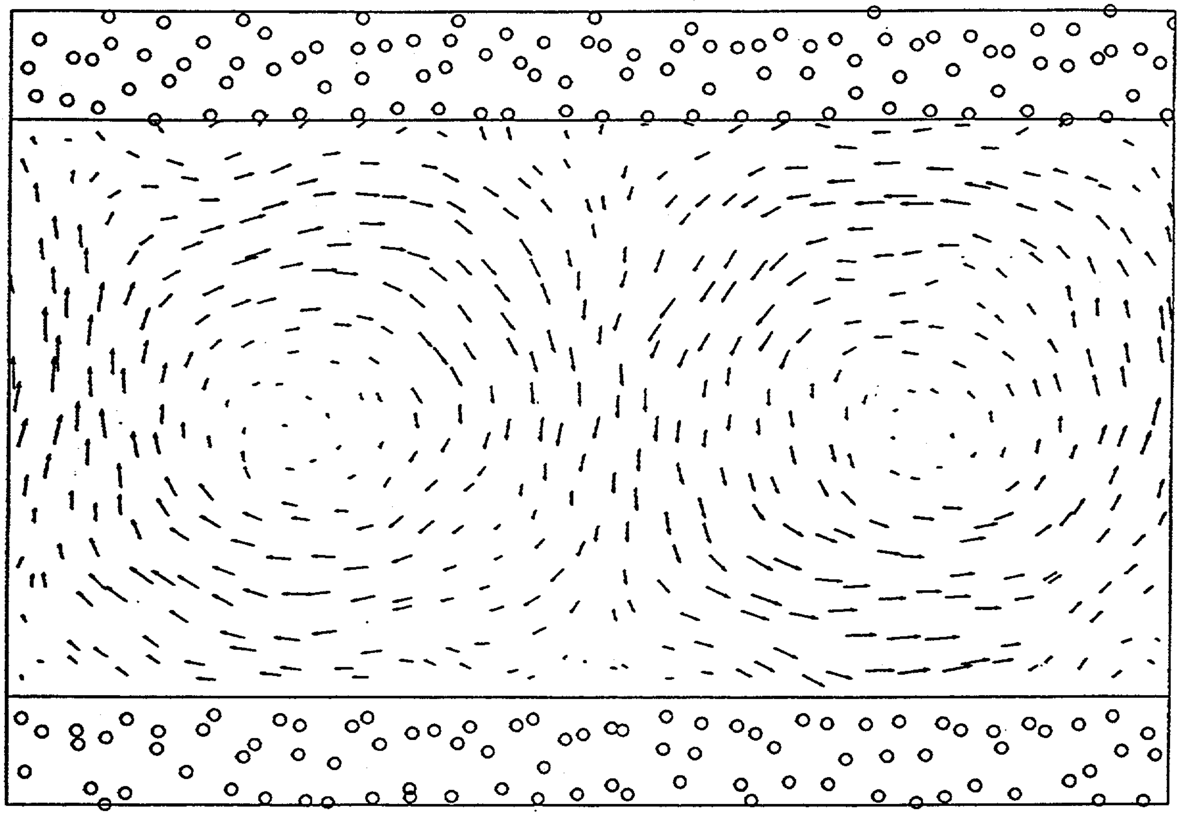

Figure 5.18 Rayleigh-Bénard simulation of a van der Waals fluid using 512 particles and Lucy's weight function. The mean reduced number density, $n\sigma^2 = 1$, is half the maximum and the mean temperature is 27/8 times the critical temperature.

Not only the final states of these simulations but also the approach to these convecting states are faithfully described. In Figure 5.19 we compare the kinetic energy approach to the steady state for an ideal gas using the smooth particle method to that found by solving the Navier-Stokes equations, as described in Section 5.4. In both cases we used the same simple initial velocities:

$$v_x \propto \sin(\pi x/L)\sin(2\pi y/L) \; ; -L < x < +L \; ; \tag{34}$$

$$v_y \propto \cos(\pi x/L)\cos(\pi y/L) \; ; -L/2 < y < +L/2 \, , \tag{35}$$

with an internal energy distribution corresponding to a uniform temperature gradient.

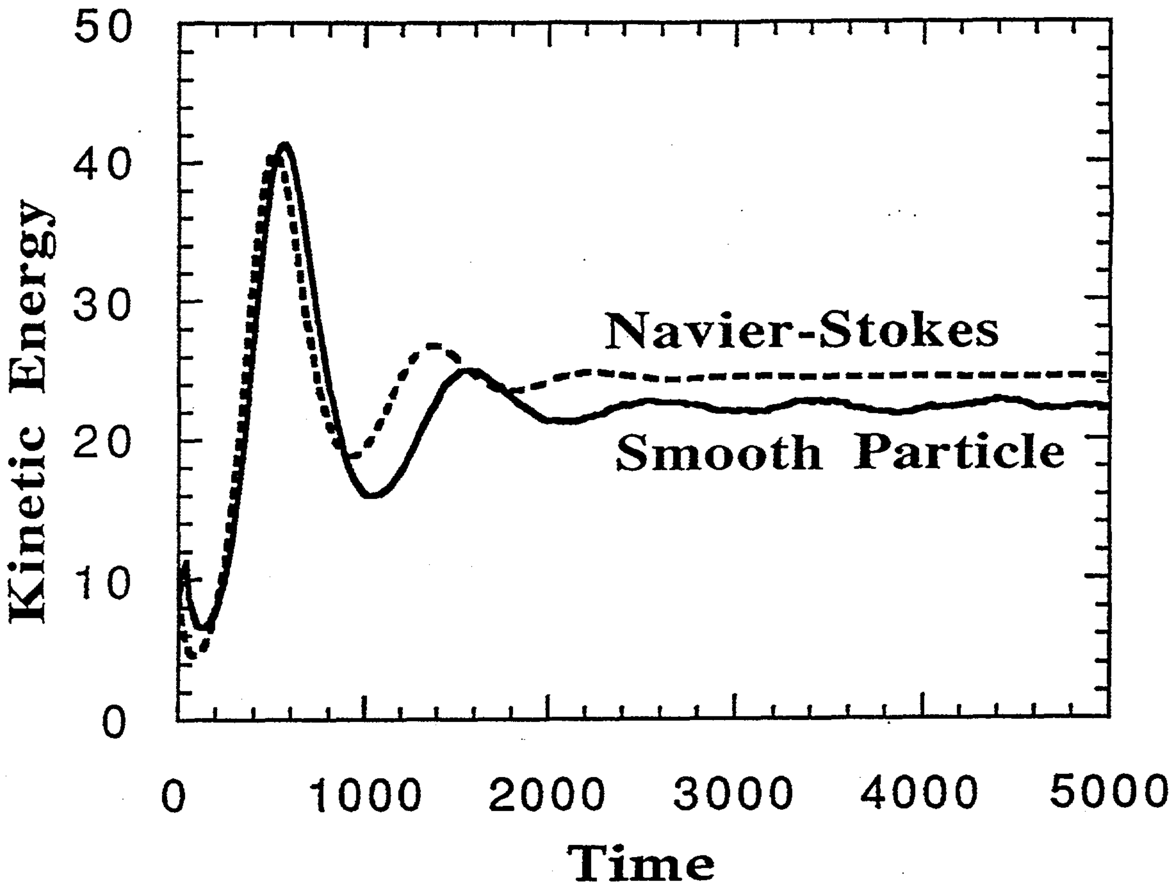

Figure 5.19 Approach of the kinetic energy to the steady two-roll state for the continuum and Lucy-weighted smooth particle methods, applied to an ideal gas [Rayleigh number 10 000 and $\eta \equiv k/k_B = 0.5(m\varepsilon)^{1/2}/\sigma$]. The initial condition has a uniform temperature gradient and two simple rolls, with the functional form given in Section 5.5.6 corresponding to a total kinetic energy about one half the final value.

Errors less than about 1% are disguised by the fluctuations inherent in the smooth particle method. These fluctuations are the analog of kinetic temperature in molecular

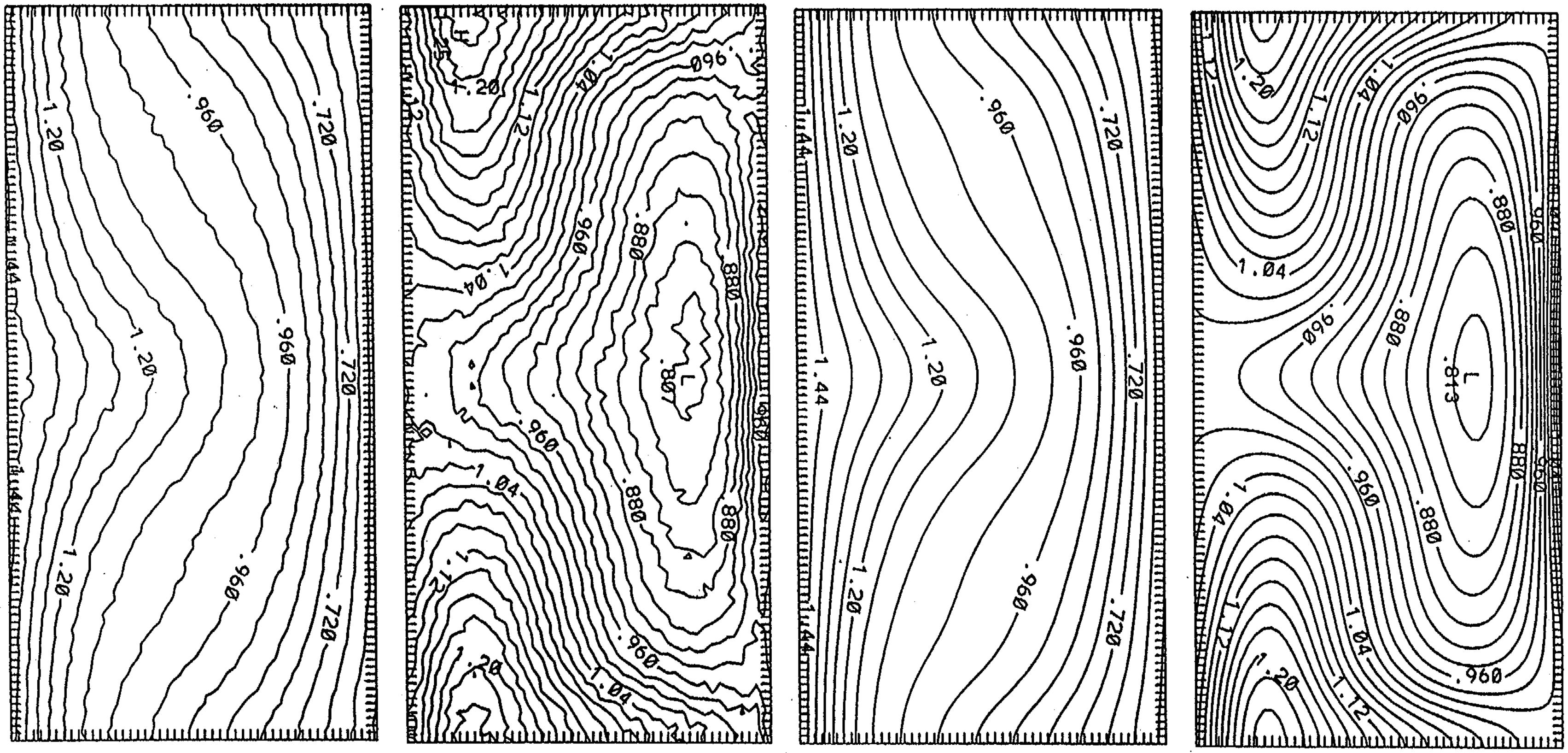

Figure 5.20 Density and temperature distributions for the continuum (upper) and smooth particle (lower) methods using the ideal-gas equation of state with $\eta \equiv k/k_B = 0.5(m\varepsilon)^{1/2}/\sigma$. The Rayleigh number is 10 000 and the aspect ratio is 2. The initial kinetic energy of the 5000 particles was about 9ε. The distributions correspond to a time of $5000(m\sigma^2/\varepsilon)^{1/2}$.

dynamics, a measure of the mean squared deviation of individual particle velocities from the average velocity in their neighborhood, $<v^2> - <v>^2$. Because the kinetic energy of the continuum flows was found to vary nearly linearly with $Ra^{-1/2}$, we have chosen the kinetic energy of the smooth particle flows $(\rho/2)<v>^2$ for a quantitative comparison. We compared the Navier-Stokes and smooth particle kinetic energies per unit mass for Rayleigh numbers 5000 and 10000. From the Navier-Stokes calculations, the corresponding infinitely-fine-mesh limits are 0.00340 and 0.00481 for Rayleigh numbers of 5000 and 10 000. From the smooth particle results, using the ideal-gas equation of state, these same specific energies are 0.0030 and 0.0046. Thus the energy errors are no worse than 10% so that velocity errors are of order 5%. Smooth particle kinetic-energy data are also shown in Figures 5.3 and 5.4, again with velocity fields correct to about 5%. Comparisons of the density and temperature contours appear in Figure 5.20. We view the good agreement of the smooth particle and the Navier-Stokes results as completely satisfactory provided that the pressure is low enough to allow for smooth-particle fluid flow.

At higher values of the Rayleigh number the "robust" smooth-particle technique continues to provide solutions when the continuum solutions begin to fluctuate, and can only be obtained with difficulty, if at all. It is this robust aspect of smooth particle applied mechanics, for extreme conditions and at high speeds, which accounts for its popularity in studying a variety of strongly nonequilibrium fluid and solid flows [24].

5.5 Summary

Smooth Particle Applied Mechanics provides a robust and simple approach to reasonably accurate solutions of many continuum problems, including Rayleigh-Bénard instability. It completely avoids grid-tangling and mesh instabilities. Often, a smooth particle solution requires fewer degrees of freedom than does a finite-difference or finite-element approach. Considerably fewer smooth particles are required than atoms in a corresponding molecular dynamics solution. Nevertheless, the smooth particle trajectories are essentially Newtonian trajectories, for particles with mass m, subject to an effective potential function $2Pn^{-2}w(r)$. Accordingly, high-pressure subsonic fluid problems, with $v^2 << c^2$, cannot be reliably solved using this method [25].

Different weighting functions show different types of Raleigh-Bénard rolls and different kinetic energy fluctuations. The hydrodynamic equations cannot tell us the exact or better solution for the given system so that we have no way to tell which one is correct or better than the other. In our computer experiments the Cusp weighting function often solidifies and displays no rolls so that we can certainly conclude that the Cusp function is not appropriate for this problem.

Different weighting functions lead to the different types of particle structure: B spline weighting function makes doubling particle motion from regular square lattice, Lucy function keeps the initial regular lattice type but gradually change it into an irregular shape, Cusp weighting function makes triangular lattice shape which is more stable than the initial regular square lattice.

Rayleigh-Bénard convective turbulent modes occur when the Rayleigh number greatly exceeds the critical Rayleigh number. We calculate the critical Rayleigh number of the system with unit aspect ratio for the dense fluid system. For the dense fluid equation of state we get a three times bigger critical Rayleigh number than that of ideal gas case.

A most interesting thing occurs when different equations of state are applied. Rayleigh-Bénard roll directions are different for dense fluid equation of state and ideal gas equation of state. The ideal gas system alternates roll directions counter clockwise and clockwise during the calculation. As an intermediate step the system shows the four rolls. But these phenomena were not seen in the dense fluid system.

Many authors [20-22] report that the Rayleigh-Benard convection system with a large Rayleigh number is a good source of Chaotic properties. In this range the Smooth

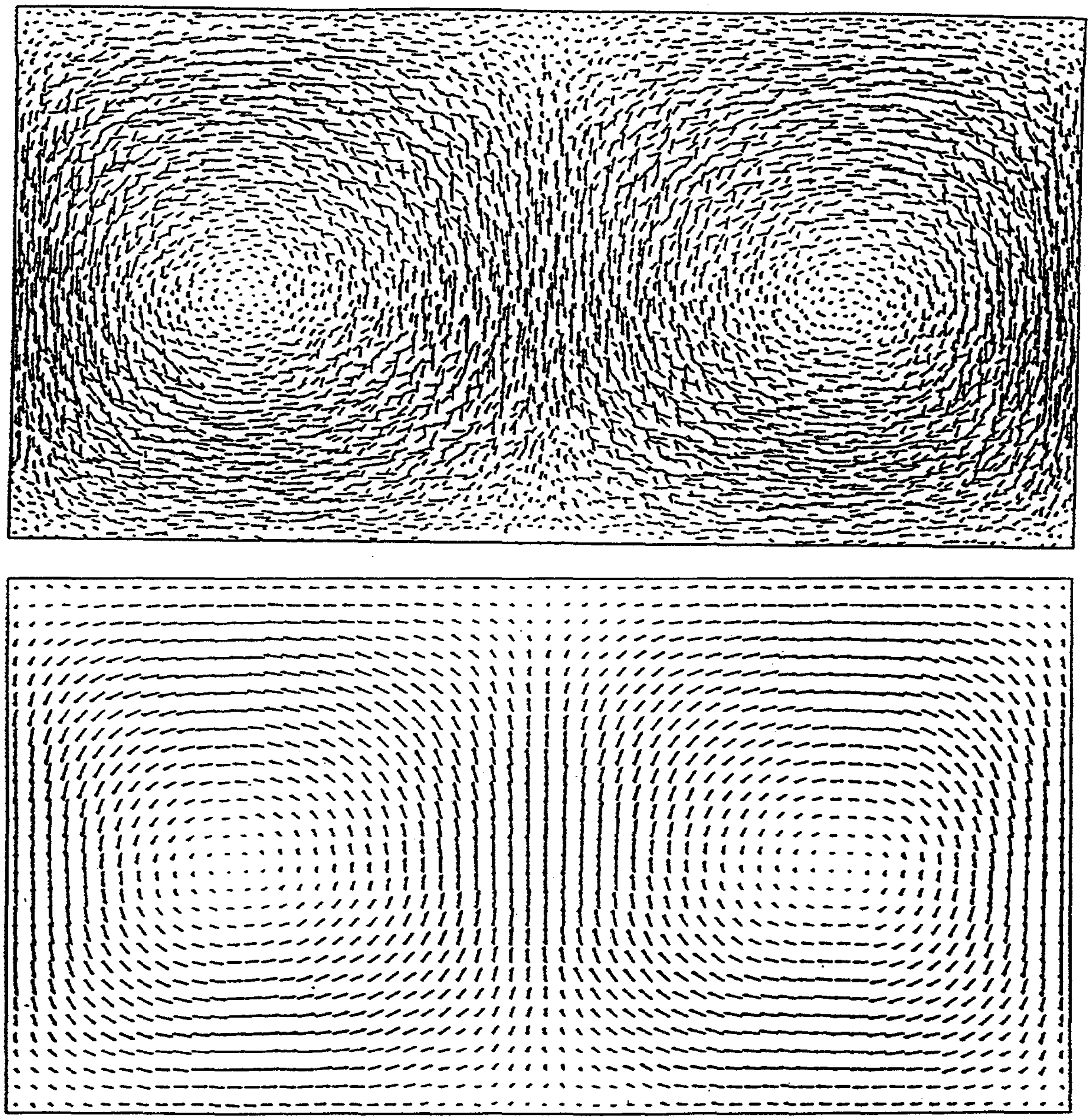

Figure 5.21 Two equivalent views of an ideal-gas simulation with 5000 smoothed particles at a Rayleigh number of 10 000 and with $\eta \equiv k/k_B = 0.5(m\varepsilon)^{1/2}/\sigma$. In the lower view the velocities have been evaluated on an 1800-point square grid using Lucy's weight function with a range of $3\sigma \equiv 3(V/N)^{1/2}$. The distributions correspond to a time of $5000(m\sigma^2/\varepsilon)^{1/2}$.

Particle method can be applied and may therefore also be a good method to study Chaos [15].

The smooth-particle method promises to be of special interest whenever it is desirable to include fluctuations, or to evaluate accurate flow quantities on a regular grid. This latter feature is desirable for the calculation of fast Fourier transforms of field quantities and for automatic rezoning. Figure 5.21 illustrates two velocity-arrow views of the same flow field: first, the individual smooth particle velocities; second, the averaged flow velocities computed at the vertices of a square grid. Because the smooth-particle results we find lie within a few percent of fully-converged solutions of the compressible continuum equations it is economically desirable to develop this method further.

References

[1] I. Goldhirsch, R. B. Pelz, and S. A. Orszag, "Numerical simulation of thermal convection in two-dimensional finite box", Journal of Fluid Mechanics **199** (1989) 1.

[2] G. Veronis, "Large-amplitude Bénard convection", Journal of Fluid Mechanics **26** (1966) 49.

[3] J. W. Deardorff and G. E. Willis, "The effect of two-dimensionality on the suppression of thermal turbulence", Journal of Fluid Mechanics **23** (1965) 337.

[4] D. R. Moore and N. O. Weiss, "Two-dimensional Rayleigh-Bénard convection", Journal of Fluid Mechanics **58** (1973) 289.

[5] L. N. Howard, "Heat transport by turbulent convection", Journal of Fluid Mechanics **17** (1963) 405.

[6] S. Chandrasekhar, **Hydrodynamic and hydromagnetic stability** (Oxford, London, 1961).

[7] D. J. Tritton, **Physical fluid dynamics** (Oxford, London, 1988).

[8] W. G. Hoover, **Computational statistical mechanics** (Elsevier, Amsterdam, 1991).

[9] J. H. Curry, J. R. Herring, J. Loncaric, and S. A. Orszag, "Order and disorder in two- and three-dimensional Bénard convection", Journal of Fluid Mechanics **147** (1984) 1.

[10] J. B. Mclaughlin and S. A. Orszag, "Transition from periodic to chaotic thermal convection", Journal of Fluid Mechanics **122** (1982) 123.

[11] M. Assenheimer and V. Steinberg, "Transition between spiral and target states in Rayleigh-Bénard convection", Nature **367** (1994) 345.

[12] M. Mareschal, M. M. Mansour, A. Puhl, and E. Kestemont, "Molecular dynamics versus hydrodynamics in two-dimensional Rayleigh-Bénard system", Physical Review. Letters **61** (1988) 2550.

[13] T. Watanabe, H. Kaburaki, and M. Yokokawa, "Simulation of two-dimensional Raylegh-Bénard system using the direct simulation monte-carlo method", Physical Review E **49** (1994) 4060.

[14] D. C. Rapaport, "Molecular-dynamics study of Rayleigh-Bénard convection", Physical Review Letters **60** (1988) 2480.

[15] W. G. Hoover, T. G. Pierce, C. G. Hoover, J. O. Shugart, G. M. Stein, and A. L. Edwards, "Molecular dynamics, smoothed-particle applied mechanics, and irreversibility", Computers and Mathematics with Applications **28** (1994) 155.

[16] A. Puhl, M. M. Mansour, and M. Mareschal, "Quantitative comparison of molecular dynamics with hydrodynamics in Rayeligh-Bénard convection", Physical Review A **40**, (1989) 1999.

[17] J. A. Given and E. Clementi, "Molecular dynamics and Rayleigh-Bénard convection", Journal of chemical Physics **90** (1989) 7376.

[18] M. Mareschal and E. Kestemont, "Order and fluctuations in nonequilibrium molecular dynamics simulations of two-dimensional fluids", Journal of Statistical Physics **48** (1987) 1187.

[19] A. Puhl, M. M. Mansour, and M. Mareschal, "Quantitative comparison of molecular dynamics with hydrodynamics in Rayleigh-Bénard convection", Physical Review A **40** (1989) 1999.

[20] P. Colinet and C. J. Legros, "On the Hopf bifurcation occuring in the two-layer Rayleigh-Bénard convective instability", Physics of Fluids **6** (1994) 2631.

[21] T. H. Solomon and J. P. Gollub, "Chaotic particle transport in time-dependent Rayleigh-Bénard convection", Physical Review A **38** (1988) 6280.

[22] P. K. Newton, "Chaos in Rayleigh-Bénard convection with external driving", Physical Review A **37** (1988) 932.

[23] T. Watanabe, H. Kaburaki, and M. Yokokawa, "Simulation of two-dimensional Rayeligh-Bénard system using the direct simulation monte-carlo method", Physical Review E **49**, (1994) 4060.

[24] H. E. Trease, M. J. Fritts, and W. P. Crowley (Editors), **Advances in the Free-Lagrange method**, Lecture Notes in Physics #395 (Springer-Verlag, Berlin, 1991).

[25] O. Kum, W. G. Hoover, and H. A. Posch, "Viscous conducting flows with smooth particle applied mechanics", Physical Review E (to appear, 1995).

Blank page

CHAPTER 6

SHOCK WAVES

Blank page

6.1 Introduction.

Shock phenomena are ubiquitous in high-speed compressible flows and also provide an important source of equation of state information under extreme conditions. Dynamic phenomena of shock waves such as propagation, diffraction, reflection, refraction, and interaction of shock waves have been studied by using experimental, numerical, and theoretical methods for a long time [1-5]. A numerical method for the calculation of shock motion is to solve Navier-Stokes equations numerically. Finite-difference methods [6-10] have been used in the macroscopic regime and Molecular Dynamics simulation has been used on the microscopic scale [11, 12]. The Smooth Particle method is a hybrid so that we can simulate shock dynamics in the macroscopic regime using a transient Molecular Dynamic technique with a moving piston [12-14].

The basic idea of wave propagation is that some recognizable disturbance moves with a finite velocity – through the convective motion of particles. We describe wave formation using a moving piston in Section 6.2. We discuss the forming of shock waves from a simple wave by showing the wave velocity as a function of density in Section 6.3. We also describe the Hugoniot relations for the shock waves and equation of state there.

With the formation of shock waves, the initial distribution of density has a discontinuous step with the value of density behind the discontinuity greater than that ahead. Without dissipation, the discontinuous surface becomes infinitely steep so that a numerical simulation can not continue. To avoid this difficulty, we incorporate dissipation by using heat conduction and viscosity – "artificial" viscosity [15]. We describe two different terms of artificial viscosity in Section 6.4. The Hugoniot equation is used in computing theoretical shock propagation properties. We describe the computational procedure of calculating the Hugoniot relations in Section 6.5. Whenever the propagation wave encounters a second medium, which causes its velocity to change, part of the incident wave is reflected and part of it is transmitted. We discuss this phenomena using a simple numerical example in Section 6.6. Finally in Section 6.7 we describe piston shock generation method using the SPAM algorithm and discuss the results. This shock generation algorithm is directly related to the Richtmyer-Meshkov instability problem, which is discussed in the Chapter 7.

6.2 Wave formation using a piston [3, 4]

Consider the problem of a cylinder filled with gas and with a movable piston at one end. Pushing or pulling the piston with a constant speed generates a compression wave or rarefaction wave. This is because the uniform flow field ahead of the piston is disturbed and the disturbance propagates as a speeding wave.

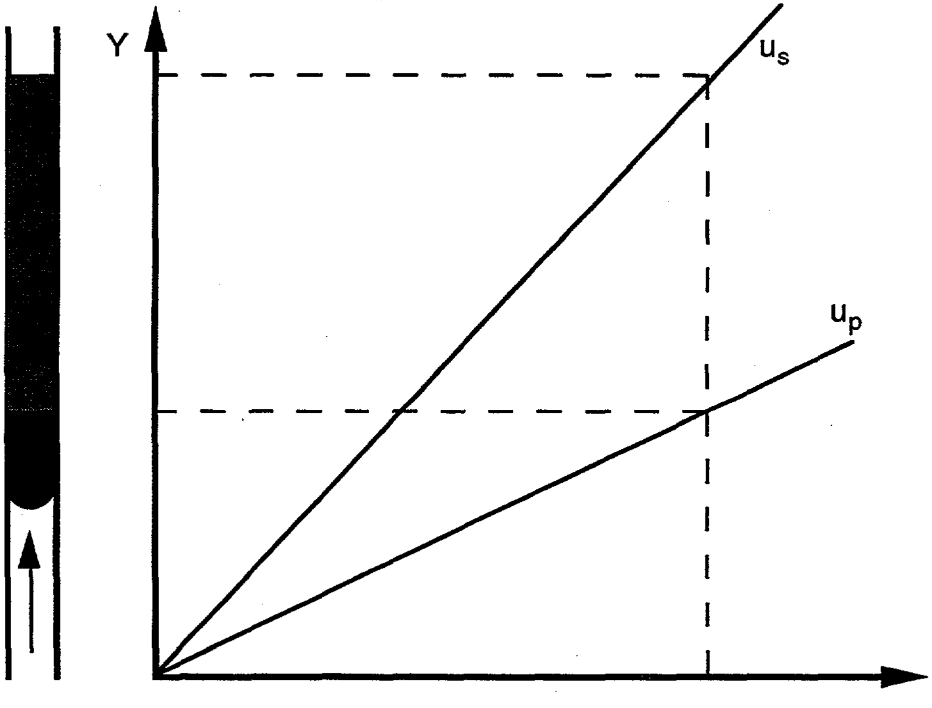

Figure 6.1 Compressive wave formation with a piston. The moving piston generates disturbances which move a steady finite velocity. The wave velocity always exceeds the piston velocity.

Obviously, the compressive wave speed must exceed the piston speed. Figure 6.1 shows the relative positions of the wave and the piston. Any material can propagate sound waves. A sound wave is defined as the small amplitude wave observed as the piston speed approaches zero. It is interesting to see the form of the equations for sound in the hydrodynamic equations. To simplify the problem, consider a one-dimensional isentropic ideal gas problem. The flow is subject to the hydrodynamic equations, continuity equations, Euler equations, and equation of state. In the Eulerian form;

$$\partial\rho/\partial t + \rho\partial u/\partial x + u\partial\rho/\partial x = 0, \tag{1}$$

$$\partial u/\partial t + u\partial u/\partial x + (1/\rho)\partial P/\partial x = 0, \tag{2}$$

$$P = P(\rho), \tag{3}$$

where P, ρ, and u are pressure, density, and flow velocity, respectively. Now assume a small perturbation of pressure and density,

$$P = P_o + P' \ ; \ \rho = \rho_o + \rho' \ ; \ u = u', \tag{4a,b,c}$$

where ' denotes small perturbations, and subscript o denotes undisturbed quantities.

Putting these into the equation (2) and retaining only the first order terms yields,

$$\partial\rho'/\partial t + \rho_o\partial u'/\partial x = 0 \ ; \ \rho_o\partial u'/\partial t + c^2\partial\rho'/\partial x = 0, \tag{5a,b}$$

where $c^2 \equiv \partial P'/\partial\rho' = \partial P/\partial\rho$. c is called the speed of sound because the wave propagation equation is obtained by applying the partial derivative of equation (5a) with respect to time t minus partial derivative of equation (5b) with respect to space x,

$$\partial^2\rho'/\partial^2 t - c^2\partial^2\rho'/\partial^2 x = 0. \tag{6}$$

The solution of this wave equation (6) is,

$$\rho' = f_1(x - ct) + f_2(x + ct), \tag{7}$$

where f_1 and f_2 are arbitrary functions, $x - ct$ = constant corresponds to right traveling waves, $x + ct$ = constant corresponds to left traveling waves. Thus infinitesimal pressure waves propagate with the speed of sound c. The speed of sound c can be written in terms of the partial derivative of pressure P with respect to density ρ at constant entropy,

$$c^2 = (\partial P/\partial \rho)_s. \tag{8}$$

Even though this result is derived from simple assumptions, equation (8) is generally valid for fluids — it is valid even if sound propagates in a non-isotropic flow field. Let us take an example for the ideal isentropic gas equation of state in which pressure is proportional to a power of density. The sound speed can be determined as follows:

$$P = R\rho^\gamma \Rightarrow dP/P = \gamma d\rho/\rho \Rightarrow (\partial P/\partial \rho)_s = \gamma RT\,; \tag{9}$$

$$\therefore\ c^2 = (\partial P/\partial \rho)_s \equiv \gamma RT, \tag{10}$$

where γ ($\equiv c_p/c_v$) is the ratio of specific heats, R is the gas constant, and T is temperature.

6.3 Formation of a shock wave from a simple wave.

To see the change of wave form as a simple wave moves to the right, we need to identify the sign of the expression of propagation velocity of pressure disturbance depending upon density change, $(d/d\rho)[u + c]$. Considering the right-traveling isentropic wave,

$$(d/d\rho)[u + c] = (\gamma + 1)c/(2\rho) > 0, \qquad (11)$$

where we used a constant Riemann Invariant [3] for the right-traveling wave, $[u + \int(c/\rho)d\rho]$. For the right-traveling ideal-gas simple wave, the wave velocity at a higher pressure higher-density point is greater than that at lower pressure. Thus a compression wave steepens as it progresses, with the higher pressure parts of the wave overtaking the lower pressure parts to form a shock wave and contact discontinuity.

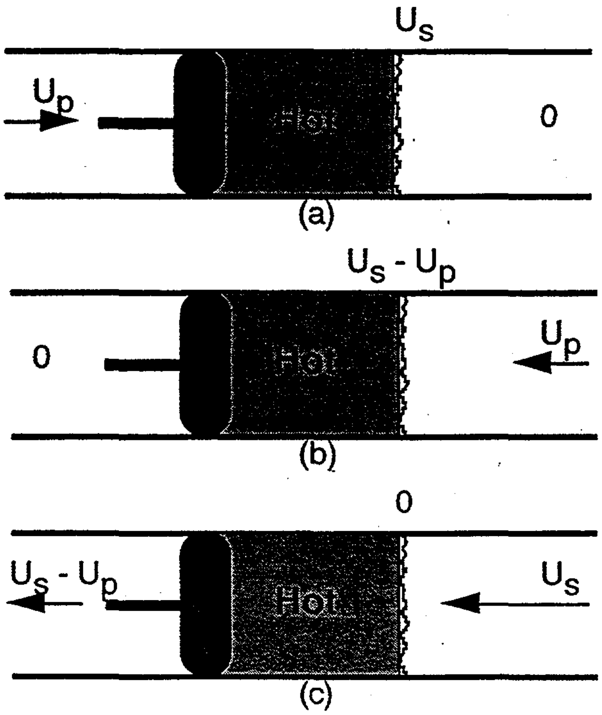

Figure 6.2 Shock wave motion as seen in three coordinate frames: (a) laboratory frame with piston speed u_p and shock wave speed u_S, (b) stagnation frame, in which cold fluid moving at u_p is brought to rest by a rigid wall, (c) shockwave frame, fixed on the wave, in which cold fluid enters at speed u_s and exit at speed $u_s – u_p$. From reference [12].

Only the presence of viscosity and, to a lesser extent, heat conductivity, prevents such a propagating one-dimensional wave from becoming infinitely steep. In the ideal gas shock wave analysis, we use artificial viscosity to moderate the wave. We discuss this idea in detail in the next Section.

The gas behind the shock wave front is usually in a "hot" high-temperature, high-energy compressed state. Ahead of the shock front is a "cold" fluid at a relatively low temperature, energy, and density. The progress generating such a shock wave can be analyzed in the three different reference frames. Figure 6.2 shows the different reference frames: the laboratory frame, with piston speed u_p and shock speed u_s; the stagnation frame, in which cold fluid moving at u_p is brought to rest by a rigid wall; the shock wave frame, fixed on the wave, in which cold fluid enters at speed u_s and exits at speed $u_s - u_p$ [12].

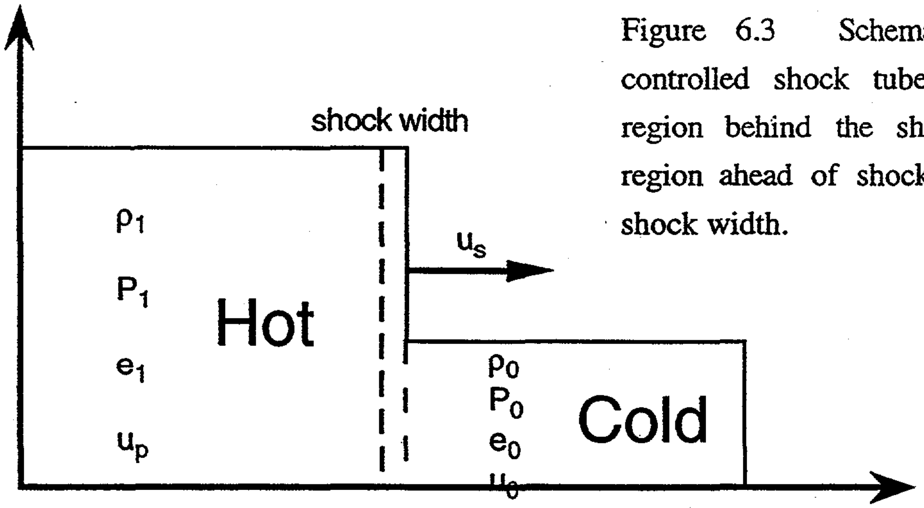

Figure 6.3 Schematic diagram of controlled shock tube, including Hot region behind the shock front, Cold region ahead of shock front, and thin shock width.

In the shock wave frame, the mass, momentum, and energy fluxes are conserved on both sides, hot and cold, and throughout the shock wave. In the controlled tube shown schematically in Figure 6.3 the system is divided by the shock front, whose propagating velocity is u_s. In the hot region, behind the shock front, density is ρ_1, pressure is P_1, energy is e_1 and particle velocity is $u_1 = u_p$. In the cold region ahead of the shock front, density is ρ_o, pressure is P_o, energy is e_o and particle velocity $u_o = 0$. Cold material moves toward the shock front at speed $-u_s$ and hot material moves away from the shock front at speed $u_p - u_s$.

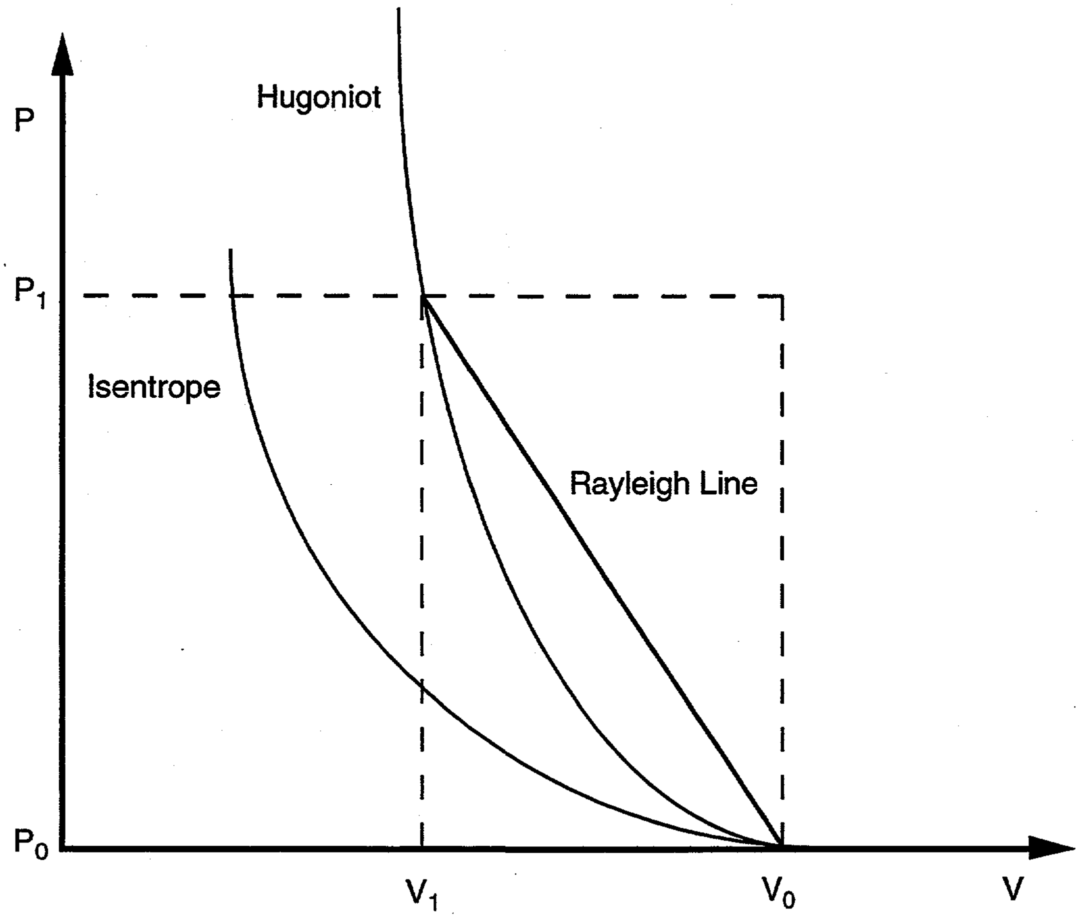

Figure 6.4 Schematic P, V diagram for three curves, Hugoniot, Isentrope, and Rayleigh Line. Material is shocked directly from initial state (P_o, V_o) to final state (P_1, V_1). The slope of the Rayleigh Line determines the shock propagation velocity.

In the shock wave frame, we obtain three equations linking together the thermodynamic properties of the cold and hot equilibrium states, using the notation ρu for the mass flux, $P + \rho u^2$ for the momentum flux, and $\rho u[e + (P/\rho) + (u^2/2)] + Q$ for the energy flux [12]:

$$\rho_1(u_p - u_s) = \rho_o(-u_s) ; \tag{12a}$$

$$P_1 + \rho_1(u_p - u_s)^2 = P_o + \rho_o(-u_s)^2 ; \tag{12b}$$

$$\rho_1 u_p[e_1 + (P_1/\rho_1) + (1/2)(u_p - u_s)^2] = \rho_o u_s[e_o + (P_o/\rho_o) + (1/2)(-u_s)^2]. \tag{12c}$$

By eliminating the two speeds from the three equations the Hugoniot relation for the work done in compression results;

$$\Delta E_{shock} = (P_1 + P_o)(V_o - V_1)/2. \tag{13}$$

The P, V diagram is very useful for clarifying the theoretical relations governing shock waves and the properties of Hugoniot curves. Figure 6.4 shows the P, V diagram for three different curves, Hugoniot, Isentrope, and Rayleigh Line. Material is shocked directly from (P_o, V_o) to (P_1, V_1) as shown in Figure 6.4 By equation (12a), $V_o/V_1 = u_s/(u_s - u_p)$ and eliminating the velocities u_s or $u_s - u_p$ term from equation (12b), the propagation velocity of shock wave is given by

$$u_s{}^2 = V_o{}^2 (P_1 - P_o)/((V_0 - V_1), \tag{14}$$

where the volumes are all "specific" [volume per unit mass]. This velocity can be determined graphically from the slope $(P_1 - P_o)/(V_o - V_1)$, the Rayleigh Line slope. The isentropic curve shown in Figure 6.4 has the initial entropy of the fluid $S_o = S(P_o, V_o)$. The sound wave velocity is calculated from the isentropic state following equation (8) and the Hugoniot curve and Isentrope have the same curvature and slope at the initial state (P_o, V_o). Thus in the limit of a weak shock, when $(P_1 - P_o)/P_o \to 0$, the shock wave is the same as a sound wave: the entropy change approaches zero and the wave velocity coincides with the sound speed,

$$u_s^2 = V_o^2 (P_1 - P_o)/(V_o - V_1) \rightarrow -V_o^2 (\Delta P/\Delta V)_s \rightarrow c^2. \tag{15}$$

In general, the slope of Rayleigh Line is always greater than the tangent to the Hugoniot curve at the initial state (P_o, V_o) so that shock wave velocity is always greater than the sound speed and Hugoniot curve always passes above the isentrope emanating from the initial point.

From equation (13) the specific internal energy increase during the shock compression from (P_o, V_o) to (P_1, V_1) is equal to the area under the trapezoid made by Rayleigh Line. If the fluid is compressed isentropically from (P_o, V_o) to (P_1, V_1), the work performed is equal to the area under the isentrope. This area also gives the increase of internal energy per unit mass,

$$(\Delta E)_s = -\int_{V_o}^{V_1} P\, dV, \tag{16}$$

where the integration is performed for $S = S_o$.

The difference between the two areas corresponds to the energy difference made by the heat increase at fixed final volume V_1 times entropy increase due to shock compression,

$$(\Delta E)_{shock} - (\Delta E)_S = \int_{S_0}^{S_1} T dS = \overline{T}(S_1 - S_0)\, , \tag{17}$$

where $\overline{T}$ is some average temperature lying between the Rayleigh Line and Isentrope. Thus the shock process is not only an adiabatic process without heat flow but is also irreversible. The entropy produced in the shock process is equivalent to an irreversible conversion of work into heat.

If the fluid is initially at rest, the kinetic energy per unit mass acquired by the fluid from the compression is equal to,

$$u_p^2/2 = (u_p - u_s + u_s)^2/2 = (1/2)(P_1 - P_o)/(V_o - V_1). \tag{18}$$

This energy corresponds to the area of the triangle made by the Rayleigh Line and the point (V_o, P_1) so that the total energy, sum of kinetic and internal energy, corresponds to the area of rectangle made by $(P_1 - P_o)(V_o - V_1)$.

6.4 Artificial viscosity [15, 16]

We mentioned in section 6.2 that a compression wave steepens as it progresses, with the higher pressure parts of the wave overtaking the lower pressure parts to form a shock wave and contact surface and becoming infinitely steep without dissipation. To analyze this discontinuity, we solve the nonlinear Hugoniot relations, equations (12a,b,c) and (13). The detailed procedure for computing the Hugoniot relations is explained in the next Section.

It is possible that a shock may develop spontaneously within the fluid. There is no way of telling when and where this might happen, except possibly by constantly monitoring the results of the calculation with an expert eye. To avoid this difficulty, we can incorporate dissipation by using heat conduction or viscosity.

In 1922, Becker [17] studied the effects of heat conduction and viscosity on shock waves. He showed that, when only heat conduction is allowed for, the temperature varies smoothly through the shock layer and that in shocks of strength lesser than a critical value, the pressure and density vary smoothly also; for stronger shocks, the transition of pressure and density is partly smooth and partly discontinuous. When viscosity is allowed for, however, all quantities vary smoothly through the shock region for a shock of any strength. In either case, the thickness of the transition zone is proportional to the coefficient of the dissipative mechanism, so that in the limit of no heat conduction and no viscosity the variations approach the discontinuous Hugoniot ones. Becker also showed that with ordinary viscosity, in which the stress is proportional to the shear rate, and which is therefore represented by linear terms in differential equations, the thickness of transition layer varies with the shock strength, approaching zero for a very strong shock and infinity for a very weak shock.

These problems were avoided in numerical simulations by Von Neumann and Richtmyer. They introduced a purely artificial dissipative mechanism of strength and form such that the shock transition is smoothed over three or four spatial zones [15]. Their quadratic artificial viscosity term has a similar effect. When we use only a quadratic term for shock dissipation, we find enhanced fluctuations around the shock discontinuity. To avoid these fluctuations we included an additional linear term proportional to the velocity gradient:

$$q = \begin{cases} \alpha\rho h^2(\nabla\cdot u)^2 - \beta\rho hc(\nabla\cdot u), & (\nabla\cdot u) < 0 \\ 0, & (\nabla\cdot u) > 0, \end{cases} \tag{19}$$

where α and β are given constants, ρ is density, u is velocity, c is sound speed, h is of the order of the smoothing length. In SPAM, we calculate $\nabla\cdot u$ with the same algorithm as that of the viscous stress tensor, using equation (1a) in Chapter 3.

6.5 Computing the Hugoniot Relations

Equations (12a,b,c) relating the flow variables on each side of the discontinuity form a system of three equations with six variables u_s, ρ_o, P_o, u_p, ρ_1, and P_1 for the ideal gas equation of state. It is assumed that thermodynamic equation of state, a function of (P, ρ), is known and the value of a parameter describing the strength of shock wave is known, for example, the density behind the wave front ρ_1 or the velocity of the "piston" creating the wave u_p. The computation is not explicit, but rather implicit, and the procedure is the following (with assumption of knowledge of shocked material density ρ_1); first calculate the specific volume of shocked material ($1/\rho_1$), second calculate the specific volume difference ΔV ($\equiv V_o - V_1$), third calculate the shocked pressure and energy. The third procedure is done implicitly to satisfy the Hugoniot equation (13) and the given thermodynamic equation of state at once: first pressure is assumed and a new energy is calculated using equation (13); then a new pressure is calculated using the given equation of state, $P(\rho, T)$ and $e(\rho, T)$. This process is iterated until the numerical value of the new pressure is equal to the old one.

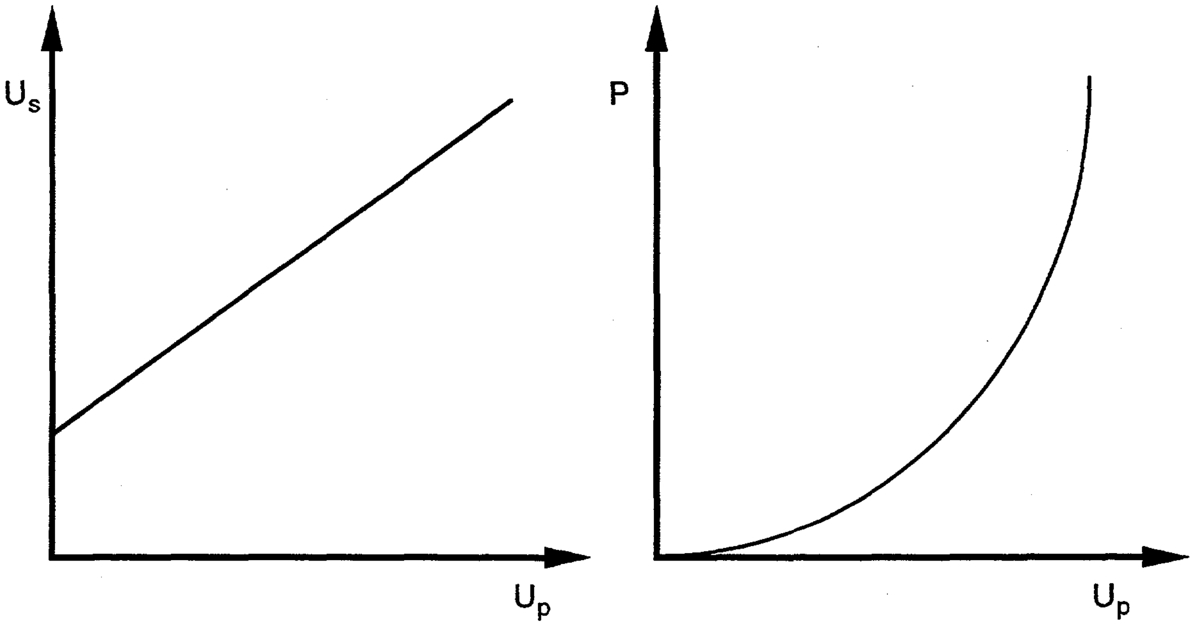

(a) (b)

Figure 6.5 The relations linking pressure P, shock speed u_s, and piston velocity u_p. (a) Shock wave velocity as a function of piston or particle velocity. The shock speed at zero piston velocity corresponds to the sound velocity of the material. (b) Shock pressure as a function of piston or particle velocity.

Finally we calculate the shock velocity and particle velocity of the shocked material from the specific volume difference, pressure difference, and piston velocity. The strength of the shock wave can be described by specifying either of the two speeds u_s and u_p, or any of variables identifying the final thermodynamic states: P_1, V_1, and e_1. Thus the three variables related to the shock, pressure P, shock speed u_s, and particle velocity u_p are not independent of each other. They satisfy a functional relation according to the equation of state.

Figure 6.5 (a) shows a shock speed u_s versus particle speed u_p relation. In this diagram, shock velocity at zero particle velocity corresponds to the sound velocity. Figure 6.5 (b) shows a pressure P versus particle velocity u_p relation. Figure 6.5 (a) suggests that a shock wave can be generated at any speed of piston velocity.

6.6 A simple reflected shock wave [18, 19]

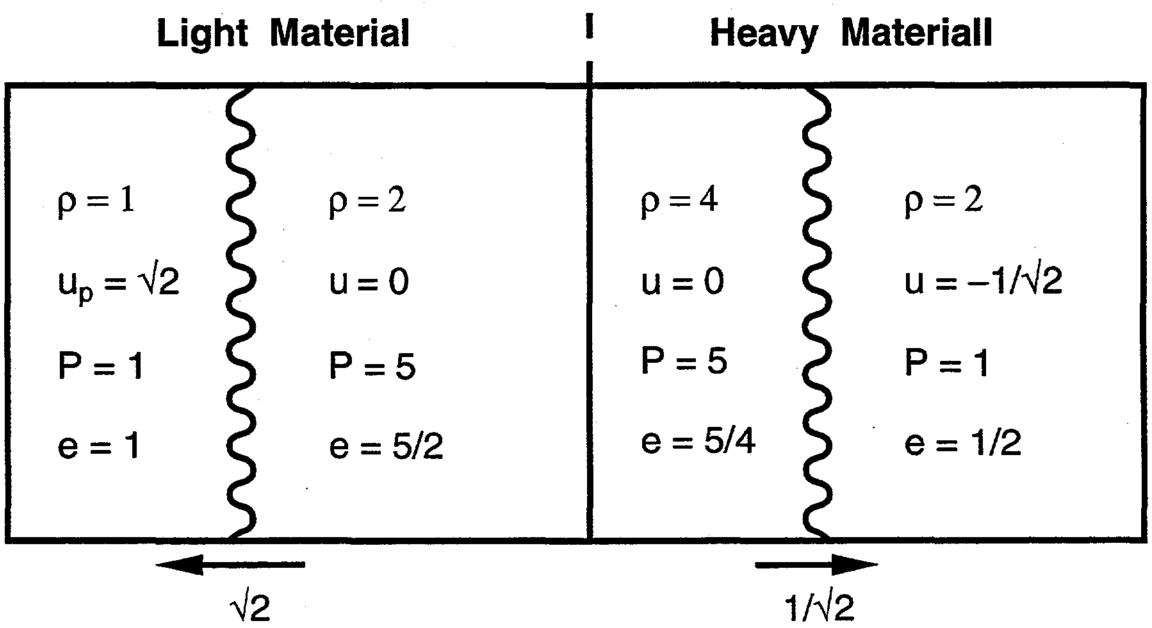

Figure 6.6 Numerical example of a controlled shock tube of Light material hitting the Heavy material generating transmitted and reflective shock waves. The equation of state is $P = \rho e$.

So far we considered propagating shock waves. When a propagating shock wave meets a contact discontinuity, [for example, materials with different thermodynamic properties, a rigid wall, a force free wall], part of the incident wave is reflected and part of it is transmitted. This situation is called the Riemann problem.

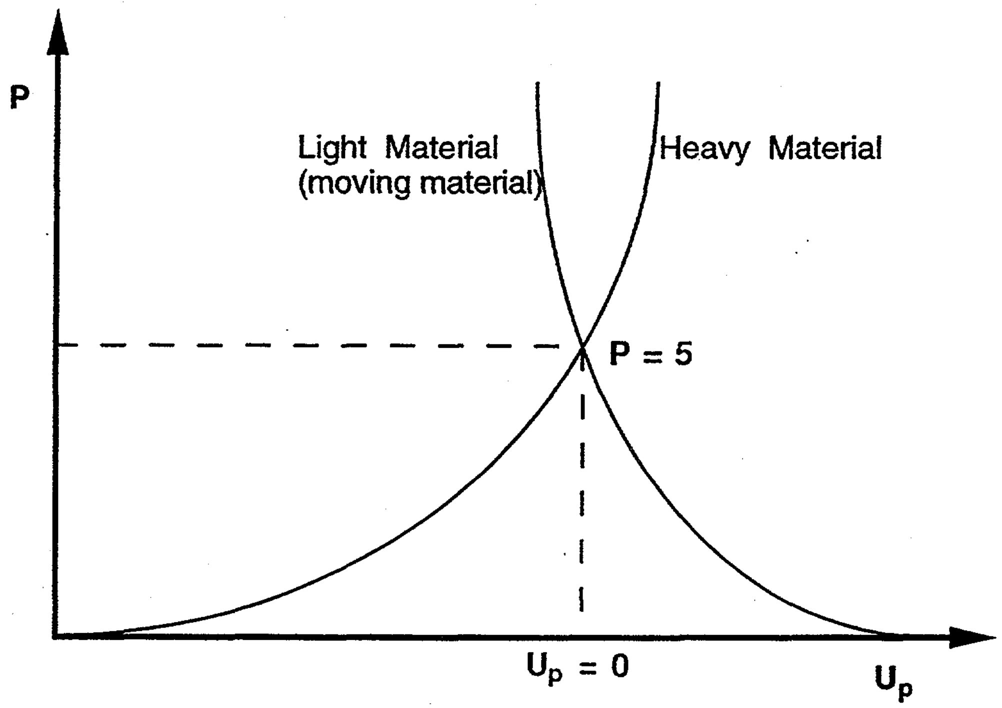

Figure 6.7 Shock interface matching condition. The shock wave is generated by the Light material (moving material) hitting the Heavy material.

The actual phenomena of the reflected and transmitted wave are very complicated, depending upon the thermodynamic properties of the reflecting material. The analysis of such experiments is based on the fundamental facts of shock wave physics. Shock pressure and mass velocity are obviously continuous across any interface between two materials, thus satisfying a shock impedance $[\rho_o u_s]$ matching principle according to the relation, $[\Delta P = (\rho_o u_s) u_p]$, from discontinuity equations (12a) and (12b). We illustrate this principle by taking a simple example: Figure 6.6 shows this numerical example with a controlled shock tube of Light material hitting a Heavy material with their physical parameter values.

To get a graphical solution, we use the Hugoniot curve, pressure versus particle velocity as shown in Figure 6.7. Computing the Riemann problem using the Hugoniot relations uses the discontinuity equations (12a, b, c) and shock matching condition shown in Figure 6.7 at each contact interface.

6.7 Piston shock generation using the SPAM algorithm

A transient method, which has been used in molecular dynamics [12,13], can be used in SPAM to generate a shock wave. Figure 6.8 shows the transient method used in molecular dynamics from reference [12].

This Figure shows two space dimensions with four periodic boundary conditions. Two boundaries incorporate time-dependent boundary conditions.

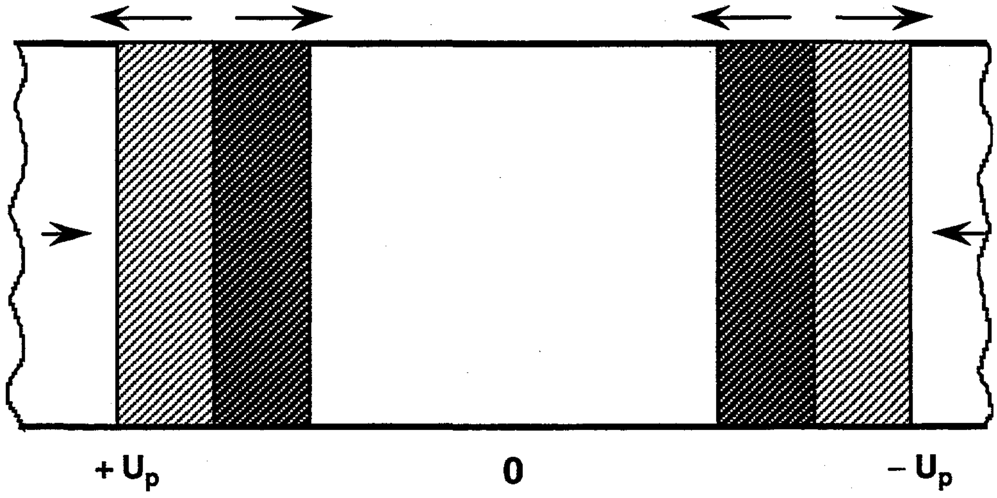

Figure 6.8 Special boundary conditions which produce two symmetric shock waves at each boundary linking the system to a periodic images. Shock velocities are shown at the top in the laboratory frame. Laboratory frame velocities are shown at the base. The Hot shocked regions are shaded. From reference [12].

Initially the y coordinates for all particles in the system lie in the range from –L(0)/2 to +L(0)/2 :

$$-L(0)/2 < \{y\} < L(0)/2. \qquad (20)$$

Instead of using periodic boundary conditions for four boundaries in two dimensional problem, we tested two different models here: (i) a system with four reflected boundary conditions with image particles, and (ii) a system with two periodic boundaries in lateral directions and two reflective boundaries in horizontal directions with image particles. In both cases we move a piston with velocity u_p from lower boundary toward the upper boundary in the y direction. For time t, the lower boundary location in y direction is

$$y_L(t) = -L(0)/2 + u_p t. \tag{21}$$

We also assumed the same velocities as the piston velocity (particle velocity) for the particles within one interaction range of the moving boundary. The effect of such a time dependent boundary condition is to compress the system using a piston. A shock wave generated near the lower end in y-direction propagates upward at the shock speed u_s. For the pure progressing shock analysis, the calculation is completed when the shock front reaches the upper end in y coordinate. Figure 6.9 is a panoramic view of the shock wave at regular time intervals. During the period of steady propagation, Figure 6.10 shows the propagating shock wave properties. In this calculation, we use the ideal gas equation of state with 1500 (10x150) particles and the B-spline weighting function with smoothing length h ($\equiv 2.5$). The physical variables, density, pressure, energy, and particle velocity of the shocked material, are calculated by a binning method. The bin size is equal to the one interaction range. Each point represents the average value in a bin. In this Figure, the particle velocity (piston velocity) is $\sqrt{2}$, reduced initial density is 1, initial energy is 1, initial pressure is 1 using ideal gas equation of state. The shock velocity is $2\sqrt{2}$. The shocked values, density, velocity, energy, and pressure, have small fluctuations less than 1 % error comparing with the values calculated by Hugoniot relation.

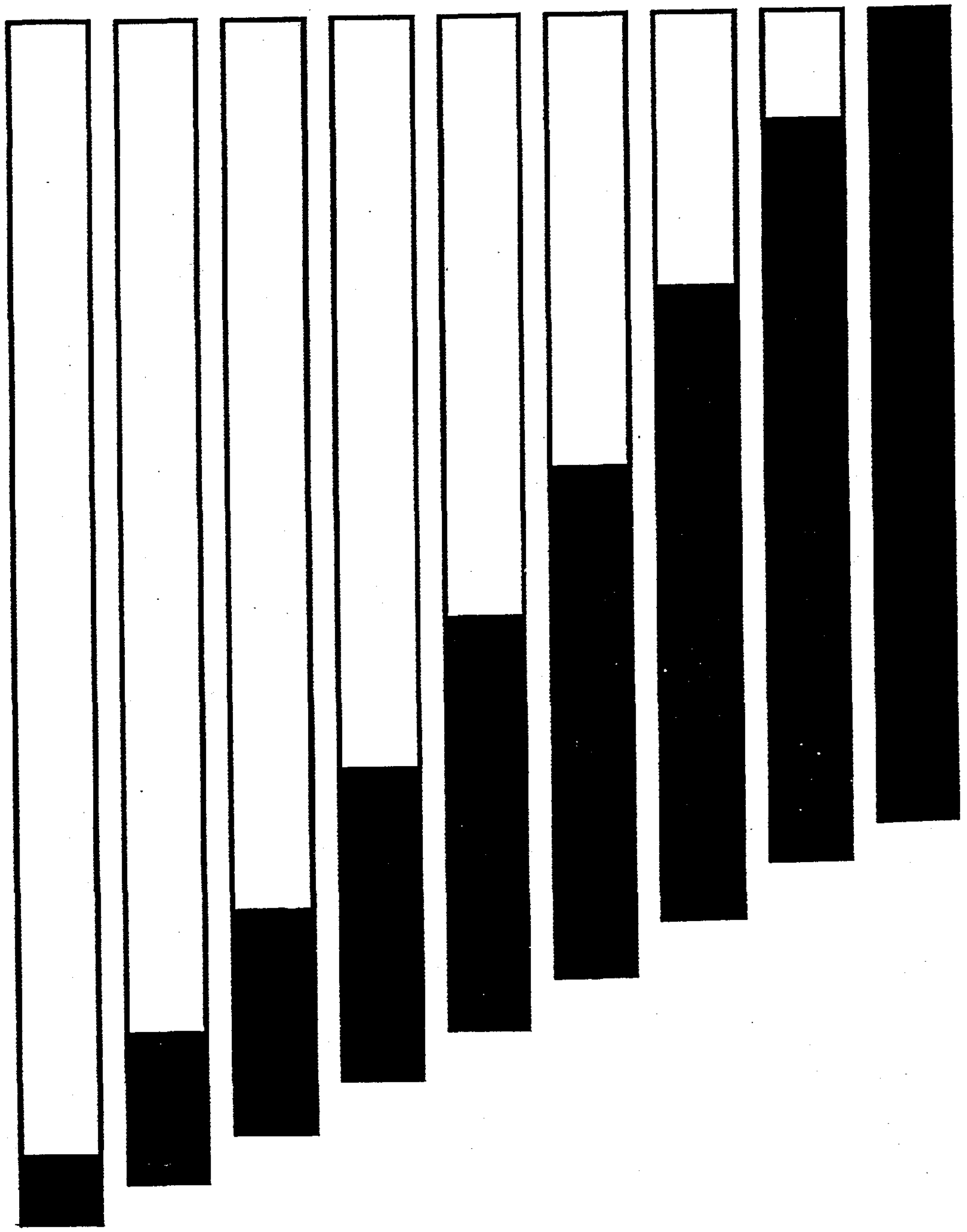

Figure 6.9 Propagation of shock waves generated by an upward moving piston. Hot regions are marked black, and cold regions white. Initially the velocities of particles within one interaction range from moving piston are given the same velocity as that of piston. Steady shock waves propagate at constant speed. 1500 (10x150) particles are involved. Initial reduced density, pressure, and energy are all unity. Particle velocity (piston velocity) is $\sqrt{2}$ and shock velocity is $2\sqrt{2}$. The ideal gas equation of state ($P = \rho e$) is used.

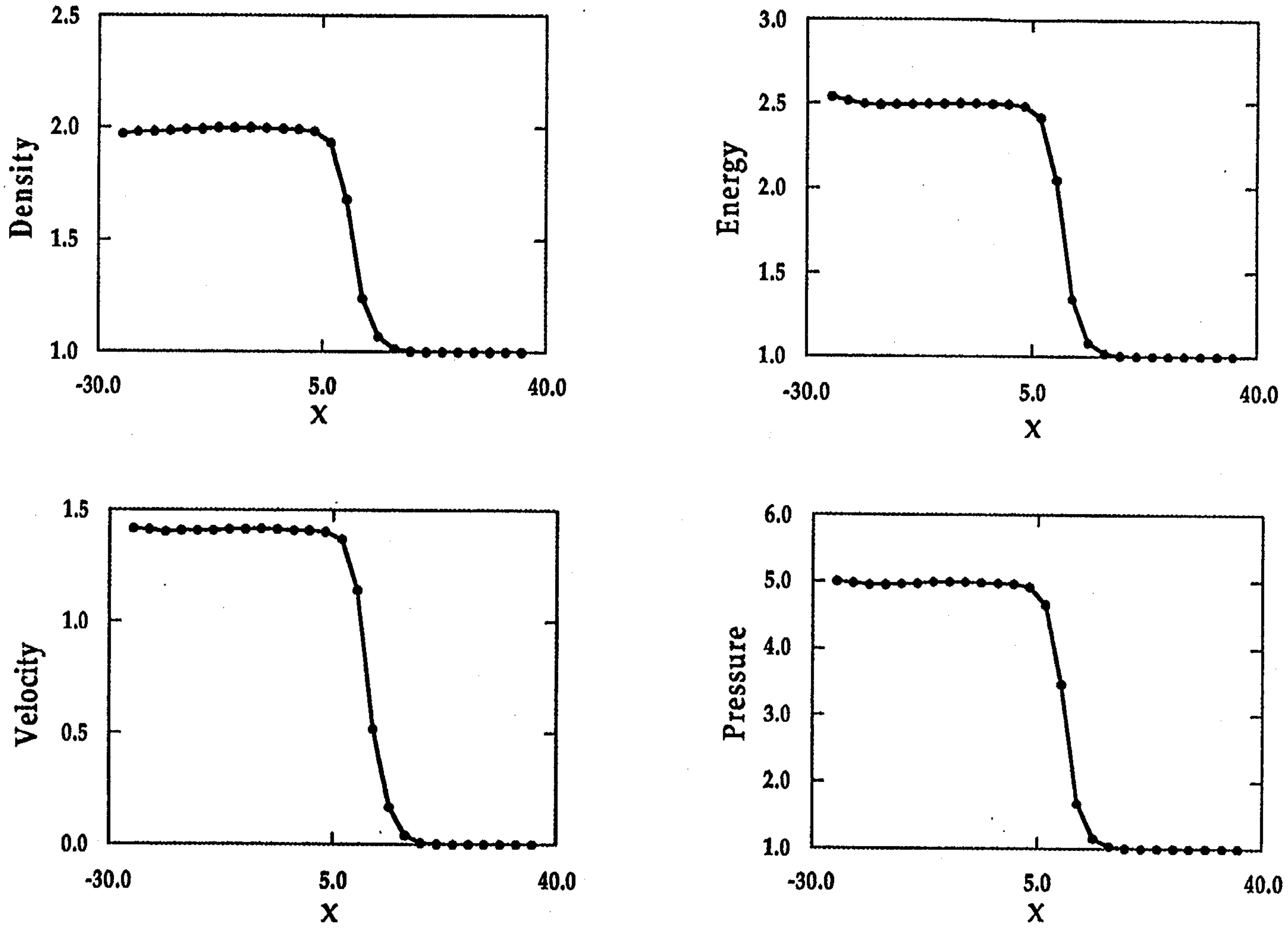

Figure 6.10 Propagating shock wave properties corresponding to Figure 6.9. 1500 (10x150) particles with an ideal gas equation of state were used.

6.8 Summary

Shock waves can be analyzed in three different coordinate frames, the laboratory frame, the stagnation frame, the shock wave frame. In the shock wave frame, the mass, momentum, and energy fluxes are conserved on both sides, hot and cold materials throughout the shock wave. From the mass, momentum, and energy discontinuity equations, the Hugoniot (P, V, E) relation is derived. We can compute the propagation properties of the shock waves using Hugoniot relations or fluid dynamic simulations. We described the two methods. For the fluid dynamic simulation we used the smooth particle method.

In SPAM simulations we used artificial viscosity terms, a linear term for preventing fluctuations and a quadratic term for avoiding numerical difficulties from the discontinuous surface. We generated the shock waves by a transient method which has been used in Molecular Dynamics. The propagating properties of shock waves generated by SPAM algorithm shows less than a 1 % error compared to the exact values calculated from the Hugoniot relations. In this simulation, we used a reflective horizontal boundaries and periodic lateral boundaries. We also simulated a generalized Riemann problem for two different density materials, a prototype of the Richtmyer-Meshkov instability problem. For the Light/Heavy or Heavy/Light materials simulations, SPAM shows accurate results with no greater than 5 % error.

References

[1] W. F. Noh, **Numerical methods in hydrodynamic calculations**, UCRL-52112 (1976).

[2] W. J. Nellis, **Shock compression of solids: Tutorial**, UCRL-TC-103276 (1990).

[3] W. D. Hayes and R. F. Probstein, editors, **Physics of shock waves and high-temperature hydrodynamic phenomena** volume **I & II** (Academic Press, New York, 1966).

[4] Z. Han and X. Yin, **Shock dynamics** (Kluwer Academic, Beijing, 1993).

[5] W. J. Nellis and A. C. Mitchell, "Shock compression of liquid argon, nitrogen, and oxygen to 90 Gpa (900 Kbar)", Journal of Chemical Physics **73** (1980) 6137.

[6] G. B. Whitham, **Linear and nonlinear waves** (John Wiley & sons, New York, 1974).

[7] E. S. Oran and P. J. Boris, **Numerical simulation of reactive flow** (Elsevier Science Publishing, New York, 1987).

[8] W. G. Noh, "Errors for calculations of strong shock using an artificial viscosity and an artificial heat flux", Journal of Computational Physics **72** (1978) 78.

[9] G. Hedstrom, G. Rodrigue, M. Berger, and J. Oliger, "Adaptive mesh refinement for 1-dimensional gas dynamics", Scientific Computing (1983) 43.

[10] R. J. Levesque, **Numerical methods for conservation laws** (Birkhä ser Verlag, Basel, 1992).

[11] M. Mareschal and B. L. Holian, editors, **Microscopic simulations of complex hydrodynamic phenomena**, NATO ASI Series **292** (Plenum Press, New York, 1992).

[12] W. G. Hoover, **Computational statistical mechanics** (Elsevier, Amsterdam, 1991).

[13] B. L. Holian, W. G. Hoover, B. Moran, and G. K. Straub, "Shock-wave structure via nonequilibrium molecular dynamics and Navier-Stokes continuum mechanics", Physical Review A **22** (1980) 2798; H. M. Mott-Smith, "The solution of the Boltzmann equation for a shock wave", Physical Review, **82** (1951) 885.

[14] J. J. Monaghan and R. A. Gingold, "Shock simulation by the particle method SPH, Journal of Computational Physics **52** (1983) 374.

[15] J. VonNeumann and R. D. Richtmyer, "A method for numerical calculation of hydrodynamic shocks", Journal of Applied Physics **21** (1950) 232.

[16] R. D. Richtmyer and K. W. Morton, **Difference methods for initial-value problems** (Wiley-Interscience, New York, 1967).

[17] R. Becker, "Stosswelle und detonation", Z. Physik, **8** (1922) 321 in reference [16].

[18] L. F. Henderson, "On the refraction of shock waves", Journal of Fluid Mechanics **198** (1989) 365.

[19] L. F. Henderson, P. Colella, and E. G. Puckett, "On the refraction of shock waves at a slow - fast gas interface", Journal of Fluid Mechanics **224** (1991) 1.

Blank page

CHAPTER 7

RICHTMYER-MESHKOV INSTABILITY

Blank page

7.1 Introduction

Instability growth plays an important role in understanding the relative fluid motion of two contiguous heterogeneous fluids of different densities accelerated toward each other [1-3]. In 1950, Taylor analyzed the instability of an interface, between two different density fluids, and perpendicular to a gravitational field [4-7]. He solved the problem in which the density difference between the materials separated by the interface was small. He found that the interface was unstable to small perturbations if the direction of the acceleration normal to the interface coincides with that of density gradient. This obvious instability is well known. It is called Rayleigh-Taylor instability.

In 1960, Richtmyer extended Taylor's analysis of gravitational acceleration to treat the shock acceleration of such an interface. In 1969, Meshkov confirmed Richtmyer's analysis with his shock tube experiments. Since then, the shock-instability problem became known as Richtmyer-Meshkov instability and become a subject of research in its own right [8-11].

The Richtmyer-Meshkov instability can be considered as a limit of the Rayleigh-Taylor instability when the acceleration acts for almost zero time but with the magnitude of the acceleration sufficiently large that a finite amount of momentum is transferred to the fluid. This instability problem is important for basic physics, for understanding supernovae, and technological applications. Applications include supersonic and hypersonic combustion as well as inertial confinement fusion [10]. There have been many experimental [12] and numerical studies of Richtmyer-Meshkov instability.

Experiments can be divided into two different types: shock tube and laser [11]. Shock tube experiments have been more numerous than laser experiments [13, 14]. Experiments in which thin solid plates with a perturbation machined in the driven surface were accelerated by gaseous detonation products from a plane wave generator were performed by Barnes *et al* [15] at Los Alamos. The numerical simulation of acceleration instability in elastic-plastic solids was preformed by J. W. Swegle and A. C. Robinson [16]. The major difficulty with fluid phases is in making a sharp interface perturbation between two fluids. Most experiments using a gasous phase employ a membrane to control the interface perturbation. For small amplitude perturbations, experimental results confirm the Richtmyer-Meshkov results: the amplitude grows linearly with time. Membrane errors in the measured amplitude are typically about 10 %. For gases without a membrane, the interface is smooth. This problem was studied experimentally by Brouillette [13] in 1989.

Many types of numerical simulations have been carried out [12]: two-dimensional calculations using purely Eulerian methods (Besnard, Wehner); Eulerian meshes with interface tracking; Eulerian meshes with adaptive mesh refinement (Rupert); arbitrary Lagrangian Eulerian meshes (Rauenzahn, Griswold); semi-Lagrangian meshes with interface tracking (Cowperthwaite); and front-tracking methods (Glimm). Some three-dimensional calculations using Eulerian codes have been carried out by Cowperthwaite and Wehner. All of the numerical calculations assume inviscid fluids. The meshes are defined so as to ensure a good resolution of the initial wavelengths. However, as a perturbation becomes nonlinear and finally turbulent, smaller scales develop. Some cannot be resolved. Simulations show that ten times the Kolmogorov eddy size, which is defined in Section 8.2, is possible for numerical resolution. The maximum size of resolved problems is obviously limited partly by computer memory size and principally by execution speed.

Possible sources of quantitative differences between calculations and experiments are membrane and boundary layer effects. Both are hard to simulate in calculations. These aspects of the problem were studied by Benjamen and Cloutman but the puzzle remains unsolved [12]. For small amplitude perturbations, there has been theoretical research [17, 18] confirmed by numerical results. Progress has been made, particularly, in the computation of single-wavelength perturbations. Although much has been accomplished in the past two decades, there is still room for exciting research into several aspects of the Richtmyer-Meshkov mixing problem, such as the nonlinear behavior of perturbation growth.

Here we present results calculated using the SPAM algorithm described in Chapters 2 and 3. We have three reasons to apply SPAM to this problem: first, SPAM is a purely Lagrangian method, without a mesh, an advantage in dealing with any turbulent problem; second, the structure of the SPAM algorithm is very simple. We can easily add any necessary physical model to this algorithm; third, SPAM can begin with a smooth density range similar to the real gas experiment without needing the membrane considered by Broullette [14]. The smoothing function and its range can also be controlled.

In the next section, we review the simple theory explaining amplitude growth. We describe our numerical model in Section 7.3. Finally, we report our results and discuss them in Section 7.4. Section 7.5 includes a summary.

7.2 Review of Simple Theories

A simplified model theory cannot explain every important aspect of a full fluid dynamical instability analysis. But it can give us some valuable insight into the concepts defining a problem. With the assumption of a small perturbation, Taylor characterized the instability of a density interface in a gravitational field. He assumed a small perturbation so that he could apply a linear perturbation theory. He then found the growth rate for the interface perturbation, a(t):

$$d^2a(t)/dt^2 = kgA_ta(t), \qquad (1)$$

k ($\equiv 2\pi/\lambda$), is the horizontal wave number of perturbation, λ is the wave length, and a(t) is a perturbation length at time t. A_t is the Atwood number, $[(\rho_2 - \rho_1)/(\rho_2 + \rho_1)]$, and g is gravity. The Atwood number A_t is positive here to cause the instability. The perturbation grows exponentially with time.

Richtmyer proposed replacing the constant acceleration g by an impulsive one g = [u]δ(t), where δ(t) is the Dirac delta function. Replacing g in this way and integrating the second order equation once with respect to time, the growth rate of perturbation in impulsive acceleration becomes,

$$da(t)/dt = k[u]A_t a_o, \tag{2}$$

where a_o is the amplitude of perturbed interface before shock passes , [u] is the change of interface velocity induced by the shock. The Atwood number A_t can now be positive, zero, or negative. In the linear theory, this equation is valid as long as $a(t) << \lambda$, i.e. for small enough $t << [\lambda^2/(a_o[u])]$. Figure 7.1 shows two schematic shape of solutions growing for the arbitrary constant.

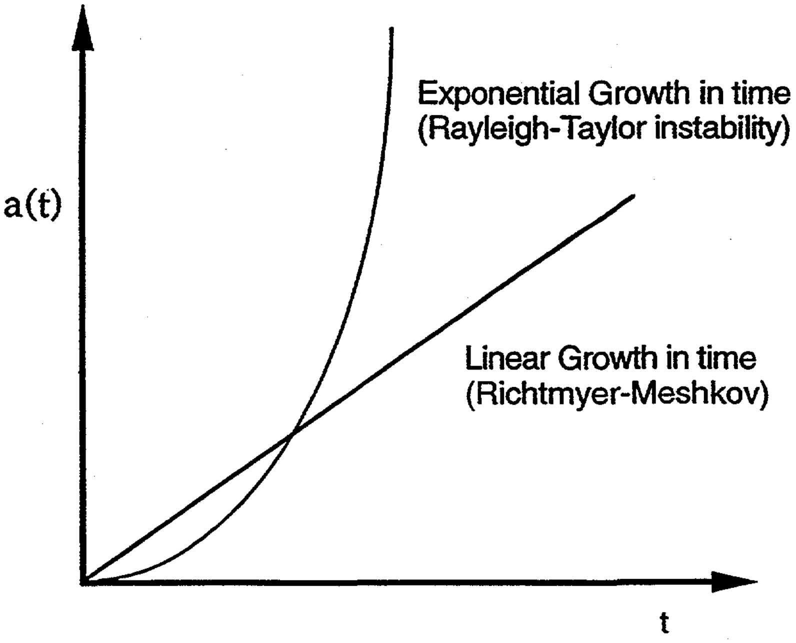

Figure 7.1 Schematic diagram for the solutions of equations (1) (Rayleigh-Taylor instability) and (2) (Richtmyer-Meshkov instability).

For the Light/Heavy configuration in which a shock wave is generated in the Light material and propagates into the Heavy material, $A_t > 0$ and the perturbation increases in amplitude from the start. For the Heavy/Light configuration in which a shock wave is generated in the Heavy material and propagates into Light material, $A_t < 0$ and the perturbation changes phase first and then grows — so called "phase inversion" [7-9]. For $A_t = 0$, there is no perturbation growth — so called "freezing out" [9].

Richtmyer solved the linear problem numerically and found agreement within 10 % with the impulsive acceleration formula, equation (2), provided a_o' and A_t', the post-shock amplitude (both material shocked) and Atwood ratio, were used respectively. His corrected equation is,

$$da(t)/dt = k[u]A_t'a_o', \tag{3}$$

where the primes denote the use of post-shock properties.

Although shock refraction at an interface between two fluids of different densities is an inherently compressible process, equation (3) is usually considered to describe incompressible materials because the perturbation velocities are assumed small with respect to the local speed of sound.

Even though this equation explains the basic concepts behind the Richtmyer-Meshkov instability, it does not give quantitative agreement with the experiments [18]. Subsequent theories tried to narrow the gap, for example, K. O. Mikaelian's [17, 19] surface tension and viscosity effects improved the results. Dr. Mikaelian has studied these instability problems for more than 10 years, [17, 19] at the Lawrence Livermore National Laboratory.

Here we wish to modify the above theory to explain the experimental results of a smoothed interface without membrane because SPAM algorithm automatically smooths the interface density. Figure 7.2 shows a schematic smoothed interface of two fluids. M.

Broullette and B. Sturtevant [14] did shock tube experiments without a membrane but with a smoothing density variation on the interface. They believe the smoothing variation caused a lower growth rate. They used a smoothing parameter and modified Richtmyer's equation (3). With a growth reduction parameter ψ in their notation, they used the following growth rate equation for the Rayleigh-Taylor instability problem,

$$d^2a(t)/dt^2 = (kgA_t/\psi)a(t), \qquad (4)$$

where the growth reduction parameter ψ is a function of time if the thickness of the smoothing interface increases by molecular diffusion, for example, while the perturbation on the interface grows in amplitude. In equation (4), $\psi > 1$ for a continuous interface and $\psi = 1$ for a discontinuous interface. In the analysis of their experimental results, they found a linear relation linking the ratio of the smoothed interface length to the wave length.

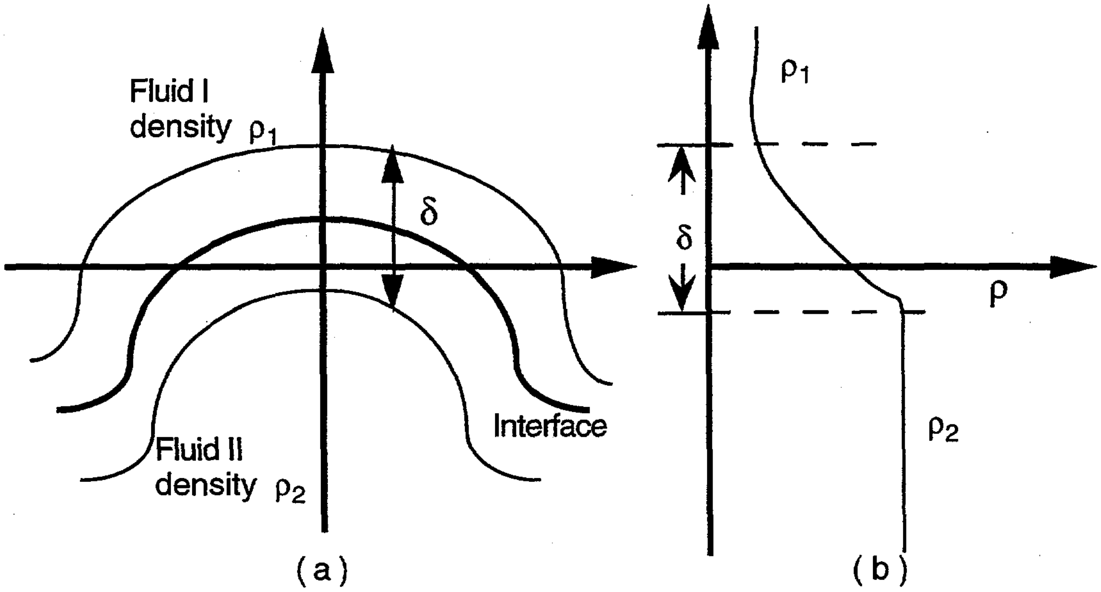

Figure 7.2 Smooth interface of two fluids: (a) sinusoidal perturbation on interface, (b) vertical density profile. A discontinuous interface would have a thickness δ.

Applying the same procedure to Richtmyer's approach, replacing the constant acceleration by an impulsive acceleration, $g = [u]\delta(t)$, where $\delta(t)$ is Dirac delta function, in the growth rate, and integrating the equation, the interface growth rate becomes:

$$da(t)/dt = (k[u]A_t'/\psi)a_o'. \qquad (5)$$

For the continuous interface they used post-shock properties for Atwood ratio and initial amplitude which are specified by Richtmyer for the discontinuous interface. They assumed the reduction factor ψ is a function of average interface smoothing thickness (average of pre- and post shock) and average Atwood ratio (average of pre- and post-shock). They found that a linear form of function ψ with one adjustable constant with respect to average interface thickness and average Atwood number, can explain their experimental results. Intuitively, this is a good idea because smoothing the interface density decreases the growth rate. In our SPAM simulation, we expect to reproduce this type of phenomena. In the next Section we describe our numerical models.

7.3 Numerical simulation

Eulerian and Lagrangian finite difference methods have known difficulties in analyzing this instability problem. The Eulerian method needs a refined mesh size for good resolution as well as an interface boundary tracking technique to follow the flow interface regions. These difficulties require considerable computer memory. On the other hand, the Lagrangian method has none of these difficulties. Instead the Lagrangian method is limited, in the phase reversal problem, by mesh distortion. In the Heavy/Light material configuration, we have a phase reversal problem so that Lagrangian method does not apply well to this problem. The no-slip boundary condition in the interface, which is used in finite difference Lagrangian scheme, also leads to large shearing distortions in the mesh since no-slip boundary condition on the interface creates a viscous flow in that region.

As we described the theory and numerical method in Chapters II and III, SPAM is a candidate numerical method free of all the above-mentioned numerical difficulties. This motivates our interest in this problem. SPAM is a Lagrangian method, but without a mesh so that there is no mesh tangling for large deformation. SPAM needs no boundary tracking technique because it is purely Lagrangian.

We calculate each particle's density as a weighted sum over all near-neighbor particles,

$$\rho(r) = \sum m_j \, w(r-r_j; h),$$ equation (16a) in Chapter 2.

To make two different density materials in one system, we assign two different masses to each region of materials. With this calculation, we have a smooth interface between two materials. This smooth interface resembles the experimental situation considered by Broullette. The same smoothing length in the two different density regions leads to a relatively fine mesh in the high density region since we have the same number of near-neighbor particles in the same volume but different densities.

We use two similar interface perturbation schemes to generate the interface perturbation:

$$a = a_o \cos[(2\pi nx)/L_x] \quad \text{or} \quad a = a_o \sin[(2\pi nx)/L_x], \tag{6a,b}$$

where a_o is the initial perturbation amplitude, L_x is length of x-coordinate, n is the number of waves imposed on the initial setup. The impulsive shock acceleration is applied in the y-direction so that a is the perturbation amplitude in this direction after the shock wave or reshock wave passes.

We use a *periodic* boundary condition in the x-direction to eliminate edge effects. But we use a reflective boundary condition in the y-direction with image boundary particles which compensate for the density decrease near the boundary region for the multiple reflected shocks. Figure 7.3 shows a schematic configuration of the simulation.

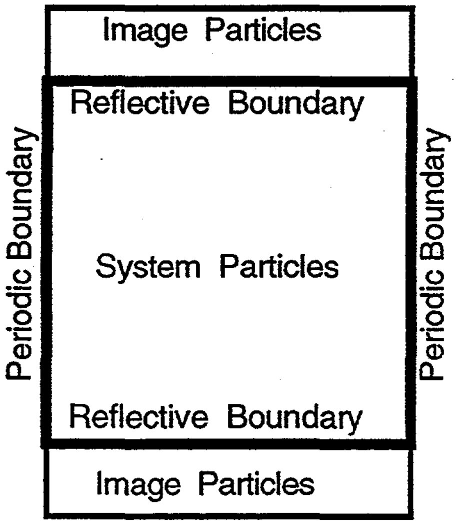

Figure 7.3 Schematic picture of boundary conditions for studying Richtmyer-Meshkov instability.

We need no special interface boundary condition. This situation differs from that using typical finite difference algorithms. SPAM allows a mixing of two materials without mesh tangling.

Shock waves can be generated by several different methods: we can use again the piston method of Chapter 6 to generate propagating shock waves, or we can use an initial perturbation corresponding to the shocked condition in one material. Shock waves generated by pistons in finite difference methods can be smoothed by artificial viscosity but their structure is sensitive to the numerical value of viscosity. Shock waves with SPAM are less sensitive to the numerical value of artificial viscosity as we showed in Chapter 6. There, reflective and transmitted shock waves remained coherent through a density discontinuity. In the Richtmyer-Meshkov instability problem, we also must include perturbed interfaces in the density discontinuity region.

The reference frame of the system is the Laboratory frame. Initial velocities of all particles are zero for both materials. The initial pressure is constant and continuous across the two materials. To maintain a constant pressure across the two materials, the initial temperatures and energies are different in the different density regions. With our method, we include a small pressure fluctuation in the perturbed interface region. In order to make this effect small, we use a different artificial viscosity: at the initial stage of evaluation, a large artificial viscosity is used to smooth out the interface pressure fluctuation.

For the constitutive equation, we use the ideal gas equation of state,

$$P = \rho e \; ; \quad k_B T = e, \tag{7a,b}$$

where P is pressure, T is temperature, k_B is Boltzmann's constant *per unit mass*, e is internal energy, and ρ is density. The density ratio is achieved through the mass ratio. The mass of lower density material is always set to unity. We can also implement different specific heat ratios for different materials used in SPAM algorithm.

We simulate a small perturbation for which linear theory is applicable, $ka_o = (2\pi/\lambda)a_o << 1$. In the next Section we describe the numerical results and discuss them.

7.4 Results and discussion

To begin, we must first confirm that the smooth particle method produces linear growth rate for a small amplitude perturbation in the shock problem. Considering the gravitational force for Rayleigh-Taylor instability, we can apply the shock wave (impulsive force) in two different ways. One way is to generate shock waves using a moving piston (boundary) far from the interface at time t = 0.

The shock wave moves with the boundary but since the shock velocity is faster than the moving boundary (piston) velocity so that the shock hits the interface before the moving

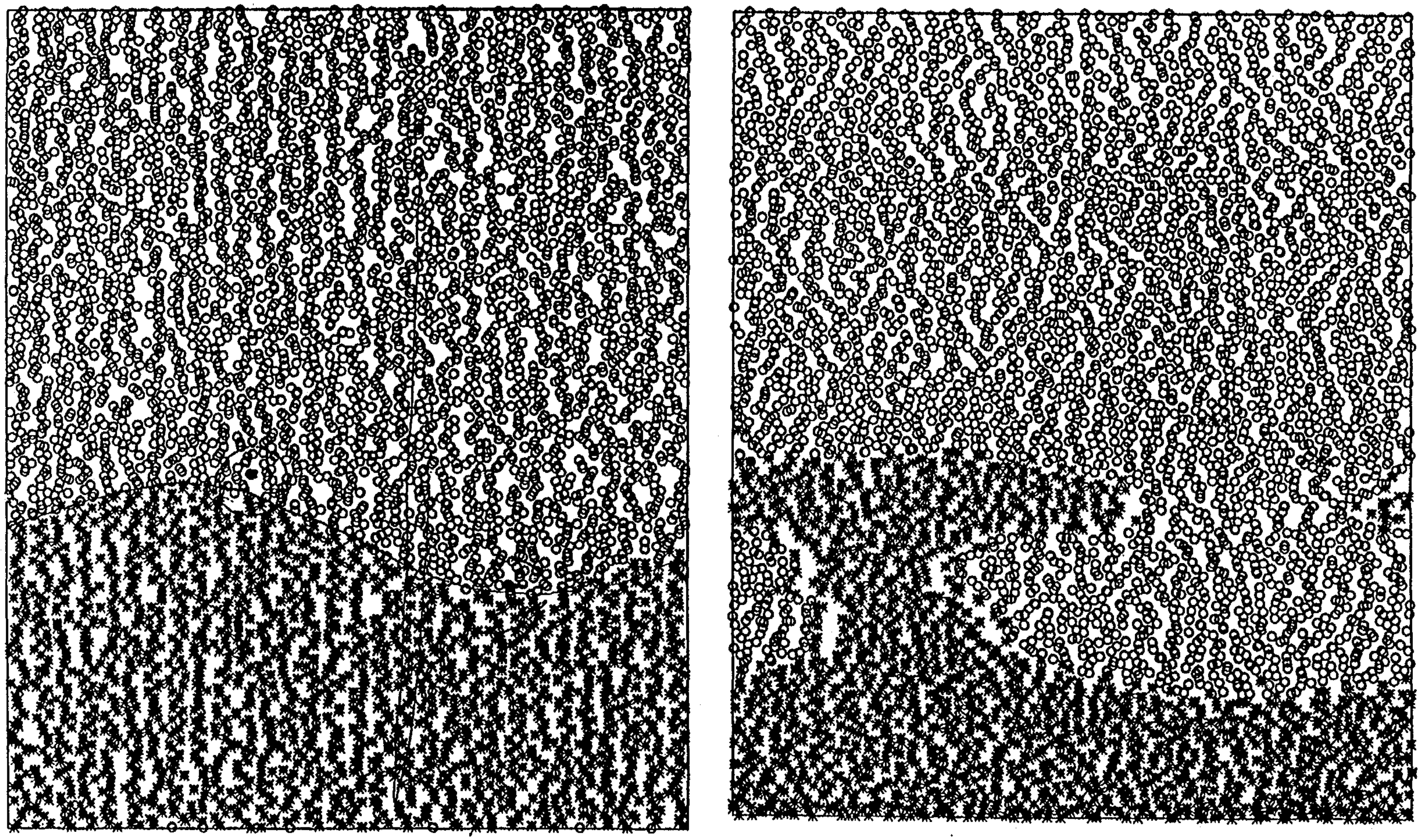

(a)

(b)

Figure 7.4 Richtmyer-Meshkov instability growth with sine wave perturbation. In this model one region is shocked with no moving boundary. B spline weighting function with smoothing length 2.5 and ideal gas equation of state are used. All other initial data were lost when **Meiko** was misoperated. (a) initial perturbation. (b) interface growth at SPAM cycle 4000 (time 20).

boundary does. A second way is to set all the physical variables, particle velocity, pressure, density, and energy, of the particles in one region to the shocked values initially. In this case the system boundary does not need to move at all. This idea is similar to using a gravitational force to study Rayleigh-Taylor instability. This low-cost model is good for a small system where there is no space to generate the shock wave by modeling a moving boundary. See Figure 7.4. In this Figure, we use sine type interface perturbation with ideal gas equation of state, equation (7). But we lost all information about the initial conditions when we lost 612 files on the **Meiko** machine.

Physically there is no difference between sine type and cosine type problem. But when sine type perturbation is used, almost all particles have x-velocity so that it is hard to quantify the growth rate and the particle velocity. The particles near the two lateral boundaries have horizontal velocity components so that they move horizontally when the interface starts to grow. The time derivative of the perturbed amplitude, equation (6b), at the two lateral edges produces

$$[da(t)/dt]_{x=0 \text{ or } x=Lx} \propto u_x, \tag{8}$$

where u_x is the horizontal velocity component of particle. This is not zero because the growth rate is non zero. Thus the interface has a horizontal non zero gradient. This gradient causes early nonlinear growth in the central region of the interface.

For the piston model, we saw linear growth. See Figure 7.5. Initially, Figure 7.5 (a), all particles are displaced randomly within a square box made by half inter particle distance from their original square lattice sites. The perturbation is one cosine wave. The wave number k is $2\pi/30$. In Figure 7.5, two different materials are marked by circles and stars. The total number of particles is 9 000 (30 x 300). Their initial density ratio is five. Since this system is comparatively small, we generate a shock wave in the dilute region so that the Atwood number is positive. For a negative Atwood number, we would have

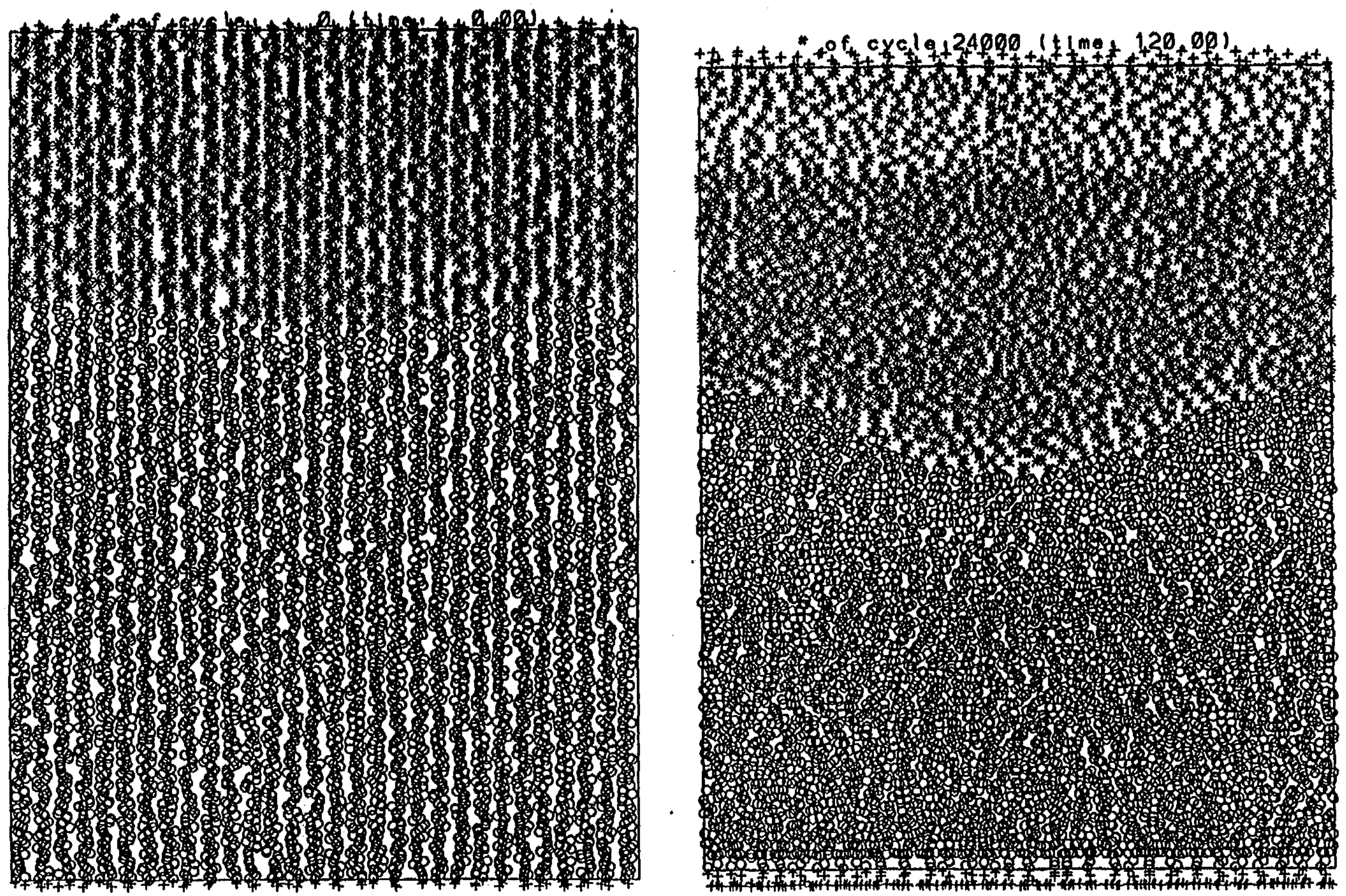

(a) (b)

Figure 7.5 Richtmyer-Meshkov instability growth with cosine wave perturbations. In this model shock waves are generated by a moving boundary and propagate from bottom to top. 30x300 particles with the ideal gas equation of state are used. B spline weighting function using smoothing length 2.5 is used. Initial reduced density ratio is 5. (a) initial perturbation, particles are randomly displaced in small distance centered at regular lattice sites. Top material is denser than bottom material. (b) at time 120. Maximum shock compression occured at time 67. Linear perturbation growth can be seen clearly from (b), no horizontal velocities.

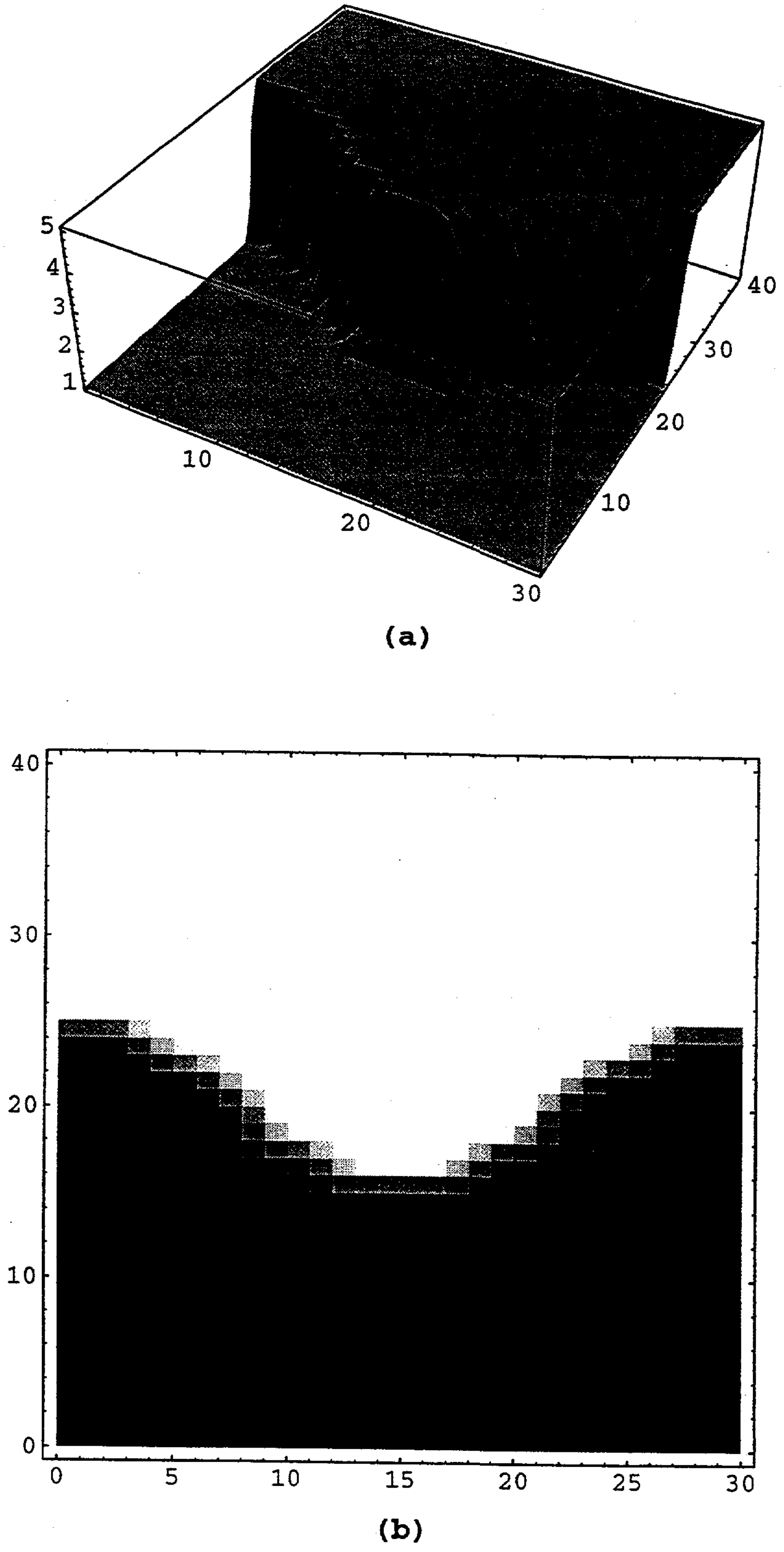

Figure 7.6 Average density discontinuity in SPAM model. Two densities are smoothly varied in interface region. (a) Three dimensional picture of interface region. Density is plotted with ratio of five. (b) Density contour map. We see that the interface is relatively smooth.

phase inversion which takes additional time. We can see it but the relatively long time required makes the relatively small system collapse. Our model seems otherwise to be quite generally useful. The density distribution is not discontinuous across the interface in the Smooth Particle method. It can be controlled by the smoothing length of the weighting function.

Here we use B spline weighting function with a smoothing length 3. Figure 7.6 shows the smooth average density profile across the interface. This smooth profile resembles those in real experiments done by M. Brouillette and B. Sturtevant without a separating membrane. See Figure 7.2. Our thermodynamic equation of state is the ideal gas equation of state, equation (7a, b), in both regions. The materials have the same specific heat ratio ($c_p/c_v = 2$) but different densities.

The shock wave was generated by the pushing the lower boundary upward. The system size of the lower part, marked by circles, is bigger than that of the upper part to allow time for shock wave to travel upward. Shock waves arrive at the interfaces at about time 67. Just after this, the traveling shock waves divide into two parts, transmitted and reflected. The maximum compression of interface due to shock wave also occurs at about time 67. The perturbed amplitude (a_0) at maximum compression is 1.889. Figure 7.5 (b) is the configuration at time 120. The time at which the amplitude grows larger than 5.0 occurs at time 100. The amplitude was 5.041 and this is approximately the start of nonlinear growth because ka_0 is considerably greater than one. This time 100 agrees with the fact that the maximum valid time allowed in the linear region is approximately equal to $\lambda/[u]$, 36 in the model after the maximum compression occures.

To calculate the growth rate analytically, we use the equation (3) or equation (5). In this model wave vector k is $2\pi/30 = 0.209$; the impact velocity (particle velocity after shocking) [u] is 0.826; the Atwood number after shocking is 0.625; the amplitude just after shocked is 1.889. Therefore the analytic growth rate is 0.204.

As in the Figure 7.5 (b) the cosine perturbation makes the lateral ends points fixed, with no horizontal velocity. This provides easy way to calculate particle velocity and the amplitude growth length with one wave length in the linear region. Thus the linear growth is clear in this Figure. We can also see the traveling transmitted and reflected waves in the Figure 7.5 (b).

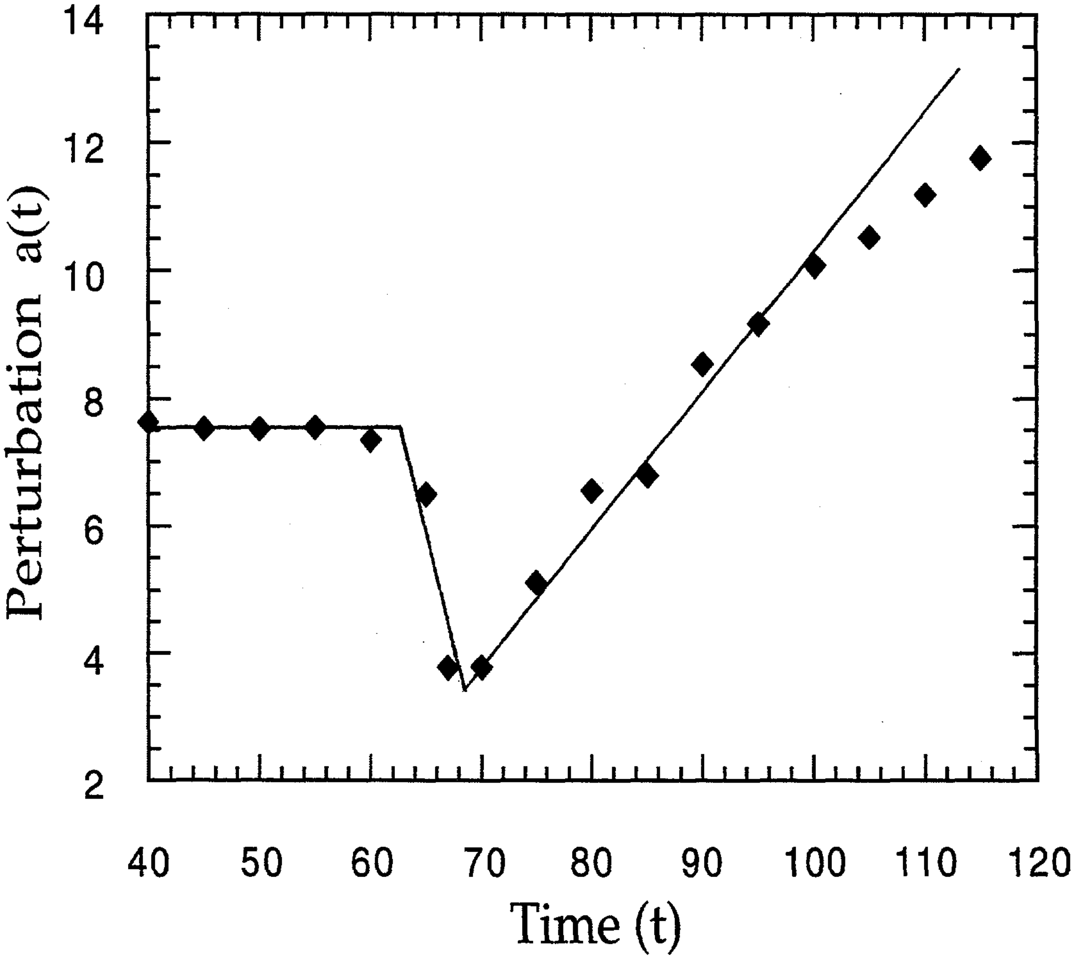

Figure 7.7 Perturbation growth as a function of time. Linear growth occurs from time 67 to about 100. At time 100 perturbation grows nonlinearly. The solid line is the linear interpolation line and its slope is 0.210. The analytic result for the growth rate is 0.204. See the text for details.

Figure 7.7 shows the amplitude growth as a function of time. The time range is plotted from 40 to 120. Initially the perturbation amplitude is constant up to time about 60. Maximum compression occurred at time 67. After that the amplitude grows linearly up to time 100. In this model the growth after time 100 is nonlinear.

The slope of the solid line (linearly interpolated with the growth data from time 67 to 100 in the linear region) in the Figure 7.7 is 0.210. Thus the computed result agrees with the analytic result within 3%. If we apply equation (5) the growth reduction parameter ψ is 1.015. Our density smoothing in the interface region is very small compared to the wavelength as seen in the Figure 7.6. Thus the growth reduction parameter ψ is close to unity. This is also true in the experimental data [14].

7.5 Summary

For a system with a density discontinuity the force applied makes the system unstable whenever the direction of applied force is the same as the direction of density gradient. For example, gravity causes Rayleigh-Taylor instability, shear causes Kelvin-Helmholtz, and a shock wave causes Richtmyer-Meshkov instability. Usually the instability grows exponentially in time but the Richtmyer-Meshkov instability caused by an impulsive shock load grows linearly in time.

The basic physics of this instability is interesting and has important technological applications. We demonstrated a way to solve this problem with a comparatively simple numerical method, SPAM. We showed that our SPAM algorithm predicts good results reproducing the analytical growth rates in equations (3) and (5) for small amplitude perturbations.

In the nonlinear range there is no theory. SPAM is good for studying this nonlinear instability problem because it can reproduce experimental data for the nonlinear range. For higher precision we would need to expand the system size using parallel processing. The SPAM algorithm requires inter-processor communication four times per cycle: the first communication occurs in calculating density; the second in calculating gradients of temperature and velocity; the third in calculating force, and finally, in the time step integration. If we use fourth-order Runge-Kutta method, we would have sixteen inter-processor communications per time step. For systems of up to 10 000 particles a single processor machine can be used.

Lawrence Livermore National Laboratory's A division has studied these instability problems for decades. This project began to follow up Dr. Alan J. Spero's smooth particle research. He hoped that this simple method could be used to study instability problems. Unfortunately he left A Division before seeing these results. We hope that he has maintained his interest in this work. We dedicate this chapter to him and his friends in A Division to honor his project idea and to express our gratitude for his help in obtaining financial support.

References

[1] S. Chandrasekhar, **Hydrodynamic and hydromagnetic stability** (Oxford, London, 1961).

[2] D. J. Tritton, **Physical fluid dynamics** (Oxford, London, 1988).

[3] K. Takayama (ed.), **Shock waves, Proceedings of the 18th international Symposium on shock waves** (Springer-Verlag, Berlin, 1992).

[4] B. J. Daly, "Numerical study of two fluid Rayleigh-Taylor instability", Physics of Fluids **10** (1967) 297.

[5] X. L. Li, "Study of three-dimensional Rayleigh-Taylor instability in compressible fluids through level set method and parallel computation", Physics of Fluids A **5** (1993) 1904.

[6] D. Ofer, D. Shvartz, Z. Zinamon, and S. A. Orszag, "Mode coupling in nonlinear Rayleigh-Taylor instability", Physics of Fluids B **4** (1992) 3549.

[7] C. L. Gardner, J. Glimm, O. McBryan, R. Menikoff, D. H. Sharp, and Q. Zhang, "The dynamics of bubble growth for Rayleigh-Tarlor unstable interfaces", Physics of Fluids **31** (1988) 447.

[8] K. A. Meyer and P. J. Blewett, "Numerical investigation of the stability of a shock-accelerated interface between two fluids", Physics of Fluids **15** (1972) 753.

[9] K. O. Mikaelian, "Freeze-out and the effect of compressibility in the Richtmyer-Meshkov instability", Physics of Fluids **6** (1994) 356.

[10] J. W. Grove, R. Holmes, D. H. Sharp, Y. Yang, and Q. Zhang, "Quantitative theory of Richtmyer-Meshkov instability", Physical Review Letters **71** (1993) 3473.

[11] G. Dimonte and B. Remington, "Richtmyer-Meshkov experiments on the Nova Laser at high compression", Physical Review Letters **70** (1993) 1806.

[12] V. Rupert, "Shock-interface interaction: current research on the Richtmyer-Meshkov problem", in **Shock waves, Proceedings of the 18th international Symposium on shock waves**, edited by K. Takayama, (Springer-Verlag, Berlin, 1992).

[13] M. Brouillette and B. Sturtevant, "Experiments on the Richtmyer-Meshkov instability: small-scale perturbations on a plane interface", Physics of Fluids A **5** (1993) 916.

[14] M. Brouillette and B. Sturtevant, "Experiments on the Richtmyer-Meshkov instability: single scale perturbations on a continuous interface", Journal of Fluid. Mechanics **263** (1994) 271.

[15] J. F. Barnes, P. J. Blewett, R. G. McQueen, K. A. Meyer, and D. Venable, "Taylor instability in solids", Journal of Applied Physics, **45** (1974) 727; J. F. Barnes, D. H. Janney, R. K. London, K. A. Meyer, and D. H. Sharp, "Further experimentation on Taylor instability in solids", Journal of Applied Physics, **51** (1980) 4678.

[16] J. W. Swegle and A. C. Robinson, "Acceleration instability in elastic-plastic solids. I. Numerical simulations of plate acceleration", Journal of Applied Physics, **66** (1989) 2838;

A. C. Robinson and J. W. Swegle, "Acceleration instability in elastic-plastic solids. II. Analytical techniques", Journal of Applied Physics, **66** (1989) 2859.

[17] K. O. Mikaelian, "Effect of viscosity on Rayleigh-Taylor and Richtmyer-Meshkov instabilities", Physical Review E **47** (1993) 375.

[18] Y. Yang and Q. Zhang, "Small amplitude theory of Richtmyer-Meshkov instability", Physics of Fluids **6** (1994) 1856.

[19] K. O. Mikaelian, "Oblique shocks and the combined Rayleigh-Taylor, Kelvin-helmholtz, and Richtmyer-Meshkov instabilities", Physics of Fluids **6** (1994) 1943.

CHAPTER 8

TURBULENCE IN HOMOGENEOUS SHEAR FLOW *VIA* MICROSCOPIC AND MACROSCOPIC SMOOTH PARTICLE APPLIED MECHANICS

Blank page

8.1 Introduction

Turbulence is an all-pervasive ubiquitous phenomena present in, for example, weather patterns, ocean currents, flows around flying aircraft, high-temperature plasmas, astrophysical jets, and combustion.

There is no completely satisfying definition of turbulence because nearly all kinds of different problems are turbulent. But from the above examples, we can drive the *definition* of turbulence: the turbulence is observed in macroscopic fluctuating flow phenomena. According to reference [1], the more exact *definition* of turbulence is a complex fluctuating flow resulting when the Lyapunov instability of the hydrodynamic equations generates information more rapidly than it can be dissipated by viscosity, making the flow field unpredictable, except in a statistical sense.

Why should we have interest in turbulent problems? Because it is closely related to economics, exact long time weather forecast, fast and quiet submarine, fast airplane flight without turbulent air flows are all examples of economically desired machines. Despite the best theoretical and experimental attempts over more than a century, and more recent computational approaches, turbulence still remains one of the great unsolved (families of) problems of fundamental physics, and poses a grand challenge comparable to other prominent scientific problems, such as the large-scale structure of universe and the nature of subatomic particles.

Smooth particle applied mechanics provides a way to study this problem. Using smooth particle applied mechanics with particles of unit mass, and a stress tensor obeying the two dimensional scalar ideal-gas equation of state $P \equiv \rho^2/2 \equiv \rho e$, provides equations of motion isomorphic to the motion equations of monatomic molecular dynamics [2]:

$$\{d^2r_i/dt^2 \equiv du_i/dt \equiv -\nabla_i\Phi\};\ \Phi \equiv \Sigma\phi_{i<j}, \tag{1}$$

where $\phi(r)$ is the pair potential. The usual smooth particle weighting function w(r) differs, in shape and in range, from conventional pair potentials $\phi(r)$. The smooth particle function has no strongly repulsive core and is also relatively long ranged, so that each smooth particle simultaneously interacts, relatively strongly, with many others.

In smooth particle applied mechanics density and energy sums the self-contribution of each particle w(0) is included. In molecular dynamics the corresponding contributions to the energy $\{\phi(0)\}$ are conventionally not included. This difference does not affect the isomorphism of the two kinds of particle trajectories, since w'(0) vanishes.

Smooth particle applied mechanics, with the two-dimensional ideal-gas equation of state, becomes an interesting model for compressible turbulence with high-Reynolds-number shear flow. Moreover, the statistical mechanics and hydrodynamics of the corresponding long-ranged molecular systems, with pair potentials resembling Lucy's weighting function [3], have not yet been systematically explored.

In particular, turbulence on the border line between microscopic and macroscopic hydrodynamics is very interesting to us. We analyze this problem with the isomorphic model of Molecular Dynamics [2].

In Section 2 we summarize the basics of turbulence. In Section 3 we describe the simulation models. Though the smootheness analysis of smooth particle method is not closely related to turbulence, it is interesting problem and gives us the idea of the particle distributions. We discuss this problem in Section 4. In Section 5, we discuss our results and conclusions. Finally, in Section 6 we summarize this chapter.

8.2 Basics of turbulence.

The most fundamental and important problems in turbulent theory are:

(1) What is the Reynolds-number dependence of the ratio of the largest to the smallest excited scales of turbulent motion?

(2) What is the kinetic energy distribution over different scales and how rapidly is energy transferred from the largest to smallest scales?

(3) What is the energy transferring mechanism and what are the roles of all the terms in hydrodynamic conservation equations?

(4) What are the tendencies toward homogeneity and isotropicity?

(5) What are the main effects of compressibility on turbulent structure?

(6) What is the effect of compressibility on the energy cascade process and on turbulence spectra?

These questions have been investigated experimentally, analytically, and numerically by many authors [4 - 24], but still very little is known.

Experimentally many turbulent problems are analyzed by measuring frequencies and related energies. These frequencies are measured by wave numbers. This idea makes the numerical calculation in wave number space, the "spectral method". Fourier transforms connect the real velocity space to wave number space. The Spectral method of solving the hydrodynamic equations requires changing the governing partial differential equations written in terms of wave number and time variables by Fourier transform. This method changes the partial differential equations in space dimensions to the ordinary analytic equations in the wave number space. By doing this fewer degrees of freedoms are sometimes enough to give fine results. This structure is similiar to that of smooth particle mechanics for dealing with partial differential equations.

The kinetic energy of the system can be expressed in terms of two alternative sums: the sum of the squared velocity in a regular spatial grid or the sum of the squares of the corresponding spectral components of velocity on a reciprocal-space grid. The two spaces are related to one another by the Fourier transform of the velocity. For example, the spectrum of kinetic energy can be described in terms of the Fourier transform of velocity u on a two-dimensional spatial square lattice.

Every regular point in space dimension with a velocity, $u_i(r_i) \equiv u_i(x_i, y_i)$ at point $r_i \equiv (x_i, y_i)$ corresponds to a Fourier transformed velocity $\tilde{u}_i(k_i) \equiv \tilde{u}_i(k_i^x, k_i^y)$ in spectral space. The relations can be expressed in the form of (fast) Fourier transform:

$$u_i(r_i) = \sum\sum \tilde{u}_j(k_j^x, k_j^y) \exp[2\pi i\{(k_j^x \cdot x_j + k_j^y \cdot y_j)\}/N], \tag{2}$$

where N is total number of points and the summations are taken over $-N/2 < \{k_j^x, k_j^y\} \le N/2$. $-N/2$ is not included since the spectral energies at $-N/2$ and $N/2$ are identical. To use the **fast** Fourier transform method, N is of the form 4^n in two space dimensions and 8^n for three space dimensions for any integer n. The square of the Fourier coefficients $E_{kinetic}(k_i) = |\tilde{u}(k_i)|^2$ $[k_i \equiv (k_i^x, k_i^y)]$ is called the kinetic energy spectral density. By Parseval's theorem,

$$\langle E_{kinetic} \rangle = N \sum E_{kinetic}(k_i), \tag{3}$$

where the summation is taken over $-N/2 < \{k_i\} \le N/2$. For the three-dimensional isotropic case, $E_{kinetic}(k) \approx 4\pi k^2 E_{kinetic}(k_i)$, and for the two-dimensional isotropic case, $E_{kinetic}(k) \approx 2\pi k E_{kinetic}(k_i)$, $|k_i| = k$, where k is the length of vector k_i.

A characteristic of turbulent flows is the net average transfer of energy from smaller wavenumbers [larger wavelengths] to larger wavenumbers [smaller wavelengths]. This phenomenon (described by the Navier-Stokes equations) is inherently nonlinear. A schematic picture of spectral energy transfer is shown in Figure 8.1 (a). Figure 8.1(b) shows the spreading of a contaminant in turbulent flow [4]. The eddies are embedded within each other and the eventual product of the cascade, where dissipation takes place, is a highly convoluted multifractal sheet shown in Figure 8.1 (b). As shown in Figure 8.1 (a), the eddies of size L ($\equiv 1/k$) interact with each other and with the more energetic large-scale eddies to generate smaller eddies.

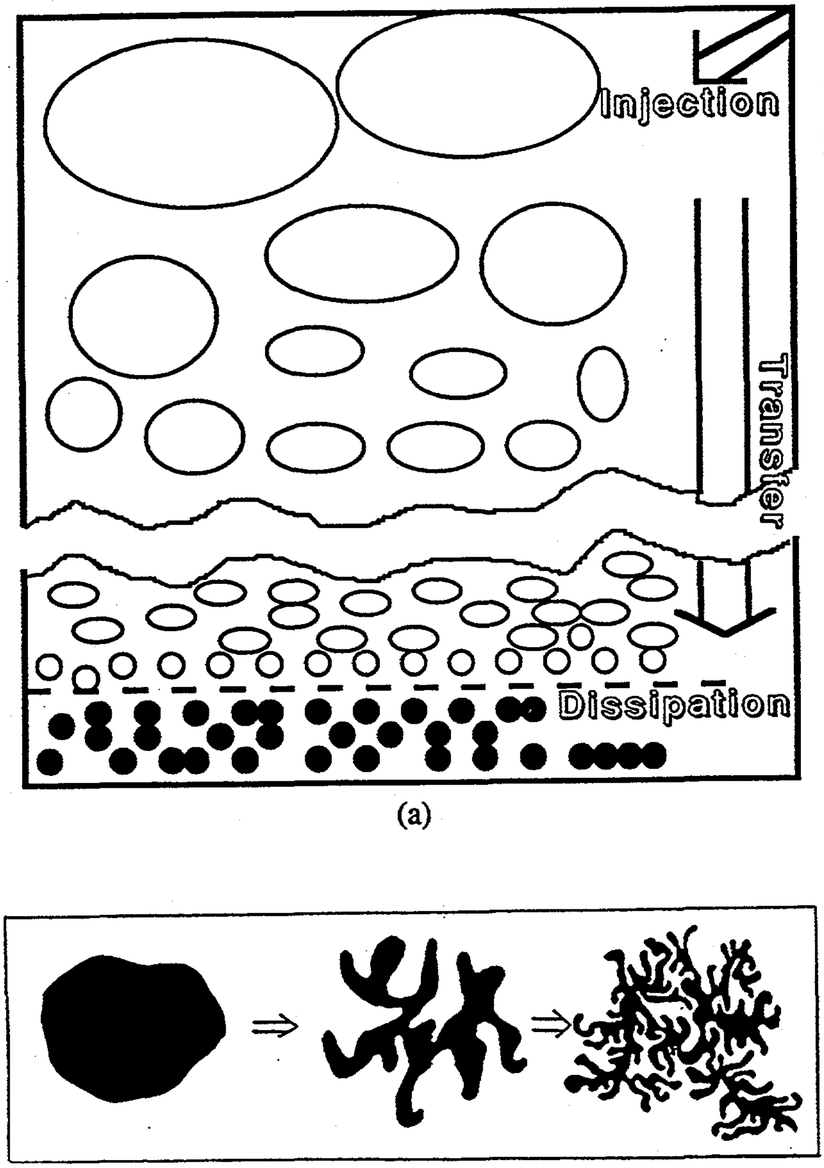

(a)

(b)

Figure 8.1 Turbulent cascade: (a) schematic diagram of spectral energy transfer in turbulence. The injected energy from the boundary generates the largest eddies. The larger eddies generate smaller eddies and the injected energy is transferred until the energy is dissipated to the heat by viscosity. (b) contaminant spreading in turbulent flow. The eddies are embedded within each other. The eventual product of the cascade is highly convoluted multifractal sheets.

These smaller-scale eddies, in turn, populate eddies of yet smaller size. The whole process is called the turbulent cascade.

The energy spectrum E(k) (kinetic energy per unit mass and unit wavenumber k) depends on the wavenumber k. Kolmogorov explained many aspects of the spectrum by dimensional analysis. In a stationary process, for a system with steady total energy, the rate of energy injection from boundary, the rate of energy transfer through cascade, and the rate of microscopic energy dissipation by viscosity are all the same and must be a function with units $[L^2/T^3]$ where all energies are specific-(per unit mass) with units $[L^2/T^2]$. Kolmogorov begins by taking the spectral energy density to be a function of the energy rate, $\dot{e}$ with units L^2/T^3, and the wavenumber k with units L^{-1}:

$$E_{kinetic}(k)\ [L^3/T^2] \sim \dot{e}^{\,\alpha} k^{\beta} \rightarrow [L^2/T^3]^{\alpha}[1/L]^{\beta}, \tag{4}$$

where $\alpha = 2/3$ and $\beta = -5/3$ are necessary in order to match the units. This result, that the spectral strength must fall off as $k^{-5/3}$, is Kolmogorov's 5/3 law. This law holds independent of problem dimensionality. The total kinetic energy per unit mass is the sum over all wave numbers:

$$E_{kinetic} = \int E_{kinetic}(k)\, dk \sim \dot{e}^{\,2/3} k^{-2/3}\ [L^2/T^2]. \tag{5}$$

The units $[L^2/T^2]$ are the same as that of velocity squared and are consistent with the general result that specific kinetic energy (kinetic energy per unit mass) is proportional to the square of velocity (i.e. velocity $u \sim \dot{e}^{\,1/3}L^{1/3}$). Therefore, the eddy rotation time t ($\equiv L/u$) is $\dot{e}^{\,-1/3}L^{2/3}$.

The cascade must eventually stop, at some minimum eddy size of L_d, where eddies are so small that they decay appreciably due to viscosity in the time they take to rotate. If we define the viscous dissipation time t^{diss} as $L_d^{\,2}/\nu$, where ν is kinematic viscosity of the fluid, then the Kolmogorov microroscale is defined as $L_d \sim (\nu^3/\dot{e})^{1/4}$ by equating the eddy rotation time to the dissipation time, at which length the cascade is terminated by viscous dissipation. In a completely resolved numerical calculation, the mesh size must be at least as small as this microscale. See Figure 8.1.

Some authors [12, 19, 20, 30-33] find an energy spectrum $E(k) \sim k^{-3}$ rather than $k^{-5/3}$ in two-dimensional numerical models. In inviscid two-dimensional flow, the vorticity of each fluid element is a constant of motion so long as boundaries are ignored. Consequently, the squared vorticity is an inviscid constant of motion. In contrast to three dimensional flows, the two constants of motion imply that any transfer of energy to higher wavenumbers must be accompanied by a bigger transfer to lower wavenumbers. In this picture, energy cascades from input wavenumbers to lower wavenumbers through an inertial range with energy spectrum of Kolmogorov 5/3 law but the squared vorticity cascades to higher wavenumbers through an inertial range with a spectral density proportional to k^{-3}. Lilly [19] demonstrated this in his two-dimensional numerical simulation in 1969. Wiin-Nielsen [19] has shown the apparent existence of an approximately k^{-3} energy spectrum in the atmosphere between longitudinal wavenumbers k of about 8 $[m^{-1}]$ to at least 15 $[m^{-1}]$. These frequencies lie in the range between those of strong baroclinic instability, where most large-scale kinetic energy is produced, and those beyond which the atmosphere can no longer be considered quasi-two-dimensional. Along with the dimensional problem, fluid compressibility affects turbulence. In compressible fluids, many authors [17, 22, 23] report that shock wavelets exist in turbulent flow and produce energy spectra different from those of Kolmogorov 5/3 law. We describe the simulation models in the next Section.

8.3 Simulation models.

One of the simplest idealizations of turbulent shear flow is a "homogeneous" shear flow. Homogeneous shear flow refers to the problem of spatially homogeneous turbulence sustained by a velocity field generated by a constant shear rate $\dot{\varepsilon}$. To minimize boundary effects, we use specially moving periodic boundary conditions. This mechanism was already explained with the Couette flow in Section 3 of Chapter 3 in discussing the elastic properties of Smooth Particle Applied Mechanics. In the link-list algorithm with moving boundary system, each cell on the upper row has one more neighbor cell moving toward its site. See Figure 8.2 and Figure 3.2 in Chapter 3. Here we describe two different simulations related by their isomorphism: microscopic time reversible simulation and macroscopic irreversible simulation.

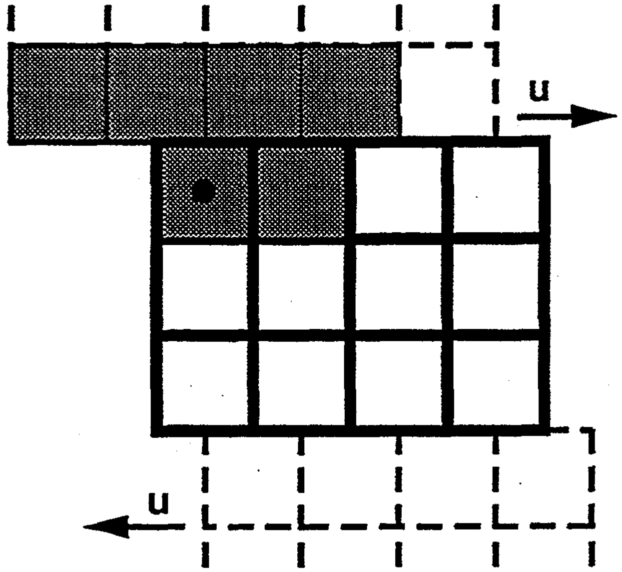

Figure 8.2 Dotted cells are periodic image cells moving with velocity u. The upper cells in the system (thick line) have one more interacting cell compared to the other cells. The black particle interacts with the particles in the shaded cells. Compare with Figure 3.2.

Homogeneous periodic shear has been studied for more than 20 years [1], using reversible Gauss [34] or Nosé-Hoover [28-29] "friction coefficients" ζ to constrain either the temperature or the internal (excluding the macroscopic flow kinetic energy) energy. For particles of mass m, and with a macroscopic (time-averaged) strain rate $\dot{\varepsilon} = du_x/dy$, the Gaussian isoenergetic form of these equations is the set:

$$\{\dot{x} = \dot{\varepsilon}\, y + p_x/m;\ \dot{y} = p_y/m;\ \dot{p}_x = F_x - \dot{\varepsilon}\, p_y - \zeta p_x;\ \dot{p}_y = F_y - \zeta p_y\}, \tag{6}$$

with

$$\zeta \equiv -\dot{\varepsilon}\, P_{xy} V/(2K);\ \ K \equiv (1/2m)\Sigma p^2. \tag{7}$$

It is convenient to solve this set of 4N equations for $\{\dot{x}\ ,\ \dot{y}\ ,\ \dot{p}_x, \dot{p}_y\}$ using the classic fourth-order Runge-Kutta method. The nature of cutoff of our smoothing function implies local trajectory errors of order dt^4. This error should exceed the time step integration global error of the fourth-order Runge-Kutta method. With a (reduced-units) time step of 0.005, the single step energy is conserved to about 9-digit accuracy. This small error can then be mostly eliminated by rescaling the momenta after each Runge-Kutta integration step. The forces $\{F_x, F_y\}$ are calculated from the gradient of Lucy's weighting function [3]:

$$w(r) = (5/9\pi)[1 + r][1 - r/3]^3;\ \ r < 3, \tag{8}$$

at unit reduced density, N=V, where the smoothing length is 3. We use unit particle mass in the calculation so that $\rho \equiv 1$. This choice gives 24 interacting neighbors for each particle when the particles are arranged in a regular square lattice and 36 interacting neighbors when the particles are arranged in a regular triangular lattice. Typical configurations of 1024 smooth particles are shown in Figure 8.3 at energy of N/2 with the moderate strain rate $\dot{\varepsilon} = 1/4$. The particle velocities are displayed in that Figure in two different ways: the individual particle "momenta" $\{p_i\}$, which represent velocities relative to the mean streaming motion,

$$\{p_i\} = \{u_i - (\dot{\varepsilon}\, y, 0)\}, \tag{9}$$

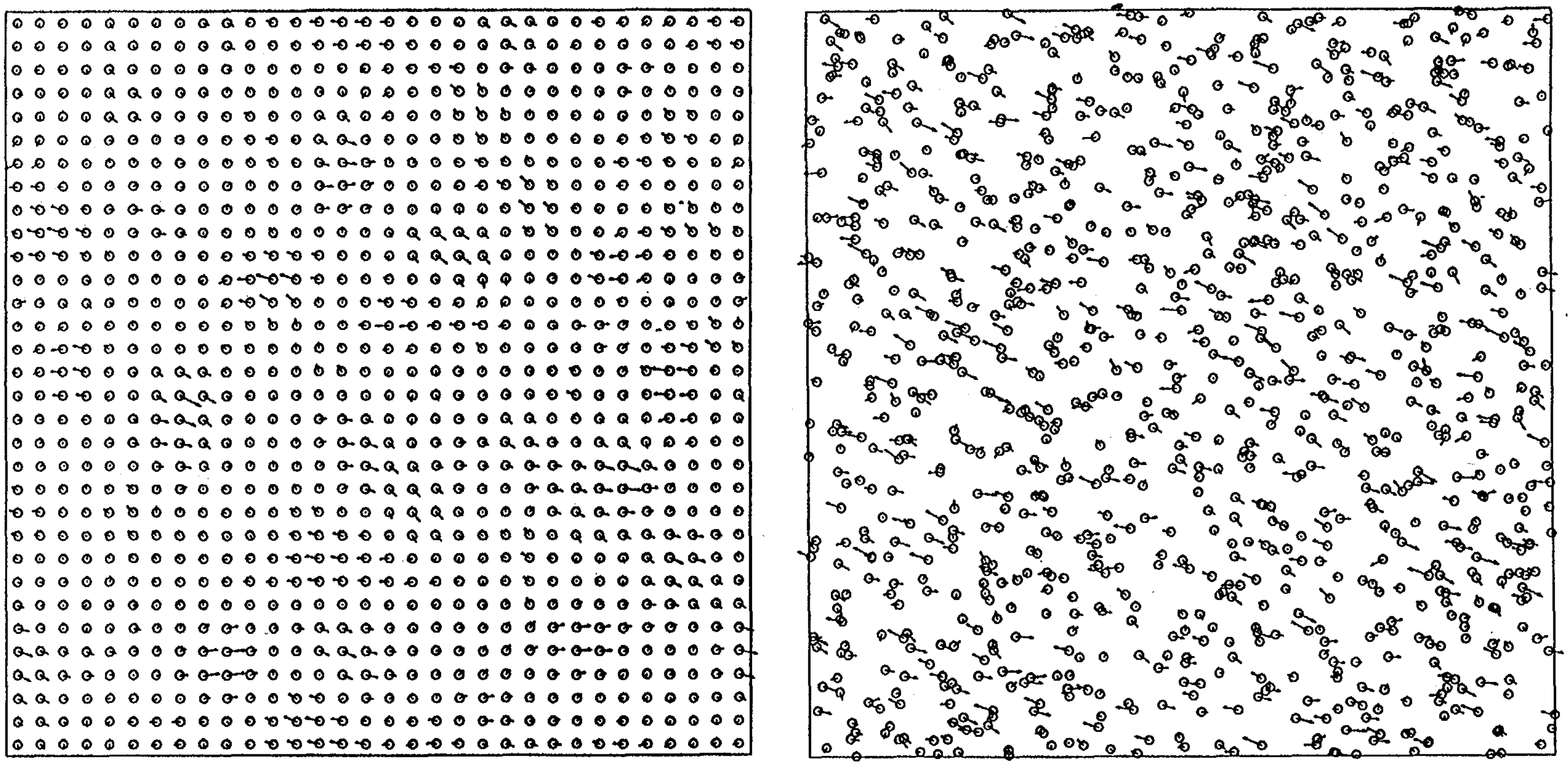

(a) (b)

Figure 8.3 Particle (with unit density) momenta, relative velocities to the mean stream motion in microscopic shear flow with smooth particles. The total number of particles is 1024. The strain rate is 0.25. The total energy is N/2: (a) average momenta at the nodes of a regular square grid. (b) individual particle momenta at particle positions.

and the averaged momenta $\{ <p_i> = \Sigma w_{ij} p_j \}$ at the nodes of a regular square grid, computed from the weighting function w_{Lucy}. Because the averaged momenta $\{<p_i>\}$ can be defined at any point in space, we have chosen to compute and display them on a square grid to facilitate the calculation of (fast) Fourier transforms of the velocity field.

Irreversible macroscopic flows are described by dissipative constitutive equations, which typically include plasticity or Newtonian viscosity, as well as Fourier heat conduction. These dissipative processes inexorably diminish velocity and temperature differences. The most interesting systems can be driven into wild chaotic time variation despite fixed nonequilibrium boundary conditions.

The Russian literature [27] stresses the need for phenomenological source terms in describing hydrodynamic flows with fluctuations. Energy sinks are often included to stabilize hydrodynamic simulations of shock waves [with "artificial viscosity"] and to avoid the explicit consideration of short wavelength degrees of freedom [with "eddy viscosity"]. Smooth particle applied mechanics contains natural velocity fluctuations with two different estimates of velocities at the nodal points, $\{u\}$, the velocities at which the points move and $\{<u>\}$, the spatially-averaged velocities characterizing the neighborhood of each moving point. In the absence of damping, smooth particle applied mechanics, like Newtonian mechanics, is exactly time-reversible [2]. If damping is required, as in driven system, then the difference between the spatially-averaged velocity and point velocity provides a natural high-frequency short wavelength heat sink:

$$\dot{U}^{SPAM}_{Eddy} \equiv [<u> - u]/\tau. \qquad (10)$$

τ is a phenomenological relaxation time which can be used to control the system energy. The damping occurs only at the smallest possible range of length scales, $\{r < h\}$. Small τ provides a flow in which the energy is nearly all potential, while larger τ provides flows with more kinetic energy. Another approach is to continuously rescale $(<u> - u)^2$ to keep the system "thermal" energy constant [35]. But we found that this approach produces a strange velocity profile and we did not consider this approach further. Before discussing the results we introduce a new way of analyzing the smoothness of the smooth particle distributions in the next section.

8.4 Smoothness analysis.

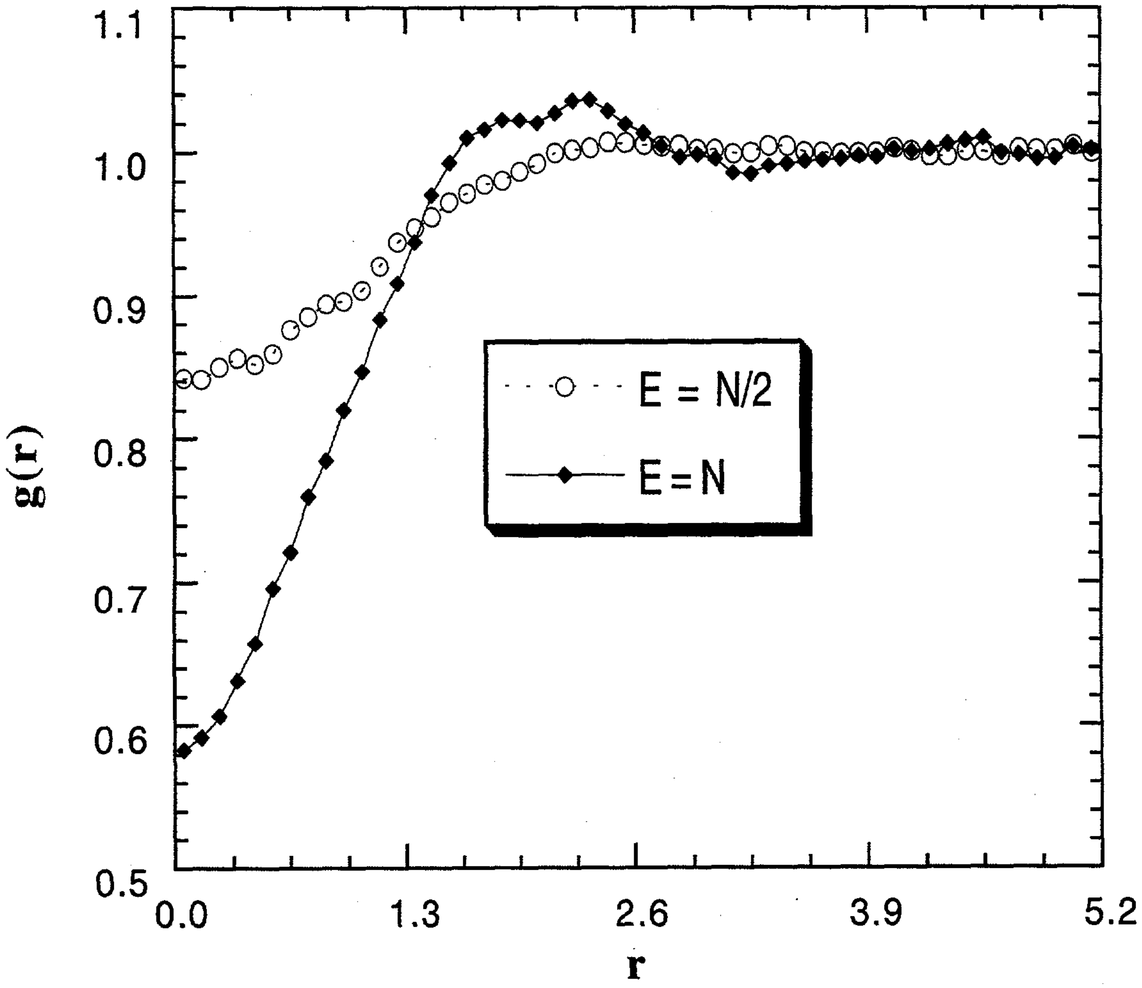

Figure 8.4 Lucy's radial distribution function with smoothing length 3 for two energies, N and N/2, where N=1024. Density is unity and time step dt = 0.005. This data is the average over 8000 cycles after discarding the first 2000 cycles.

Though this section is not directly related to turbulence, *smoothness* analysis is very useful for studying particle distributions. The *smoothness* of the smooth particle distributions can be checked by analyzing the radial distribution function. Figure 8.4 shows Lucy's radial distribution function normalized with respect to ideal gas density.

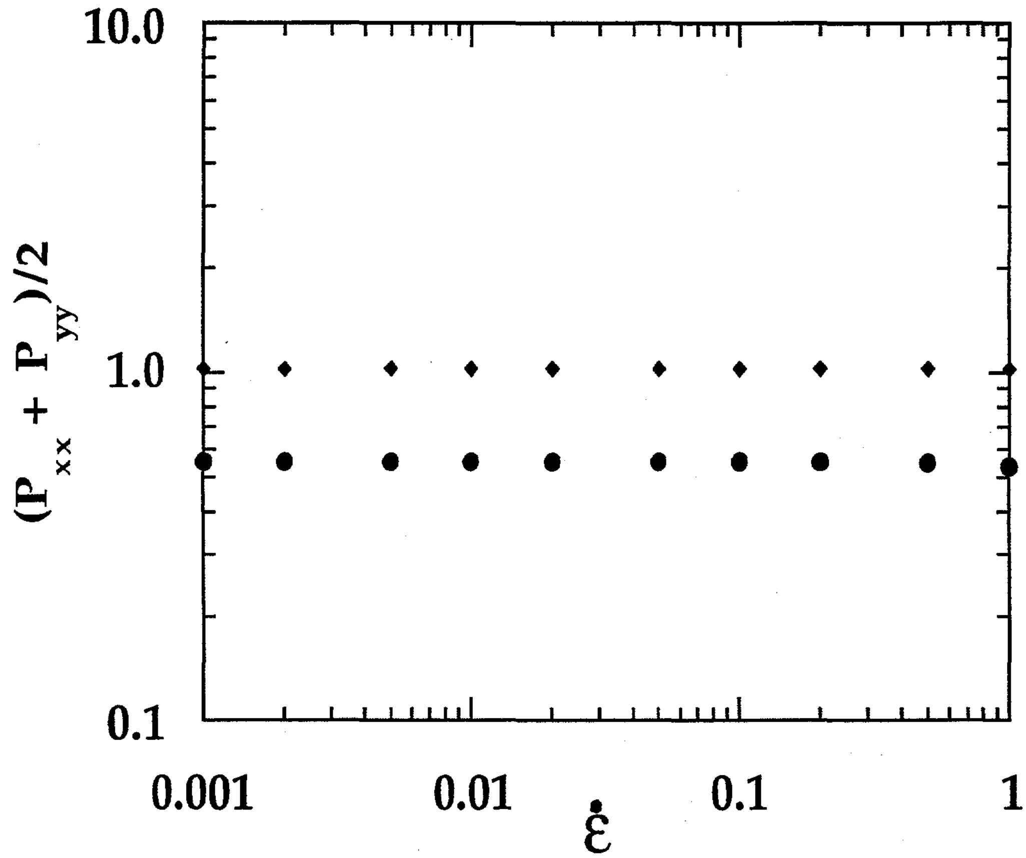

Figure 8.5 Pressure as a function of strain rate in microscopic model with Lucy potential function with smoothing length 3 at energy E = N and N/2. Static pressure is constant, independent of strain rates. Data from Professor H. A. Posch [University of Vienna].

This radial distribution function is the average over 8000 cycles of length 0.005 after discarding data from the first 2000 cycles. In terms of the radial distribution function, the potential energy per particle is expressed by the equation:

$$\Phi/N = (1/2) \int \phi(r)\, 2\pi\, rg(r)\, dr, \qquad (11)$$

where $\phi(r) = w(r)$. For Lucy's weighting function and N = 1024 particles, the potential energy per particle ignoring $\phi(0)$ is 0.423 for E = N/2 and 0.462 for E = N. These data agree with the simulated values {0.422, 0.463} within 1%. The pressure per particle is expressed by the equation:

$$PV/N = \langle p^2/2m \rangle - (1/4) \int \phi'(r)\, 2\pi\, r^2 g(r)\, dr. \qquad (12)$$

Calculated data are 0.57 and 1.02 and agree with the simulated results shown in Figure 8.5. Figure 8.4 indicates that a smooth particle has no finite volume and allows the particles to overlap substantially. It is interesting that the higher kinetic energy system (E = N) is smoother than the higher potential energy system (E = N/2) even though the higher kinetic energy system has a larger viscosity. See Figure 5.7 in Chapter 5.

Another way to analyze the topology of the flow is through the local moment of inertia tensor as suggested to us by Romeel Davé (University of California, Lick Observatory) in a 1994 Hertz Foundation interview;

$$S_{DAV\acute{E}} = \Sigma m_i (r_i^2\, I - \mathbf{r}_i \mathbf{r}_i) w(r_i - r), \qquad (13)$$

where w is a weighting function and I is the unit tensor in two dimensions.

Figure 8.6 shows the topological characteristics of the 1024 flow particles generated by the smooth particle method and by random numbers. In this Figure we calculate the moment of inertia tensor with Lucy's weighting function using smoothing length 3. Initially we start at the regular 32x32 lattice points and follow the eigenvector direction belonging to the smallest eigenvalue. Each step size is 0.1 and first 200 steps

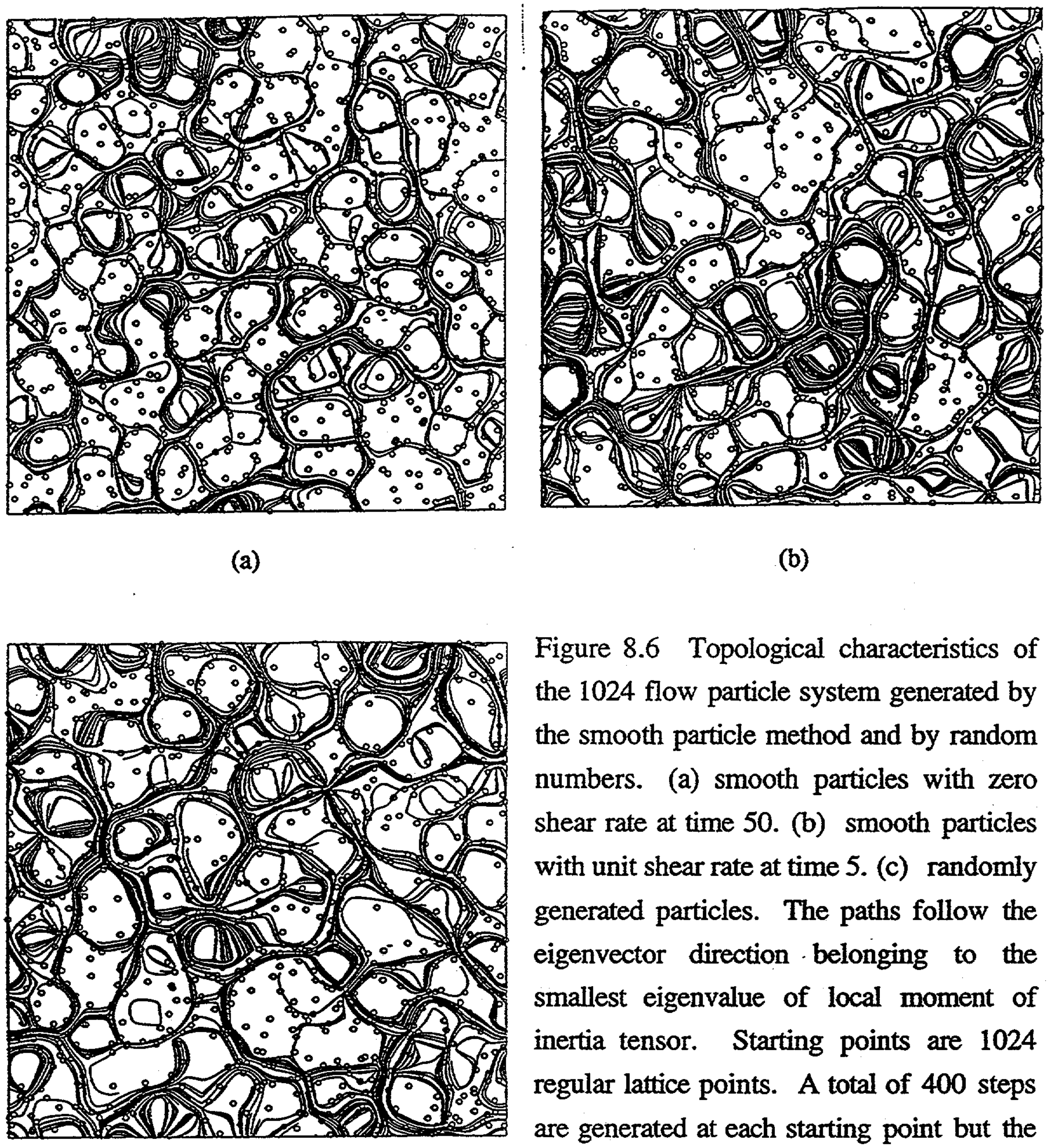

(a)

(b)

(c)

Figure 8.6 Topological characteristics of the 1024 flow particle system generated by the smooth particle method and by random numbers. (a) smooth particles with zero shear rate at time 50. (b) smooth particles with unit shear rate at time 5. (c) randomly generated particles. The paths follow the eigenvector direction belonging to the smallest eigenvalue of local moment of inertia tensor. Starting points are 1024 regular lattice points. A total of 400 steps are generated at each starting point but the first 200 steps are discarded. Step size is 0.1 and the square shown is 32x32.

are discarded and the following 200 steps are used in order to avoid small path fluctuations.

The system is neatly divided into a set of cells, the size and shape of which characterize the topology of the flow [36]. Each flow configuration and corresponding topological cells are shown side by side. In the next section, we provide results and discuss them.

8.5 Results and Discussion.

The new type of eddy viscosity, a thermostat idea, can be applied both in microscopic and in macroscopic simulations. Kolmogorov's 5/3 law can be inverted to total energy as a function of normalized wave length:

$$E_{\text{kinetic}} \sim \int k^{-5/3}\, dk \sim \int \lambda^{5/3}\, d(1/\lambda) \sim (\lambda/\lambda_{\min})^{2/3}, \tag{14}$$

where the various proportionality constants are related to the energy transfer rate and minimum wave length. The flows themselves provide numerical energy spectra supporting Kolmogrov's dimensional arguments for long wavelengths.

Figure 8.7(a) shows the results from microscopic Gaussian thermostat for 32x32 particles corresponding to Figure 8.3 for particle velocities. In this Figure, the points represent the total energy spectrum as a function of wave length and the solid line is the interpolation of the eight longest wavelength points from the energy spectrum.

The constant interpolating slope supports Kolmogorov's dimensional arguments for this small system. We can analyze this Figure 8.7(a) with that of k-space, Figure 8.7(b), which is the square lattice in k-space centered at black dot. The smallest wave number in Figure 8.7(b) is unity and represents the four sites closest to the origin. The numbers in circles in Figure 8.7(b) represent the distances from the central particle.

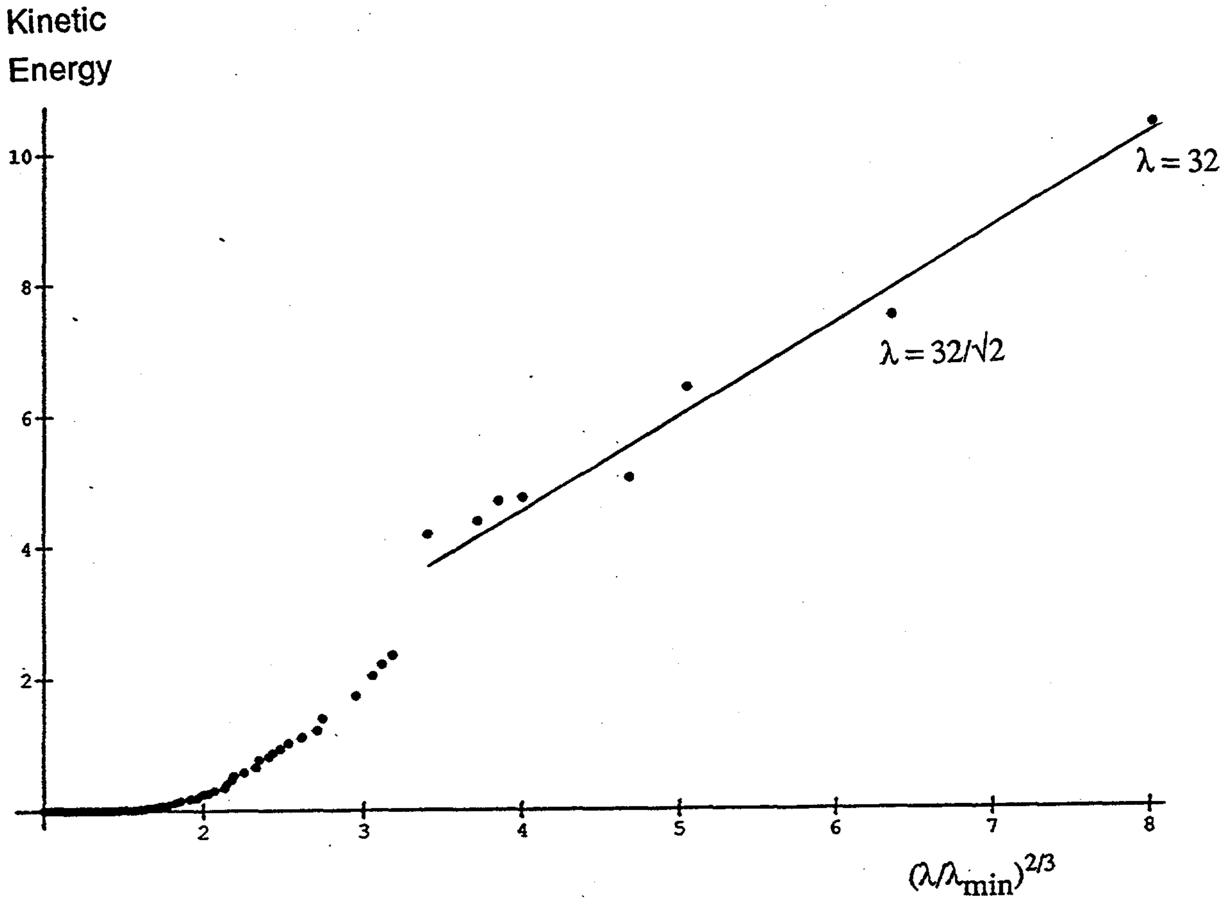

(a)

Figure 8.7 (a) Total kinetic energy per mass as a function of normalized wavelength in a system of 32x32 particles. The solid line approximates the eight longest wavelength points in the integrated energy spectrum. This is a microscopic reversible simulation with Gauss' thermostat. The total energy is N/2.

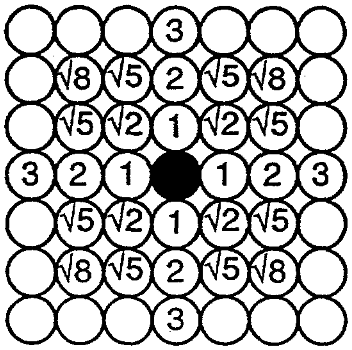

(b)

Figure 8.7 (b) Fourier wave number space in a square lattice centered at the black dot. This space is reciprocal to wavelength space. The smallest wave number points, marked by 1, correspond to the longest wavelength in Figure 8.7(a). The numbers in circles represent the distance from the central dot.

The closest four sites correspond to the longest wave length 32 and appear as the right most point in Figure 8.7(a). The next shortest wave number is the square root of two for which four sites are involved. These correspond to the second point from the right in Figure 8.7(a). Therefore, the eight points involved in interpolation in Figure 8.7(a) correspond to wavelength 32 (four points), $32/\sqrt{2}$ (four points), $32/\sqrt{4}$ (four points), $32/\sqrt{5}$ (eight points), $32/\sqrt{8}$ (four points), $32/\sqrt{9}$ (four points), $32\sqrt{10}$ (eight points), and $32/\sqrt{13}$ (eight points). Only forty-four points follow Kolmogorov's analysis out of more than one thousand points. However, this approach is entirely different to that followed by She and Jackson [37], who developed spectral methods for solving the Euler equations.

For the macroscopic simulation, the "background bulk energy" due to homogeneous shear flow depends on the system sizes:

$$E_b = \dot{\varepsilon}\, L^4/24, \tag{15}$$

where E_b is background bulk energy, $\dot{\varepsilon}$ is shear rate, L^2 is system size. We simulate the same order of bulk energy systems for three system sizes, 16x16, 32x32, 64x64. Figure 8.8 shows the kinetic energy fluctuations as a function of time for three systems. Kinetic energies converge very fast and their fluctuations are very small. We checked the spectral energy in the fully converged ranges. Figure 8.9 shows the velocity profiles for particle positions and regular grid points. We studied very small energy system (small Reynolds number system) because high kinetic energy system with big relaxation time does not show any y-velocity component either in particle position or in grid points. See the Figure 8.9. Therefore the high Reynolds number turbulent system can not be represented with relaxation time eddy viscosity. Figure 8.10 shows Kolmogorov's results for three systems. The physical interpretation is the same as that in the miscroscopic case, Figure 8.7; some large wave lengths satisfy the Kolmogorov's theory. But system size becomes bigger and bigger, the larger eddies dissipate their energies

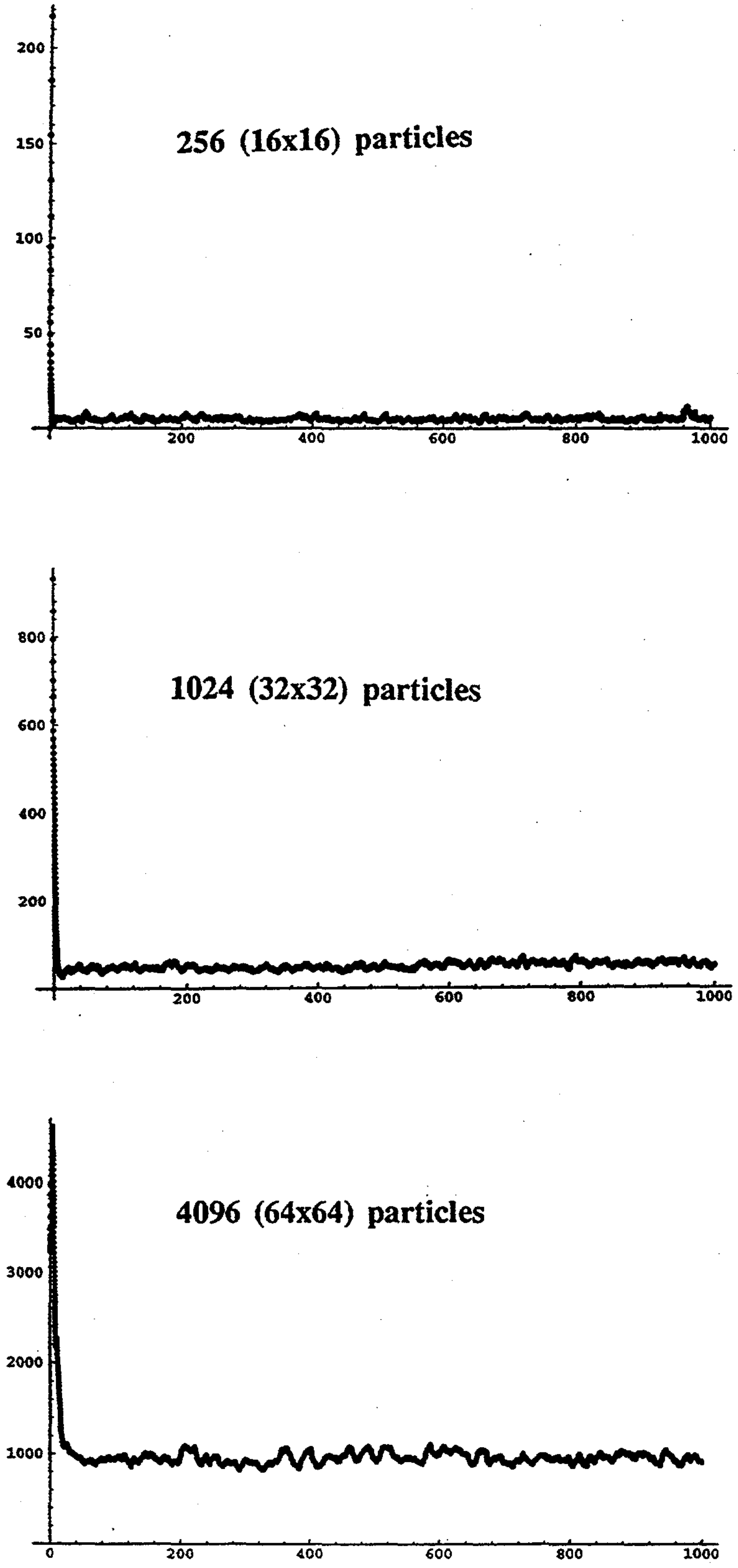

Figure 8.8 Kinetic energies as a function of time for three systems, 16x16, 32x32, and 64x64 particles. Shear rate is unity for all systems. The relaxation time τ is 1.0, 2.0, and 3.5 respectively. All system energies converge very fast and have small fluctuations. We measured the spectral energies at equal time intervals 100, 200, ..., 1000.

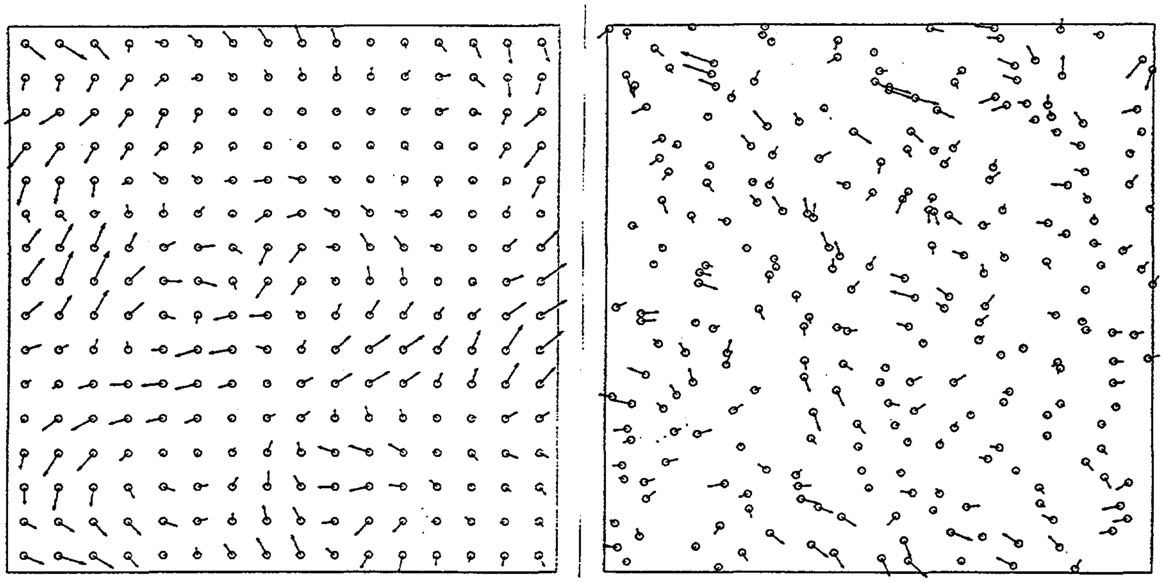

256 (16x16) particles

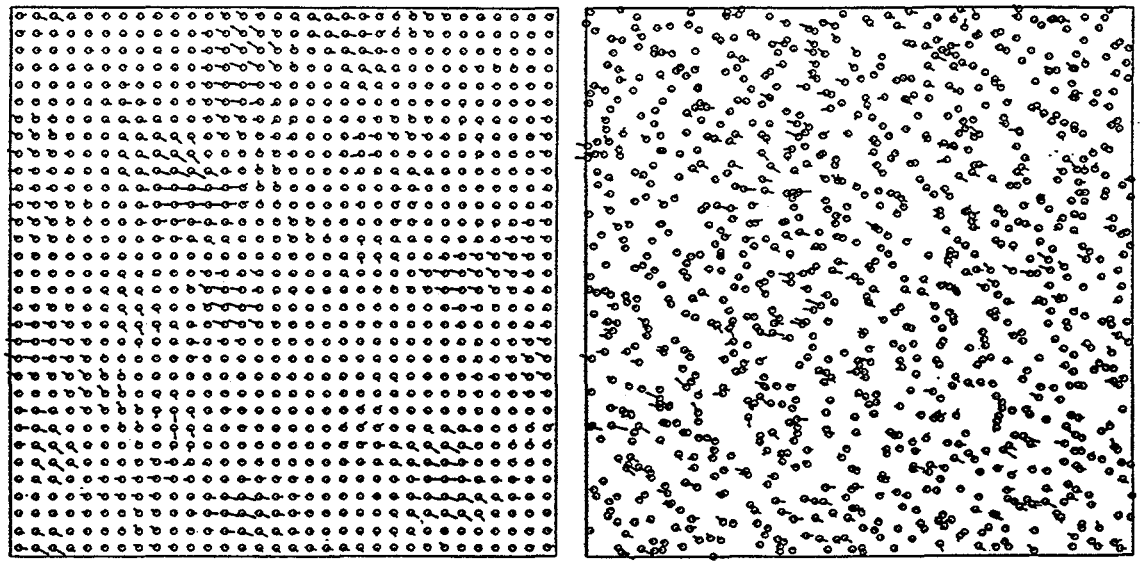

1024 (32x32) particles

Figure 8.9 Particle (with unit density) momenta, relative velocities to the mean stream motion in macroscopic shear flow for 256 (16x16) and 1024 (32x32) particles systems. Comparing average momenta at the nodes of a regular square grid with individual particle momenta at particle positions. Strain rate is unity. Relaxation time τ is 1.0 and 2.0 respectively. We neglect 4096 (64x64) system because it shows the same features except with more complexity.

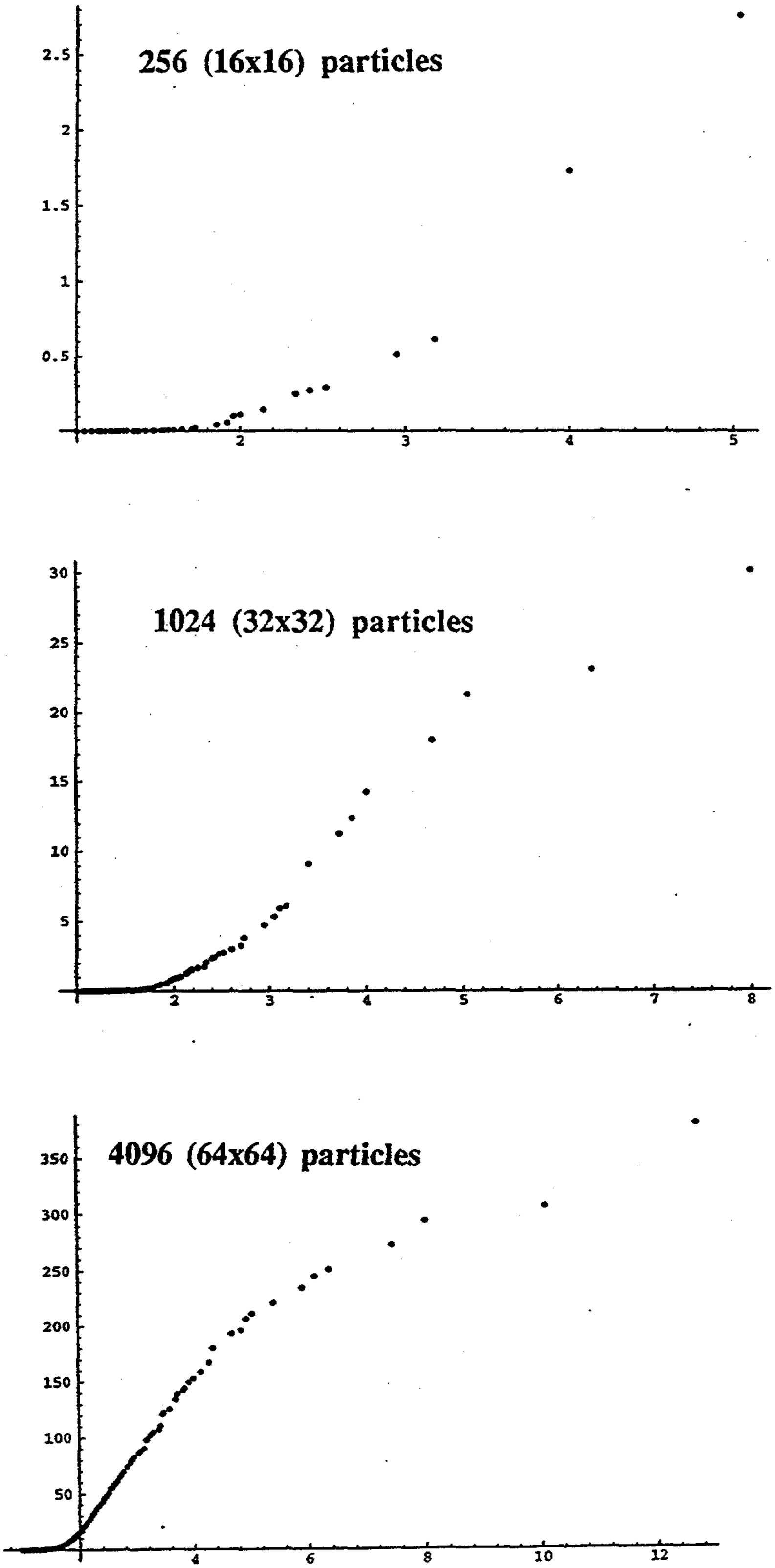

Figure 8.10 Total kinetic energy per mass as a function of normalized wavelength for 256 (16x16), 1024 (32x32), and 4096 (64x64) particles of irreversible macroscopic simulation. Shear rate is unity. Relaxation time τ is 1.0, 2.0, and 3.5 respectively. This Figure has the same interpretation as Figure 8.7(a).

more rapidly than the smaller ones. In other words, it is hard to generate the larger eddies when the system size becomes big. We can not interpret it quantitively yet but we guess that this phenomenon is due to the intrinsic viscosity shown in Figure 5.7 in Chapter 5.

8.6 Summary

Homogeneous shear flow which is substained by a velocity field generated by a constant shear rate $\dot{\varepsilon}$ can produce a simple idealization of turbulent flows. SPAM can approach homogeneous turbulent flows in two different levels, microscopic and macroscopic levels since SPAM can generate isomorphic trajectories for the isentropic ideal gas equation of state. For the two-dimensional ideal gas equation of state, the Smooth Particle method becomes an interesting model for compressible turbulence with high-Reynolds-number shear flow.

We investigated the challenging problems of turbulence along with microscopic and macroscopic shear flow equations of motion. We use the eddy viscosity with the same idea of microscopic thermostats; in miscroscopic simulation we use the Gauss reversible thermostat; in macroscopic simulation we use the velocity fluctuations, difference between the spatially-averaged velocity and point velocity, which provides a natural high-frequency short wavelength heat sink.

We simulated three system sizes, 16x16, 32x32, 64x64. For the high Reynolds number turbulent system thermostat eddy viscosity does not show turbulent eddies. For the small energy system with small relaxation time, some large wavelengths satisfy Kolmogorov's dimensional analysis, a robust part of turbulence theory. But as the system size becomes bigger, it is hard to generate energetic large wavelength eddies. From the above results we conclude that the thermostat idea of eddy viscosity, which can be one possibility in smooth particle method, is not a very good way to represent the eddy viscosity for homogeneous turbulence generated by constant shear rate.

References

[1] W. G. Hoover, **Computational statistical mechanics** (Elsevier, Amsterdam, 1991).

[2] O. Kum and W. G. Hoover, "Time-reversible continuum mechanics", Journal of Statistical Physics **76** (1994)1075.

[3] L. B. Lucy, "A numerical approach to the testing of fission hypothesis", Astronomical Journal **82** (1977) 1013.

[4] S. Corrsin, "Outline of some topics in homogeneous turbulent flow", Journal of Geophysical Research **64** (1959) 2134.

[5] H. L. Grant, R. W. Stewart, and A. Moilliet, "Turbulence spectra from a tidal channel", Fluid Mechanics **12** (1961) 241.

[6] A. Y. Kuo and S. Corrsin, "Experiments on internal intermittency and fine-structure distribution functions in fully turbulent fluid", Journal of Fluid Mechanics **50** (1971) 285.

[7] H. E. Fiedler and P. Mensing, "The plane turbulent shear layer with periodic excitation", Journal of Fluid Mechanics **150** (1985) 281.

[8] M. P. Jaroch and H. H. Fernholz, "The three-dimensional character of a nominally two-dimensional separated turbulent shear flow", Journal of Fluid Mechanics **205** (1989)523.

[9] T. J. O'hern, "An experimental investigation of turbulent shear flow cavitation", Journal of Fluid Mechanics **215** (1990) 365.

[10] W. V. R. Malkus, "Outline of a theory of turbulent shear flow", Fluid Mechanics **2** (1956) 521.

[11] S. A. Orszag and M. D. Kruskal, "Formation of the theory of turbulence", The Physics of Fluids **11** (1968) 43.

[12] R. H. Kraichanan, "Inertial-range transfer in two- and three-dimensional turbulence", Journal of Fluid Mechanics **47** (1971) 525.

[13] V. Yakhot, S. A. Orszag, and Z.-S. She, "Space-time correlations in turbulence: kinematical versus dynamical effects", Physics of Fluids A **1** (1989) 184.

[14] V. Yakhot, Z.-S. She, and S. A. Orszag, "Deviations from the classical Kolmogorov theory of the inertial range of homogeneous turbulence", Physics of Fluids A **1** (1989) 289.

[15] Z.-S. She, S, Chen, G. Doolen, R. H. Kraichnan, and S. A. Orszag, "Reynolds number dependence of isotropic Navier-Stokes turbulence", Physical Review Letters **70** (1993) 3251.

[16] T. S. Lundgren, "Small-scale turbulence model", Physics of Fluids A **5** (1993) 1472.

[17] S. Kida and S. A. Orszag, "Energy and spectral dynamics in forced compressible turbulence", Scientific Computing **5** (1990) 85.

[18] G. A. Blaisdell, N. N. Mansour, and W. C. Reynolds, "Compressibility effects on the growth and structure of homogeneous turbulent shear flow", Journal of Fluid Mechanics **256** (1993) 443.

[19] D. K. Lilly, "Numerical simulation of two-dimensional turbulence", Physics of Fluids Supplement **II** (1969) 240; A. Wiin-Nielsen, "On the annual variation and spectral distribution of atmospheric energy", Tellus, **XIX** (1967) 4.

[20] J. R. Herring, S. A. Orszag, R. H. Kraichnan, and D. G. Fox, "Decay of two-dimensional homogeneous turbulence", Journal of Fluid Mechanics **66** (1974) 417.

[21] T. Passot and A. Pouquet, "Numerical simulation of compressible homogeneous flows in the turbulent regime", Journal of Fluid Mechanics **181** (1987) 441.

[22] G. Erlebacher, M. Y. Hussaini, H. O. Kreiss, and S. Sarkar, "The analysis and simulation of compressible turbulence", Theoretical Computing of Fluid Dynamics **2** (1990) 73.

[23] S. Sarkar, G. Erlebacher and M. Y. Hussaini, "Direct simulation of compressible turbulence in a shear flow", Theoretical Computing of Fluid Dynamics **2** (1991) 291.

[24] G. E. Karniadakis and S. A. Orszag, Nodes, "Modes and flow codes", Physics Today **March** (1993) 34.

[25] E. S. Oran and J. P. Boris, "Computing turbulent shear flows - A convenient conspiracy", Computers in Physics **7** (1993) 523.

[26] U. Frisch and S. A. Orszag, "Turbulence: challenges for theory and experiment", Physics Today, **January** (1990) 24.

[27] Y. L. Klimontovich, **Statistical physics**, Chapter 23 (Harwood, London, 1986).

[28] S. Nosé, "A unified formulation of the constant-temperature molecular dynamics methods", Journal of Chemical Physics **81** (1984) 511.

[29] W. G. Hoover, "Canonical dynamics. equilibrium phase-space distributions", Physical Review A **31** (1985) 1695.

[30] R. H. Kraichnan, "Inertial ranges in two-dimensional turbulence", The Physics of Fluids 10 (1967) 1417.

[31] R. H. Kraichnan, "On Kolmogorov's inertial-range theories", Journal of Fluid Mechanics **62** (1974) 305.

[32] A. Pouquet, M. Lesieur, J. C. André, and C. Basdevant, "Evolution of high Reynolds number two-dimensional turbulence", Journal of Fluid Mechanics **72** (1975) 305.

[33] J. P. Dahlburg, R. B. Dahlburg, J. H. Gardner, and J. M. Picone, "Inverse cascades in two-dimensional compressible turbulence. I. Incompressible forcing at low mach number", Physics of Fluids A **2** (1990) 1481.

[34] W. G. Hoover, A. J. C. Ladd, and B. Moran, "High-strain-rate plastic flow studied via nonequilibrium molecular dynamics". Physical Review Letters **48** (1982) 1818.

[35] W. G. Hoover, "Temperature, least action, and lagrangian mechanics", Physics Letters A (to appear, 1995).

[36] H. A. Posch, W. G. Hoover, and O. Kum, "Steady-state shear flow *via* nonequilibrium molecular dynamics and smooth particle applied mechanics", Physical Review E, (to appear, 1995).

[37] Z.-S. She and E. Jackson, "Constrained Euler system for Navier-Stokes turbulence", Physical Review Letters **70** (1993) 1255.

CHAPTER 9

SUMMARY AND CONCLUSIONS

Blank page

It is possible to use fast computers to study many body systems, both at and away from equilibrium. At equilibrium Gibbs' exact ensemble theory allows the Monte-Carlo method to be used [1]. Because of the multifractal nature of nonequilibrium systems, dynamic computer simulation is popular way to study nonequilibrium systems. Dynamic computer simulation can easily generate nonequilibrium steady states [2]. The development of computer technology even makes it feasible to use computers to discover efficient algorithms for numerical integration [3, 4]. The multifractal nature of nonequilibrium systems can also be studied with graphical workstation using maps corresponding to dynamic evolutions [5].

The smooth particle method, the subject of this thesis, has now been applied successfully to many complex astrophysical problems, such as colliding planets and stars, for which correct answers are unknown. It is hard to assess the adaptibility or fitness of this method for solids and fluids using complex astrophysical results with no comparison to exact solutions. In this sense, smooth particle methods are still in their infancy relative to use in typical hydrocode production problems. Its fitness for the usual solid and fluid problems has yet to be determined even though it has been applied for almost two decades now.

Smooth particle applied mechanics is hybrid: it provides *ordinary* differential equations, which is similiar to molecular dynamics, for solving the *partial* differential conservation equations. To solve the ordinary differential equations provided by smooth particle applied mechanics, we use the efficient and accurate classical fourth order Runge-Kutta method with the link-list algorithm. The link-list algorithm is the best algorithm for use of memory storage and computing time and for parallel computing. We supply constitutive equations and boundary conditions. The hardest problem in smooth particle method for usual solids and fluids is to implement the boundary conditions and surface forces. We use periodic boundaries to represent infinite systems and reflective boundaries with image particles or fixed particles for finite systems, preventing density anomalies near the boundary region, while maintaining continuous boundary fluxes. Still the surface force problem remains. An additional problem is the intrinsic viscosity which comes from the molecular dynamics (hybrid) nature of smooth particle method [6].

Here we have studied two-dimensional systems [7, 8] because the divergence of two dimensional transport coefficients [9] makes two dimensional systems especially interesting. Smooth particle applied mechanics with isentropic ideal gas equation of state, $P = \rho^2/2$, is in fact isomorphic to molecular dynamics [10]. Even in the inviscid case, smooth particle applied mechanics includes an intrinsic viscosity which can be understood through its relation to molecular dynamics. Even though the smooth particle method has intrinsic "shear viscosity" through its relation to molecular dynamics, it can be "time-reversible" for nondissipative Euler equation just as is molecular dynamics. Boltzmann's connection of macroscopic irreversibility, second law of thermodynamics, to microscopic time reversibility, Newton's equation of motion, has been a famous problem for more than one hundred years. In molecular dynamics, the explanation involves the Lyapunov instability of particle trajectories in phase space [11]. The smooth particle method provides insight into the problem for continua.

In studying the Rayleigh-Bénard instability [12] we found that a smooth particle method with image particles provides exact solutions of kinetic energies within 10 % error comparing with continuum Navier-Stokes solutions and is a very robust method. However, in applying the dense fluid equation of state, we found a fundamental shortcoming of the smooth particle method. In conventional continuum mechanics a constant pressure addition does not affect the accelerations at all, because they depend upon the *gradient* $\nabla \cdot P$. In smooth particle mechanics such an addition *does* affect the accelerations, when the particles move or vibrate, through the combination $(P/\rho^2)\cdot\nabla w$. By analogy with molecular dynamics melting affects the accelerations.

The intrinsic viscosity problem is helpful to apply this method to shock wave propagation problems. The smooth particle method is not so sensitive to the artificial viscosity coefficients compared to a one dimensional Lagrangian code. Particle distribution (regular or random distribution) does not affect the shock wave propagation. We simulated Richtmyer-Meshkov instability with smooth particle applied mechanics. The perturbed interfaces grow linearly within 3% error comparing analytical results. We did not study the nonlinear region in this thesis. For studying nonlinear region, we need to use bigger system which is possible in parallel processing. Parallel computing is not hard for smooth particle method with link-list algorithm. But to treat the real mixing problem in nonlinear region we think that a surface force implementation is essential.

Smooth particle applied mechanics contains natural velocity fluctuations with two different estimates of velocities at the particle position, $\{u\}$, the velocities at which the points move and $\{<u>\}$, the spatially-averaged velocities characterizing the neighborhood of each moving point. On the other hand we can calculate velocities at each regular grid point which is useful for Fourier transformation. The velocity difference between the spatially-averaged velocity and point velocity provides a natural high-frequency short wavelength heat sink (eddy viscosity) with phenomenological relaxation time, similiar to the thermostat idea in molecular dynamics. We applied this idea to study homogeneous turbulence generated by constant shear rate. The results do not fully explain Kolmogorov's 5/3 law which holds independent of problem dimensionality. Therefore, we conclude that the thermostat eddy viscosity is not very good for homogeneous shear flow turbulence with smooth particle applied mechanics.

Though 10 or 5 % errors are a bit large for scientific research, they are quite acceptable for most engineering applications. Therefore, we conclude that the smooth particle applied mechanics is a most useful method for problems that are difficult to solve. It is also an excellent method for teaching, research, and applications. Especially it can provide *hybrid* methods or powerful *alternative* methods to the more-usual finite difference and finite element methods. We recommend the following problems for future study. It is important to implement surface tension in the smooth particle method in order to treat real boundaries. A real surface tension is important as are the eddy viscosity or artificial viscosity in mixing problems. It would also be worthwhile to analyze the detailed effects of the intrinsic viscosity for a variety of weighting functions.

References

[1] W. G. Hoover and F. H. Ree, "Melting transition and communal entropy for hard spheres", Journal of Chemical Physics, **49** (1968) 3609; K. Binder, editor, **Monte-Carlo methods in statistical physics**, (Springer, New York, 1986); K. S. Jhung, O. Kum, and H. Lee, "Monte-Carlo calculations of free energy in the solid phase", Journal of Chemical Physics, **94** (1991) 1470.

[2] W. G. Hoover and O. Kum, "Nonequilibrium simulations", Molecular Physics Reports (to appear, 1995)

[3] S. K. Gray, D. W. Noid, and B. G. Sumpter, "Symplectic integrators for large scale molecular-dynamics simulations - a comparison of several explicit methods", Journal of Chemical Physics, **101** (1994) 4062; W. G. Hoover, O. Kum, and N. E. Owens, "Accurate symplectic integrations *via* random sampling", Journal of Chemical Physics, 103 (1995) 1530.

[4] J. C. Sprott, "Some simple chaotic flows", Physical Review E, **50** (1994) R647.

[5] W. G. Hoover and O. Kum, "Time-reversible dissipative ergodic maps", Physics Letters A (to appear, 1995).

[6] H. A. Posch, W. G. Hoover, and O. Kum, "Steady-state shear flow *via* nonequilibrium molecular dynamics and smooth particle applied mechanics", Physical Review E, **52** (to appear, 1995).

[7] W. G. Hoover and H. A. Posch, "Shear viscosity via global control of spatiotemporal Chaos in two-dimensional isentropic dense fluids", Physical Review E, **51** (1995) 273.

[8] W. G. Hoover, "Entropy for small classical crystals", Journal of Chemical Physics, **49** (1968) 1981; W. G. Hoover, W. T. Ashurst, and R. J. Olness, "Two-dimensional computer studies of crystal stability and fluid viscosity", Journal of Chemical Physics, **60** (1974) 4043; W. G. Hoover and O. Kum, "Vibrational properties of small two-dimensional classical crystals", Journal of Chemical Physics, **103** (1995) 1718.

[9] M. H. Ernst, B. Cichocki, J. R. Dorfman, J. Sharma, and H. van Beijeren, "Kinetic theory of nonlinear viscous flow in two and three dimensions", Journal of Statistical Physics, **18** (1978) 237.

[10] O. Kum and W. G. Hoover, "Time-reversible continuum mechanics", Journal of Statistical Physics, **76** (1994) 1075.

[11] W. G. Hoover, "Nonequilibrium molecular dynamics: the first 25 years", Physica **194 A** (1993) 450; W. G. Hoover, **Molecular dynamics**, edited by H. Araki, Kyoto, J. Ehlers, München, K. Hepp, Zürich, R. Kippenhahn, München, H. A. Weidenmüller, Heidelberg, and J. Zittartz, Köln, Managing editor: W. Beiglböck, lecture notes in Physics 258 (Springer-Verlag, Berlin Heidelberg 1986); W. G. Hoover, **Computational statistical mechanics,** (Elsevier, Amsterdam, 1992).

[12] O. Kum, W. G. Hoover, and H. A. Posch, "Viscous conducting flows with smooth particle applied mechanics", Physical Review E, (to appear, 1995).